

Fast Calculation of the  
Radiative Opacity of Plasma

James Austin Gaffney

Physics Department

Imperial College London

*Submitted for the award of Doctor of Philosophy*

*February 2011*

---

## Abstract

Plasma opacity calculations play an important role in solar modelling and many plasma physics and inertial confinement fusion experiments. This thesis is focussed on the fast calculation of opacity from first principles. The existing average atom (AA) opacity code IMP [1] is used alongside experimental data and detailed atomic physics to develop new models; the results show that simple models can give an excellent description of plasma spectra for a large range of conditions. The results are significant for the development of fast opacity codes which necessarily use the AA approach.

The application of fast models to very large scale calculations is considered and an efficient approach to these developed; this allows the fast description of experimental data that would not have otherwise been possible [2]. Analysis of this data then allows the accuracy of the IMP model to be further discussed. The atomic model is also considered, and an improved approach implemented. These improvements makes little difference to the description of experiment provided electron exchange is included. The range of applicability of the IMP model is then extended to higher density by adding a fast description of line broadening by electrons. This gives an excellent agreement with both experiment and more advanced opacity codes.

The treatment of atomic term structure can represent a significant portion of code runtime. A good compromise between detail and efficiency is the unresolved transition array (UTA) formulation; a consistent theory of UTAs is developed, and various models introduced. The accuracy of these is systematically tested. It is found that within the validity range of the UTA approach, a good description of the opacity can be gained using a simple model provided that the linewidth is correct. Various simplified calculations of this width are tested, and found to be inaccurate [3].

---

## Acknowledgements

My thanks go to Steve Rose for all of his help and support during my PhD, and also to Ed Hill for many useful discussions. I would also like to acknowledge Dave Hoarty and his team, James Harris and Lee Upcraft of AWE Aldermarston for their welcome into the wider community and the opportunity to experience the experimental side of laser-plasma research. I was also lucky enough to spend time at the Graduate School of Engineering, Osaka University, Japan for which I thank Peter Norreys and Ryosuke Kodama.

On a more personal note I would like to thank the whole of the Plasma Physics group at Imperial and in particular Ed, Charlie, Rhys and George for making sure I stayed sane during my time at IC. Similar thanks go to various alumni of St. Aidan's College, Durham University; you know who you are. The other residents of room 738 also need thanks for putting up with my singing, dancing and other distracting behaviour for years on end.

I could never have done it without Mum, Dad and Liz who support me in every way. Last, but by no means least, thanks to Claire for everything. We made it!

## Declaration

I hereby certify that the material of this thesis, which I now submit for the award of Doctor of Philosophy, is entirely my own work unless otherwise cited or acknowledged within the body of text.

Signed,

James Austin Gaffney

28<sup>th</sup> February 2011

# Contents

|          |  |           |
|----------|--|-----------|
| <b>1</b> | <b>Introduction &amp; Motivation</b>                                 | <b>7</b>  |
| 1.1      | Radiation in Plasma Dynamics . . . . .                               | 10        |
| 1.2      | Solar Modelling . . . . .  | 11        |
| 1.3      | Inertial Confinement Fusion . . . . .                                | 14        |
| <b>2</b> | <b>Theoretical Background</b>  | <b>17</b> |
| 2.1      | Photon Absorption Processes in Plasma . . . . .                      | 17        |
| 2.2      | Describing Photons in Plasmas . . . . .                              | 21        |
| 2.3      | Distribution Moments and Energy Transport by Photons . . . . .       | 24        |
| 2.4      | Emission and Absorption Spectra . . . . .                            | 27        |
| 2.5      | Quantum Mechanical Description of Line Opacity . . . . .             | 31        |
| 2.6      | Plasma Ionic Wavefunctions . . . . .                                 | 34        |
| 2.7      | Quantum Mechanics of Many Electron Atoms . . . . .                   | 41        |
| 2.8      | Plasma - Ion Interactions . . . . .                                  | 45        |
| <b>3</b> | <b>Opacity Calculations</b>  | <b>50</b> |
| 3.1      | History . . . . .  | 50        |
| 3.2      | The Structure of Fast Plasma Opacity Calculations . . . . .          | 52        |
| 3.3      | Self Consistent Field Models for Bound Electrons . . . . .           | 55        |
| 3.4      | Unresolved Transition Arrays . . . . .                               | 60        |
| <b>4</b> | <b>Opacity Experiments</b>   | <b>62</b> |
| 4.1      | History . . . . .  | 62        |
| 4.2      | Requirements for Plasma Opacity Measurements . . . . .               | 63        |
| 4.3      | Radiative Heating of Plasmas . . . . .                               | 64        |
| 4.4      | Typical Plasma Opacity Experiments . . . . .                         | 68        |
| <b>5</b> | <b>Improvements to the IMP Opacity Code</b>                          | <b>71</b> |
| 5.1      | Generation of Configurations . . . . .                               | 71        |
| 5.2      | The Relativistic Hartree-Fock-Slater Self Consistent Field . . . . . | 75        |
| 5.3      | Random Transition Arrays . . . . .                                   | 80        |
| 5.4      | Electron Impact Broadening . . . . .                                 | 84        |
| 5.5      | Absorption Lineshapes . . . . .                                      | 89        |
| <b>6</b> | <b>Convergence of Fast Opacity Calculations</b>                      | <b>92</b> |
| 6.1      | The Volume of Calculations in Forming the Opacity . . . . .          | 92        |

---

|          |  |            |
|----------|--|------------|
| 6.2      | Identification of Important Absorption Features . . . . .  | 93         |
| 6.3      | Achieving Convergence . . . . .                            | 96         |
| 6.4      | The Frequency-Resolved Opacity . . . . .                   | 100        |
| 6.5      | Comparison with Experiment . . . . .                       | 103        |
| 6.6      | Discussion . . . . .                                       | 106        |
| <b>7</b> | <b>The Effect of UTAs on Opacity Calculations</b>          | <b>108</b> |
| 7.1      | Background . . . . .                                       | 108        |
| 7.2      | Questions Regarding Unresolved Transition Arrays . . . . . | 124        |
| 7.3      | Testing UTA Models using Detailed Calculations . . . . .   | 126        |
| 7.4      | Results I - Transition Array Statistics . . . . .          | 133        |
| 7.5      | Results II - UTA Models and the Mean Opacity . . . . .     | 137        |
| 7.6      | Discussion . . . . .                                       | 143        |
| <b>8</b> | <b>Summary &amp; Conclusions</b>                           | <b>146</b> |
| <b>9</b> | <b>References</b>  | <b>151</b> |

## List of Figures

|     |  |     |
|-----|--|-----|
| 1.1 | The fraction of the total energy in radiation as a function of temperature of an iron plasma . . .   | 8   |
| 1.2 | Comparison of hydrodynamic simulations including and neglecting radiation . . . . .  | 10  |
| 1.3 | Observations of iron transition radiation from the sun, taken aboard the EIT/SOHO satellite  | 12  |
| 1.4 | The NIF inertial confinement fusion Hohlraum . . . . .   | 16  |
| 2.1 | Cartoons of typical opacity experiments . . . . .  | 29  |
| 2.2 | Contributions of different absorption processes to the Rosseland mean opacity . . . . .  | 30  |
| 2.3 | Notation used in the description of photon absorption . . . . .  | 31  |
| 2.4 | The average ionisation of iron in the sun . . . . .  | 42  |
| 3.1 | The general structure of opacity codes . . . . .   | 54  |
| 5.1 | Broadening of absorption lines to account for partially open valence shells . . . . .  | 75  |
| 5.2 | Charge density around an iron nucleus in the Thomas-Fermi and Hartree self consistent field models . . . . .   | 76  |
| 5.3 | Comparison of experimental and calculated $L$ shell populations for an aluminium plasma . .  | 78  |
| 5.4 | Comparison of experiment and calculation of the the mean ionisation of carbon as a function of temperature . . . . .   | 80  |
| 5.5 | Opacity of iron calculated using the Random and Unresolved Transition Array models . . . .   | 84  |
| 5.6 | Experimental transmission through an aluminium plasma of $T \sim 60$ eV, $\rho \sim 1$ g/cc compared with calculations including and neglecting electron impact broadening . . . . . | 88  |
| 5.7 | Transmission through the same Al plasma with a modified areal density showing a much improved agreement. . . . .   | 88  |
| 5.8 | The RMS error in the Voigt profile calculated using two fast algorithms . . . . .  | 91  |
| 6.1 | Schematic of the occupation-number space used in opacity calculations . . . . .  | 96  |
| 6.2 | Contribution to the partition function of different configuration sets for a Nb plasma at $T = 30$ eV and $\rho = 0.028$ g/cc . . . . .  | 98  |
| 6.3 | Contribution to the partition function of different configuration sets for a Nb plasma at $\rho = 0.028$ g/cc and various temperatures . . . . .                                     | 99  |
| 6.4 | Convergence of the frequency resolved opacity of niobium at 30 eV and 0.028 g/cc . . . . .   | 102 |
| 6.5 | Convergence of the frequency resolved opacity of niobium at 41 eV and 0.025 g/cc . . . . .   | 103 |
| 6.6 | The opacity of niobium in the UTA approximation, compared to the experiment of Hoarty <i>et al.</i> . . . . .  | 105 |
| 7.1 | Comparison of the detailed strength profile of a $2p \rightarrow 3d$ transition in iron with the distribution of strengths for varying linewidths . . . . .                          | 111 |
| 7.2 | The effect of moment - mixing on the opacity of a transition array with incorrect moments .  | 115 |
| 7.3 | Comparison of various high-order UTA strength distributions . . . . .  | 120 |

|      |  |     |
|------|--|-----|
| 7.4  | Cartoon of the model used to describe term line distributions from first principles . . . . .  | 121 |
| 7.5  | The energies and total strengths of the transition arrays used in this study . . . . .   | 127 |
| 7.6  | Comparison of the COWAN and GRASP2K codes for the $2p^3 \rightarrow 2p^23d$ transition in Fe XX .  | 128 |
| 7.7  | The variation of the variance in line amplitudes as a function of energy for the $4d^4 \rightarrow 4d^35p$ transition in Pd XII . . . . .  | 128 |
| 7.8  | The number of UTAs that are ‘unresolved’ for given porosity parameter $P$ . . . . .  | 131 |
| 7.9  | The cumulative harmonic mean strength for varying background strength . . . . .  | 133 |
| 7.10 | The skewness coefficient of all transition arrays in this study . . . . .  | 135 |
| 7.11 | The kurtosis coefficient of all transition arrays in this study . . . . .  | 135 |
| 7.12 | Line narrowing due to correlations between component line energies and strengths . . . . .   | 136 |
| 7.13 | Comparison of the kurtosis of transition arrays calculated using the model of Bauche <i>et al.</i> and from detailed calculation . . . . . | 136 |
| 7.14 | An example histogram of fractional error in harmonic mean opacity showing the effect of random and systematic errors . . . . .             | 138 |
| 7.15 | Histograms of the fractional error in the harmonic mean opacity for various UTA models and plasma conditions . . . . .                     | 139 |
| 7.16 | Comparison of the variance in transition energy calculated using IMP and the GRASP2K code  | 141 |
| 7.17 | Testing of a reduced width unweighted UTA model for strong, spikey lines . . . . .   | 143 |

## List of Tables

|     |   |     |
|-----|---|-----|
| 2.1 | Contributions of various absorption processes to the Rosseland mean opacity . . . . .                             | 30  |
| 5.1 | Energy level structure of iron at 50 eV and 1 g/cc in the Thomas-Fermi and Hartree approximations . . . . .       | 77  |
| 6.1 | Number of configurations produced by a DCA calculation with 1 valence shell . . . . .                             | 93  |
| 6.2 | Convergence of various parameters of IMP opacity calculations as the size of calculations are increased . . . . . | 101 |

# 1 Introduction & Motivation

The interaction of radiation with matter is a difficult problem that has applications in many areas of physics. That is particularly true of plasma physics, since the systems we aim to study cannot be probed directly. Analysis of the emission spectra from hot matter can give a wealth of useful information even when the sample is not directly accessible, making spectroscopic measurements very important in plasma physics. The modelling of this emission is a complex problem that depends on the thermodynamics of the plasma and its composition, which means that calculations must be performed in detail for all of the conditions that are expected. We aim to produce a model for the radiation field that is consistent with all of the ways that photons can interact with matter - this requires a description of the photon absorption and emission at all points in the plasma.

This model then allows the calculation of absorption and emission spectra from hot matter, and the effect of radiation on energy balance. In hot systems this can be very important; consider figure 1.1 where we plot the proportion of the total energy in the radiation field as a function of temperature for an iron plasma at 10% of solid density. At temperatures that are of relevance to solar physics and fusion science, this fraction can be quite large. In fact, the relative ease with which photons propagate means that this simple analysis does not fully measure the importance of photons in the energy balance of a plasma system. Clearly an accurate model of the photon field, and the way it interacts with the constituent particles of the plasma, is essential.

General calculations must include all important absorption channels. These are described in detail in the following sections however the calculations are complicated by several aspects of the plasma system. The high temperature means that several different ion stages (defined by the number of electrons still bound to their nuclei) must be included for each atomic species, and each ion stage can represent a large number of electron configurations. Each of these configurations can absorb photons of many different energies, each requiring a quantum mechanical calculation making the computational workload very large. The relative populations of these ion stages and states must be calculated self consistently with the various excitation and relaxation processes that can occur. Finally, the plasma environment in which these absorbing ions reside



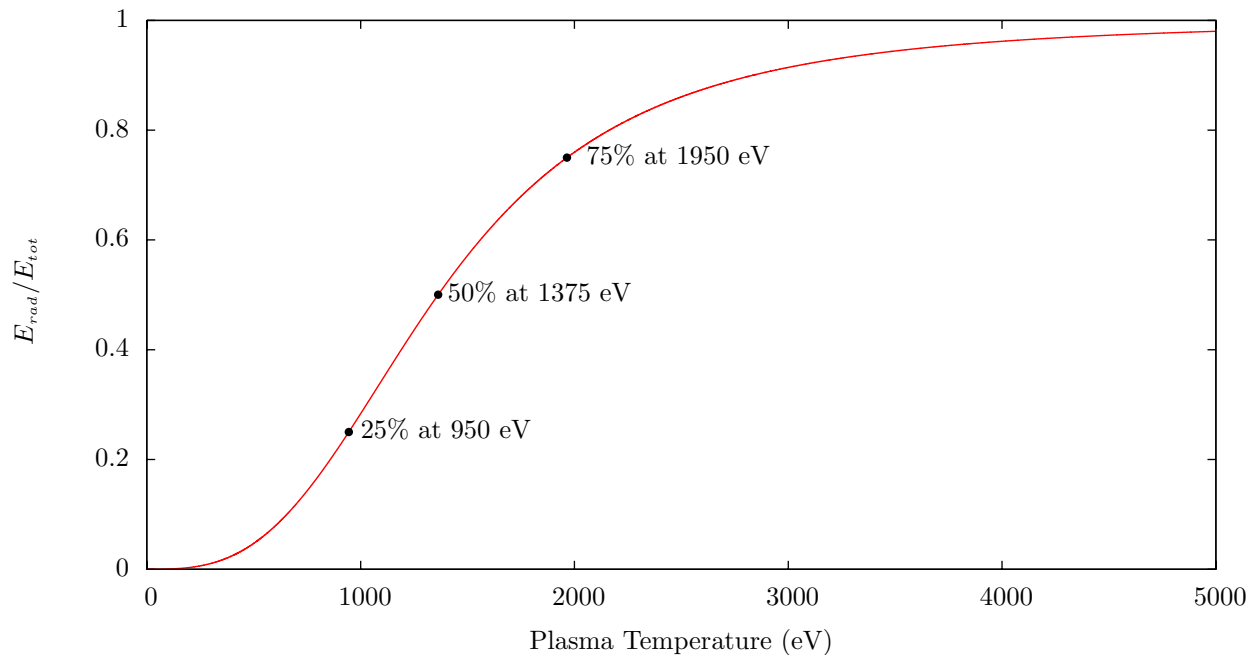


**Figure 1.1:** *The energy in a Planckian radiation field compared to the total plasma energy (thermal + radiation) as a function of temperature. Results are shown for an iron plasma at 10% of solid density, and we have assumed that the plasma ions are ionised to the L shell ( $16^+$ )*

must be taken into account since interactions between bound electrons and the surrounding plasma change energy levels, shifting and removing absorption resonances according to the plasma density and temperature. These interactions are, in general, time dependant since the surrounding plasma particles move, and this must also be modelled in order to gain a good description.

The complications described above can make calculations very difficult, and therefore slow to implement and perform. There is interest, however, in trying to keep calculation times reasonably low since the description of radiation is only a small part of the description of the entire plasma system. The ions and electrons interact with each other as well as with the radiation so the distributions of all plasma constituents should be calculated self-consistently. This is compounded by the fact that in many systems photons are able to travel relatively large distances, transporting heat to different parts of the plasma. If all of these coupled distributions are to be solved together, taking into account spatial and time dependence, then it is not possible to spend huge amounts of time calculating radiative properties.

In general the very large scale calculations described above are not undertaken without approximations.

In this thesis I will describe many of these; the main underlying assumption of this work is that of ‘local thermodynamic equilibrium’ (LTE). It is assumed that interactions between electrons keep them thermalised at some temperature  $T$ , and that they drive ion populations into equilibrium at the same temperature. The electron and ion state populations are then given by the Maxwell-Boltzmann and Saha-Boltzmann statistics respectively, and detailed calculations are not required. The assumption that the radiation field, either self generated or applied, is not strong enough to drive either distribution away from equilibrium is implicit in the assumption of LTE. When the system is in LTE, the emission and absorption of a plasma are simply related (Kirchoff’s Law); in this thesis we will describe both of these through the opacity  $\kappa(\epsilon)$ , which describes the probability that a photon of energy  $\epsilon$  will interact with the plasma, per density per distance travelled. The opacity has units ( $\text{cm}^2/\text{g}$ ) and in LTE it is a function of temperature  $T$ , density  $\rho$  and composition alone. This allows it to be calculated *a priori* and used as an input for the simulation of the plasma dynamics. It should be noted, however, that the range of temperatures and densities in a typical calculation can be very large, and interpolation errors potentially significant [4]; there is still interest, therefore, in developing the capability to calculate the opacity fast enough to give accurate results on-demand. This is of particular importance in the design of experiments, where synthetic spectra may be required, since in that case the frequency-resolved emission must be integrated over space and/or time.

In this thesis I will consider the calculation of the opacity using relatively fast models that are suitable to use in plasma dynamic simulations, and for the modelling of spectra. The work is based on the IMP code [1], which is upgraded and compared to experiment in order to elucidate the importance of various approximations that can be used to speed up calculations. In particular the extension of fast opacity models into difficult regimes of plasma conditions is investigated. A large portion of the final part of this work focusses on the treatment of atomic term structure, which is of great relevance to mid to high  $Z$  plasma that play an important role in various plasma systems.

The remainder of this introduction will give some examples of the application of LTE opacity calculations to real plasma systems. The assumption of LTE relies on a high plasma density, and in practice this is only satisfied in certain regions of a given plasma. One system where it is certainly valid is the interior of a star; another important system is the ‘Hohlraum’ used to produce X-ray drive in various plasma experiments.

Prior to these discussions, however, we will elaborate on the effect of radiation on plasma dynamics.

## 1.1 Radiation in Plasma Dynamics

The absorption and emission of radiation by matter effectively couples the behaviour of a plasma system to the radiation field and visa-versa. The efficiency with which the plasma absorbs and emits radiation, the size of the system, and the details of any applied fields all determine how important this effect is; in many cases the radiation field can be neglected or treated using simple approximations. In others, however, this is not the case and calculations must include radiation.

By way of an example, consider figure 1.2, where we reproduce a figure by Nagatomo *et al.* [5] (With thanks to Prof. Hideo Nagatomo). The results from simulations of an imploding fast ignition target are shown, with radiation included and neglected (left and right panels respectively). The upper and lower plots show electron density and temperature as a function of space, and contours show the boundary between the plastic ablator and gold cone plasmas. The difference is clear - radiation is transporting energy from the hot plasma generated by the drive lasers inwards and heating the tip of the gold cone. This is then expanding

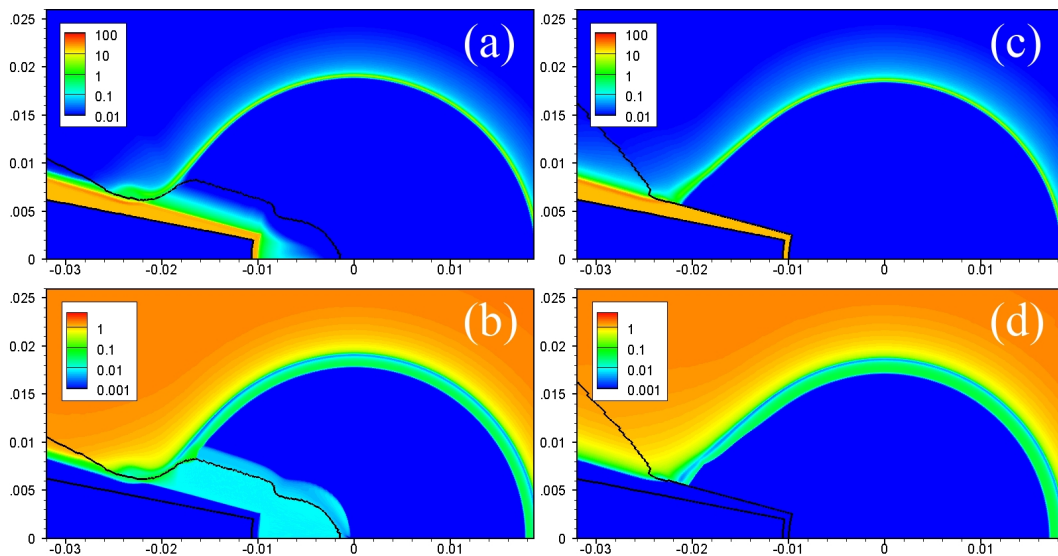


**Figure 1.2:** *Hydrodynamic simulations of an imploding fast ignition capsule, calculated with and without the effects of radiation transport. The figure is reproduced with permission from the work of Nagatomo et al.[5]. Left and right columns show data with and without radiation; top and bottom panels show mass density and electron temperature. The black contour shows the boundary between gold and plastic. It can be seen that the inclusion of energy transport by radiation significantly modifies the plasma conditions at the tip of the fast ignition cone.*

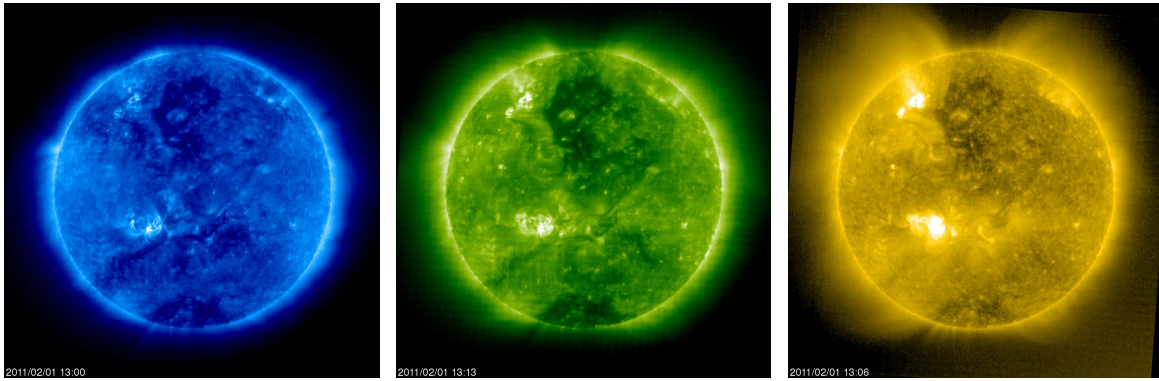
and mixing with the fuel. This will have dramatic consequences for the symmetry of the implosion and absorption of the ignition laser required in this scheme (see section 1.3). The calculations of Nagatomo *et al.* include a fairly complex treatment of radiation; the inclusion of the radiative model increases the calculation time by a factor of 10 [6].

The reason that radiation can play such an important role is that photons are able to transport energy and momentum between different parts of the plasma system. Photons travel faster, and often further, than other particles and so they can play a very important role even when they represent a fairly small proportion of the total energy [7]. In fluid models of plasma dynamics, the motion of the system is determined by equations that express the conservation of mass, momentum and energy of small elements of the plasma; these equations must include source and sink terms due to radiation transport, the evaluation of which require knowledge of the details of the radiation field.

## 1.2 Solar Modelling

The modelling of solar structure has been a very important field in science for over 100 years, and remains important in modern physics. Stars have presented many challenges to researchers, and the solution to these problems has lead to some of the biggest discoveries in the last century. The Sun plays a pivotal role in this research since it is the only star that we can make detailed observations of; measurements of other stars are very limited due to their distance. Even though the options are much more varied for our closest star, we of course cannot make direct measurements and so rely on spectroscopic observations; the opacity is essential in understanding what is observed. An example of these observations is shown in figure 1.3 where monochromatic X-ray images of the sun, sensitive to radiation from different ion stages of iron, are shown. The data were taken using the EIT/SOHO satellite and allow the measurement of temperature variations in the solar atmosphere.

The absorption of the stellar material means that the light we observe only originates from the low density corona of the star; the internal structure of the star, however, is dependant on the opacity at all points. In order to model a star's structure more information is needed and since the range of plasma conditions in a star cannot be addressed by experiment, opacity calculations are essential to the problem.

(a)  $FeIX$  ( $171\text{\AA}$ )(b)  $FeXII$  ( $195\text{\AA}$ )(c)  $FeXV$  ( $284\text{\AA}$ )

**Figure 1.3:** Monochromatic images of the sun, taken at three different wavelengths corresponding to different iron ionisation stages. The images were taken by the EIT/SOHO solar observatory at the 1<sup>st</sup> Lagrangian point. Comparison of the different images allows temperature variations in the solar atmosphere to be measured. Images taken from <http://umbra.nascom.nasa.gov/eit/>

The basic structure of the Sun is determined largely by hydrostatic equilibrium between the plasma and gravitational pressures. This, combined with expressions for mass conservation, energy generation and energy flux, results in a set of equations that require three physical inputs. The first is the equation of state of the plasma, the second the rate of energy generation and the third the opacity. These must be known as a function of temperature, density and plasma composition in order to model the star. The total opacity determines the radial temperature gradient through the equation

$$\frac{dT}{dr} = -\frac{3\kappa L\rho}{16\pi acr^2T^3} ,$$

where  $L$  is the energy flux,  $c$  is the speed of light,  $a$  is the radiation density constant and  $r$  is the radial position in the star. This expression is simply a re-arrangement of the energy flux in the diffusion approximation where the opacity is related to the conductivity  $\sigma$  through

$$\sigma = \frac{4acT^3}{3\rho\kappa} . \quad (1.2.1)$$

The opacity in these expressions includes the opacity to electrons and to photons; under the conditions expected in the solar interior (  $1300 \rightarrow 150$  eV) the electron population will hold the majority of the energy

and so it may appear that heat transport by electrons is the most important. This, in fact, is not the case since their longer mean free path means that photons are able to carry energy over large distances; in the Sun the energy flux due to photons dominates [8]. The calculation of the radiative opacity of solar material is therefore very important for calculations.

Although the mean free path is large enough for heat transport by photons to be significant, it is still very small. Photons take on average  $10^7$  years to reach the surface from the core of the sun, and the maximum temperature change over a mean free path in the solar interior is  $\sim 10^{-10}$  eV; their motion is therefore diffusive to a very good approximation and thermodynamic equilibrium is well maintained at the local temperature. These facts are very useful when approaching the problem of calculating the opacity of stellar material.

The details of the internal structure of the Sun are clearly sensitive to the opacity. One of the best tests (and biggest problems) in current models is describing the onset of convection in the solar core. The core of the Sun is stable to convection and as mentioned the majority of the energy is carried by radiation. This is therefore known as the ‘radiative zone’. At some radius, however, convection currents occur that mix the outer ‘convective zone’ of the star and vastly improve heat transport. The atmosphere is unstable to convection if an element of plasma, when displaced upwards, becomes buoyant; a simple model then predicts the condition for convection as

$$\left| \frac{dT}{dr} \right| > \frac{\gamma - 1}{\gamma} \frac{T}{P} \left| \frac{dP}{dr} \right| ,$$

where  $\gamma$  is the ratio of specific heats of the plasma. Since the temperature gradient is sensitive to changes in opacity, the calculated radius at which convection occurs is a good test of the input opacity models. This depth can be measured with great accuracy [9], and is found to occur at the radius where large numbers of iron transition lines are expected to appear. The increased opacity due to these lines means that a large temperature gradient is required to maintain the outwards energy flux. Theoretical predictions of this radius agree poorly with the measured result, and the discrepancy has been blamed on the opacity in this region. In this thesis we focus on the description of mid - high  $Z$  elements, which are inherently difficult to describe and have a dramatic effect on the opacity in this region of the Sun’s atmosphere.

Pulsating variables are another class of stars where radiation plays a very important role. These stars are extremely useful in astronomy and astrophysics due to their reliability as standard candles, and their behaviour is determined critically by the variation in opacity with temperature in their atmosphere [10]. Essentially an expansion of the star causes a cooling of its atmosphere; the opacity of some element (usually helium) at some radius drops as it becomes less ionised, resulting in less energy deposition in that layer and a reduced pressure. The atmosphere then falls under gravity until the ionisation and opacity rise again, increasing the pressure and causing the star to expand. The variation in opacity with ionisation is of critical importance in describing these stars, in fact problems with stellar pulsation models have led to large interest in opacity calculations in the past.

### 1.3 Inertial Confinement Fusion

The effort to produce energy through the fusion of two hydrogen nuclei has been a major driving force in plasma physics for many decades. In order to generate useable energy the power generated through fusion reactions must exceed the rate at which energy is lost from the plasma; this leads to the important ‘Lawson Criteria’ which, for deuterium - tritium (DT) reactions, is

$$n_e \tau_E \gtrsim 10^{14} \text{ s/cm}^3, \quad (1.3.1)$$

where  $n_e$  and  $\tau_E$  are the electron density and energy confinement time, respectively [11]. Attempts to satisfy this requirement have led to two main approaches to fusion energy; magnetic confinement fusion (MCF) in which a large scale, low density fusing plasma is maintained for a long period of time, and inertial confinement fusion (ICF) in which a very high density plasma is created for a short period of time. The low density of MCF plasmas makes the effects of radiation largely unimportant to heat transport (and the LTE assumption poor) and so the work in this thesis has little application; in ICF, however, radiation plays a very important role.

In ICF the fundamental problem is how to generate the large densities required to satisfy equation (1.3.1) before the fuel blows apart. To do this it is necessary to use a spherical implosion. A typical ICF target

then consists of a shell of low  $Z$  material around the DT fuel. The outer surface of this fuel is then heated rapidly, expanding outwards and driving the remaining shell inwards like a rocket. The fuel is then pushed in front of the imploding shell and stagnates at high temperature and density at the centre. The implosion can be driven in various ways which give rise to the various different approaches to ICF; the common theme is the effort to provide a uniform drive in order to mitigate instabilities during the implosion.

The development of high energy lasers presents the possibility of using light to deposit energy into the shell and drive the implosion, and the majority of current work focusses on this approach. In ‘direct drive’ ICF, laser beams directly illuminate the outer surface of the fuel pellet. It is essential to provide as uniform an illumination as possible so that the implosion is symmetric; even so this approach normally requires a method of producing a small ignition hotspot in the compressed fuel to reduce the required implosion parameters. From this point, fusion  $\alpha$ -particles drive a burn wave that consumes all of the fuel in the target. Popular methods of providing this hotspot are the fast ignition concept (as mentioned in section 1.1) where a short laser pulse is driven into the stagnating plasma, and shock ignition in which the incident laser energy is varied in time in order to launch a shock front into the fuel. The timing of this shock is very important so that it provides the ‘spark’ at the optimum time.

Radiation is important in energy transport in these models; in particular the generation of soft X-rays is critical since they can pre-heat fuel and reduce the implosion efficiency. Even when these are not able to heat the fuel they can launch shocks modifying the density. In the case of shock ignition this may change the required timing of the ignition shock and so an accurate description of this effect is very important. The process by which these shocks are produced has been shown to be sensitive to the variation in the opacity of the ablator material with radius [12]; in the case where absorption lines produce a trough in the opacity at some radius, this serves as a bottleneck to radiative energy and a shock will be launched.

A second highly developed approach to ICF uses ‘indirect drive’, where a high  $Z$  can, or ‘Hohlraum’ is used to convert laser energy to X-rays which drive the implosion. By enclosing the fuel in this can, a highly uniform and symmetric X-ray field is produced driving a highly symmetric implosion. The largest experiments of this type are currently undertaken on the NIF facility at Lawrence Livermore National Laboratory [13]; in figure 1.4 we show the Hohlraum setup for these experiments.



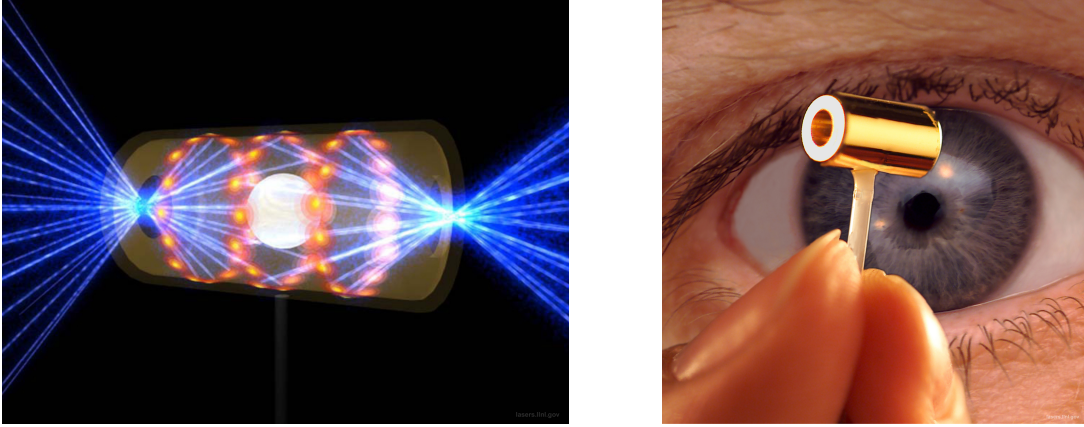


**Figure 1.4:** *The indirect drive scheme for inertial confinement fusion. A high  $Z$  can (‘Hohlraum’) is used to convert laser energy into a bath of near-Planckian radiation that provides a symmetric implosion of the fuel pellet mounted inside. The images show the millimetre-scale gold ignition Hohlraums used on the NIF facility; the drive energy is provided by 192 laser beams focussed onto the inside surface. Image credit: Lawrence Livermore National Laboratory*

Radiation is even more important in indirect drive ICF since the details of the implosion, which are determined by the drive radiation, become linked with the conversion of laser light to X-rays in the walls of the Hohlraum. The laser light heats the high  $Z$  plasma which then re-radiates in the soft X-ray region. These X-rays undergo many absorption and re-emissions within the walls and rapidly thermalise into a near-Planckian spectrum. This is the process by which the high drive symmetry can be achieved, however the efficiency of the conversion of laser light is dependant on the absorption of the Hohlraum walls. Due to the high optical depth of the walls this absorption takes the form of a diffusive ‘Marshak wave’ propagating into the wall [14]. The energy lost to the walls of the Hohlraum is then determined by the rate at which this wave propagates. A simple model for the gold Hohlraum of NIF predicts that the energy absorbed by the wall will be [15]

$$E_w \propto T^{3.25} \sqrt{\frac{t}{\kappa_0}},$$

where  $t$  is time,  $T$  is the temperature of the heating radiation and  $\kappa_0$  is the mean opacity. The efficiency with which laser light is converted to X-rays is determined by the opacity of the Hohlraum wall; in general the variation of the opacity with temperature and density must be calculated accurately to give a good description of the drive radiation. Changes in the opacity between different models then result in different laser power requirements and this can have an important bearing on the design of targets and facilities [16].

## 2 Theoretical Background

Opacity calculations represent a difficult computational and theoretical problem, as they require an in-depth description of the atomic properties of plasma constituents, along with thermodynamic quantities and the equation of state. These properties are inherently linked through interactions between the various particles in the plasma; In this section we give the general theoretical basis required to approach the problem. In following sections these concepts are used, and in some cases simplified, to allow the calculation of plasma opacity.

### 2.1 Photon Absorption Processes in Plasma

The description of the energy contained and transported by light in any system requires knowledge of the number of photons at a given position in space and time, and the details of their propagation. This problem is complicated by the ease with which photons couple to the states of the other particles in the plasma. This must be taken into account in any description of radiation transport. In this section we will discuss the various processes that cause this coupling, and introduce the theory by which they are described.

Photon absorption and emission mechanisms involve the transfer of energy between photons and electrons, a coupling that can occur in several different ways. We will distinguish between processes that cause a change in the properties of the photon and those that cause the destruction or creation of a photon with corresponding transfer of energy. These are termed scattering and photoabsorption/emission respectively, and have different parts to play in the dynamics of a plasma. Scattering processes act to isotropise the radiation field however since they do not cause a transfer of energy between the radiation field and the plasma they do not drive the system into thermodynamic equilibrium [17]. The opposite is true of photoabsorption and emission, where there is a direct transfer of energy between the plasma and radiation field, allowing the possibility of thermodynamic equilibrium.

We describe the photon field in a plasma through the distribution function  $f_{phot}(\mathbf{r}, \mathbf{\Omega}, \epsilon, t)$ , which is the number of photons per volume, solid angle and energy at time  $t$ , and consider variation in this due to various processes. Since we approach opacity calculations from a microscopic point of view this distribution function

picture will be used to develop theory before certain important macroscopic quantities are derived.

### 2.1.1 Photoabsorption and Emission

The important process of the absorption or emission of a photon result in the transfer of energy between an electron and a photon that moves in the field of an ion. The result of the energy transfer is a change in state of the electron and the creation or annihilation of a photon. This is a quantum mechanical process, however to begin with we describe the various absorption and emission processes in terms of transition rates which will be derived quantum mechanically in later sections. We use the definitions of Condon & Shortley [18], where the increase or decrease in the total number of photons in the system is described through Einstein rate coefficients. These have been generalised to suit our more detailed description of the photon distribution  $f_{phot}$ . For a lower state  $i$  and an upper state  $f$  there are several processes to consider;

- Absorption ;

Described by the Einstein  $B$  coefficient  $B_{if}$ . The rate of removal of photons from the distribution function  $f_{phot}$  is defined as

$$\left( \frac{d}{dt} f_{phot} \right)_{Abs} = -\epsilon c N_i B_{if} \phi_{Abs}(\epsilon) f_{phot}(\epsilon) , \quad (2.1.1)$$

where  $N_i$  is the number density of atoms in the initial state,  $\epsilon$  is the energy of the transition and the energy profile associated with the transition is  $\phi_{Abs}$ . This is normalised such that

$$\int_{-\infty}^{\infty} \phi_{Abs}(\epsilon) d\epsilon = 1 .$$

- Stimulated Emission ;

Here an electron residing in an excited state  $f$  is perturbed by an incoming photon and relaxes, creating a second photon. In analogy with absorption the rate of stimulated emission is

$$\left( \frac{d}{dt} f_{phot} \right)_{Stim} = \epsilon c N_f B_{fi} \phi_{Stim}(\epsilon) f_{phot}(\epsilon) , \quad (2.1.2)$$

where a new lineshape  $\phi_{stim}$  has been introduced to account for differences in emission and absorption.

It should be noted that the indices on the  $B$  coefficient for emission have been reversed signifying a new coefficient.

- Spontaneous Emission ;

The excited state of an ion has finite lifetime and so emission can occur spontaneously without the presence of a second photon. The rate of emission in the case does not depend on the number of photons already present, only on the number of initial ions available. We define the Einstein  $A$  coefficient, with units  $s^{-1}$ , such that

$$\left( \frac{d}{dt} f_{phot} \right)_{Spont} = \frac{1}{4\pi} N_f A_{fi} \phi_{Spont}(\epsilon) . \quad (2.1.3)$$

In equilibrium, the above processes are in detailed balance (the total emission and absorption rates balance) and this allows the Einstein relations to be derived. In our case these are

$$A_{fi} = 8\pi \frac{\epsilon^3}{h^3 c^2} \frac{\phi_{stim}(\epsilon)}{\phi_{Spont}(\epsilon)} B_{fi} , \quad (2.1.4)$$

$$g_i B_{if} \phi_{Abs}(\epsilon) = g_f B_{fi} \phi_{stim}(\epsilon) , \quad (2.1.5)$$

where  $g_i$  and  $g_f$  are the degeneracies of the two ion states. The above relations are very useful in simplifying the form of the radiative transfer equation. In particular, the relationship between the absorption and stimulated emission allows these processes to be described through a single coefficient, which is normally considered as the absorption rate corrected for stimulated emission. This result is used in later sections and is very useful in reducing the number of quantum mechanical calculations that must be performed.

The initial and final states of the electron  $i, f$  can be classified as being bound or free depending on the relative values of its potential and kinetic energies; this classification allows us to describe several different absorption and emission processes depending on the type of state the electron occupies before and after the interaction. In this way we define free-free, bound-free and bound-bound processes for photoabsorption (in which the final state is higher in energy than the initial state). As a result of the different energy

level structures for bound and free electrons, these different transition types result in different characteristic structures in absorption and emission profiles; for this reason it is convenient to consider them separately in opacity calculations. The general theory is the same, however, and so for the majority of this section they will be treated on the same footing.

### 2.1.2 Scattering

The change in direction of a photon, with or without an accompanying energy shift, due to interactions with the plasma is termed scattering. The majority of the energy remains with the photon in this process and so the main effect is to isotropise radiation.

The scattering of a beam of photons is described through the scattering cross section  $\sigma_s(\epsilon)$ , which measures the area of the incident beam that is scattered by a given centre. The cross section therefore gives the intensity that is lost from the incident beam, and so will be very useful in the description of radiation transport in following sections. When scattering is to be used in the diagnosis of material properties, however, more information can be derived from the differential cross section defined by

$$\sigma_s = \int \frac{d\sigma_s}{d\Omega} d\Omega ,$$

where the integrand is the cross section for scattering into the range of solid angles between  $\Omega$  and  $\Omega + d\Omega$ .

For plasmas of relevance to experimental applications the main interaction is between free electrons and the electric field of the photon; the photon's energy is passed to the electron, and the subsequent acceleration causes re-emission of that energy in a different direction. A non-relativistic treatment of the electron's motion results in the Thomson scattering cross section, which for unpolarised light gives

$$\left( \frac{d\sigma_s}{d\Omega} \right)^{(T)} = \frac{r_0^2}{2} (1 + \cos^2 \theta) , \quad (2.1.6)$$

and

$$\sigma_s^{(T)} = \frac{8\pi}{3} r_0^2 = 6.65 \times 10^{-25} \text{ cm}^2 . \quad (2.1.7)$$

In the above equation,  $r_0 = e^2/4\pi\epsilon_0 mc^2$  is the classical radius of electron and  $\theta$  is the angle between the incident and scattered light. The non-relativistic treatment of electron motion is valid when the photon energy is much less than the rest mass of the electron,  $\epsilon \ll 511$  KeV. The effects of relativistic electron motion are to break the symmetry between forward and backscattering seen in equation (2.1.6), and to introduce a small shift in the energy of the photon which depends on the incident energy and the scattering angle. This high energy behaviour is known as Compton scattering and is described by the Klein-Nishina formula,

$$\left(\frac{d\sigma_s}{d\Omega}\right)^{(C)} = r_0^2 \frac{1 + \cos^2 \theta}{2} \frac{1}{1 + \gamma(1 - \cos \theta)^2} \left[ 1 + \frac{\gamma^2(1 - \cos \theta)^2}{(1 + \cos^2 \theta)(1 + \gamma(1 - \cos \theta))} \right], \quad (2.1.8)$$

where  $\gamma = \epsilon/mc^2$ , and which reproduces the Thomson result for small  $\gamma$ .

In this thesis we are most interested in the description of absorption processes on opacity calculations, since they monopolise a large portion of code runtime. The scattering cross section will be based on the work of Sampson [19], who showed that the Klein-Nishina formula predicts a scattering contribution to the opacity that is characterised by the effective cross section

$$\sigma_s(\epsilon, k_B T) = \sigma_s^{(T)} G\left(\frac{\epsilon}{k_B T}, T\right), \quad (2.1.9)$$

where the function  $G$  includes corrections for the motion of electrons, the density of photons in the scattered state, and both scattering in and out of the beam. In calculations using the IMP code, the low temperature form of the function  $G$  is used (see equation (37) in the reference). Equation (2.1.9) is derived for calculations in thermodynamic equilibrium.

## 2.2 Describing Photons in Plasmas

In order to find the effects of the above processes on plasma dynamics, we consider the time evolution of the photon distribution. This is the sum of all the photon sources and sinks described previously. The remainder of this section is concerned with the analysis of this system.

We describe the plasma using an Eulerian coordinate system, where the plasma moves over a fixed grid of points. In this case the time derivative of the photon distribution at some point is not simply given by

the sources and sinks at that point; it must take into account the net flux of photons from the surrounding plasma. Then the total time derivative has a spatial dependence part;

$$\frac{d}{dt} = \frac{\partial}{\partial t} + c(\mathbf{\Omega} \cdot \mathbf{\nabla}) ,$$

where the right hand side is the convective derivative. Using the above expression and the absorption and emission rates described previously we obtain the radiative heat transfer equation:

$$\begin{aligned} \frac{\partial}{\partial t} f_{phot} + c(\mathbf{\Omega} \cdot \mathbf{\nabla}) f_{phot} &= \frac{1}{4\pi} \sum_n N_f^n A_{fi}^n \phi_n(\epsilon) \\ &+ c \sum_n N_f^n B_{fi}^n \epsilon f_{phot} \phi_n(\epsilon) \\ &- c \sum_n N_i^n B_{if} \epsilon f_{phot} \phi_n(\epsilon) \\ &- cn\sigma_s(\epsilon) f_{phot} \quad . \end{aligned} \quad (2.2.1)$$

In this equation the summations over  $n$  refer to all possible electron transitions that can occur, and the emission and absorption lineshapes are assumed to be the same.

Analysis of equation (2.2.1) is simplified by using general formulae (2.1.4)-(2.1.5) which relate the various Einstein coefficients and allow the ion terms to be collected together. The result is

$$\begin{aligned} \frac{\partial}{\partial t} f_{phot} + c(\mathbf{\Omega} \cdot \mathbf{\nabla}) f_{phot} &= c\epsilon \sum_n B_{if}^n \left\{ \frac{2\epsilon^2}{h^3 c^3} \frac{g_i^n}{g_f^n} N_f^n - \left( 1 - \frac{N_f^n g_i^n}{N_i^n g_f^n} \right) N_i^n f_{phot} \right\} \phi_n(\nu) \\ &- cn\sigma_s(\nu) f_{phot} \quad . \end{aligned} \quad (2.2.2)$$

In this equation the summation describes all processes that involve the creation or annihilation of a photon and the other term describes scattering. The second term in the summation shows that the effect of stimulated emission is to reduce the absorption rate by an amount related to the populations of upper and lower states. Finally, both emission and absorption of photons are described by a single Einstein coefficient  $B_{if}$ , hence a single description of the quantum mechanical electron-photon system can be used to describe all photon absorption processes.

The radiative heat transfer equation, in the form shown above, can be used to describe the photon field in a given plasma provided that the various absorption rates, and the populations of all emitters and absorbers ( $N_i^n$  and  $N_f^n$ ) are known. Both of these problems introduce significant difficulties; the first is that the number of absorption and emission paths in a given plasma is very large, the second is that the calculation of ion populations requires the solution of a set of equations similar to equation (2.2.2). This leads to a very large system of coupled differential equations, the analysis of which is a complex problem in itself. Significant simplification is reached by assuming that collisions between electrons and ions are fast enough to drive both populations to equilibrium at some local temperature  $T$ . These collisions must be fast enough to overcome radiative transitions (since we do not assume an equilibrium photon distribution). This is the case when the plasma density is high giving large collisional rates, and the temperature is low giving weak emission; then the ion populations that we require are described by Boltzmann statistics,

$$\frac{N_2}{N_1} = \frac{g_2}{g_1} e^{-\epsilon_{12}/k_B T} , \quad (2.2.3)$$

where the temperature can vary with position and time. This situation is known as local thermodynamic equilibrium (LTE). In the case where the photon field is also in equilibrium at temperature  $T$ , it is described by the Planck function,

$$f_{planck}(\epsilon, T) \, \mathbf{dr} \, \mathbf{d}\Omega \, d\epsilon = \frac{2\epsilon^2}{h^3 c^3} \frac{1}{e^{\epsilon/k_B T} - 1} \mathbf{dr} \, \mathbf{d}\Omega \, d\epsilon . \quad (2.2.4)$$

This expression can be substituted in the heat transfer equation to give the LTE radiative heat transfer equation

$$\begin{aligned} \frac{\partial}{\partial t} f_{phot} + c(\boldsymbol{\Omega} \cdot \boldsymbol{\nabla}) f_{phot} &= c \epsilon \left(1 - e^{-\epsilon/k_B T}\right) \sum_n B_{12}^n N_1^n (f_{planck}(\epsilon) - f_{phot}(\epsilon)) \phi_n(\epsilon) \\ &\quad - cn\sigma_s(\epsilon) f_{phot} . \end{aligned} \quad (2.2.5)$$

It should be noted that although we have used the Planck function we do not assume that the radiation field is Planckian at this stage; the assumption of LTE has, however, related the emission and absorption



terms through  $f_{Planck}$ . This is the well known ‘Kirchoff’s law’. The above expression can now be used to describe the evolution of the photon distribution function for a plasma in equilibrium. The population of the lower ion configuration is calculated from the energy of the configuration, which we discuss in the following sections.

Equations (2.2.5)-(2.2.4) can be used to determine the radiation field at all points in a plasma once the energies of ion states and transitions are known. They also define the plasma opacity through the well known Beer-Lambert law for a material of mass density  $\rho$ ;

$$\frac{d}{dx}I(\nu) \equiv -\rho\kappa(\nu)I(\nu) , \quad (2.2.6)$$

The form of which is identical to equation (2.2.5) in the case of a steady state, homogeneous 1D plasma with a strong applied photon field (in which case the self-emission term can be neglected as  $f_{phot} \gg f_{planck}$ ). This allows us to identify the opacity with the quantum mechanical Einstein coefficients and cross sections as shown below.

$$\kappa(\epsilon) = \frac{1}{\rho} \left\{ \epsilon \left( 1 - e^{-\epsilon/k_B T} \right) \sum_n N_1^n B_{12}^n \phi_n(\epsilon) + n\sigma_s(\epsilon) \right\} , \quad (2.2.7)$$

$$= \frac{1}{\rho} \left\{ \left( 1 - e^{-\epsilon/k_B T} \right) \sum_n N_1^n \sigma_a^n(\epsilon) + n\sigma_s(\epsilon) \right\} , \quad (2.2.8)$$

The above expression is also written in terms of the absorption cross section,  $\sigma_a^n(\epsilon) = \epsilon B_{12}^n \phi_n(\epsilon)$  in analogy with the description of scattering. Throughout this thesis we will use this above definition of the opacity, and we concern ourselves with the treatment of each electron - electron transition in the summation separately.

## 2.3 Distribution Moments and Energy Transport by Photons

The photon distribution function describes all properties of photons in a plasma. This microscopic description is not, however, the most efficient way of calculating physically interesting quantities; in fact the radiative transfer equations given in section 2.2 can be reformulated to explicitly give useful macroscopic quantities. This is done by taking moments of the transfer equation.

In this analysis  $f_{phot}$  takes the role of a probability density function and the propagation of photons in the  $x$  direction can be characterised by the moments

$$f_{phot}^{(n)} = \int \mu^n f_{phot}(\mu) d\Omega, \quad (2.3.1)$$

where  $\mu = \cos \theta$  is the component of the photon's motion along  $x$ , and the various values of  $n$  can be used to generate useful physical quantities. The first few of these are

$$\bullet \text{ Photon Concentration; } n_{phot} = \int f_{phot}(\mu) d\Omega \equiv f_{phot}^{(0)}, \quad (2.3.2)$$

$$\bullet \text{ Photon Flux; } j_x = \int v_x f_{phot}(\mu) d\Omega = \int c \mu f_{phot}(\mu) d\Omega \equiv c f_{phot}^{(1)}, \quad (2.3.3)$$

$$\bullet \text{ Photon Pressure; } P_x = \int p_x v_x f_{phot}(\mu) d\Omega = \int \frac{\epsilon}{c} \mu c \mu f_{phot}(\mu) d\Omega \equiv \epsilon f_{phot}^{(2)}. \quad (2.3.4)$$

all of which are important in describing the behaviour and stability of a given plasma system.

Using the definitions (2.3.2)-(2.3.4) and the radiative transfer equation, a series of relations that link each moment of the distribution  $f_{phot}$  are found to the next highest order. In general such a system cannot be solved, but under certain assumptions formulae for the moments can be obtained.

We begin by multiplying the radiative transfer equation, (2.2.5), written in 1D and for a stationary state by powers of  $\mu$  and integrating to give

$$\frac{\partial}{\partial x} f_{phot}^{(i)} = - \left\{ \epsilon \left( 1 - e^{-\epsilon/k_B T} \right) \sum_n B_{12}^n N_1^n \phi_n(\epsilon) + n \sigma_s(\epsilon) \right\} f_{phot}^{(i-1)}. \quad (2.3.5)$$

The above form makes clear the infinite nature of this problem which must be overcome with simplifying assumptions. An important result can be found by looking at the energy flux through a material. We consider the moment equation (2.3.5) with  $i = 2$ , relating photon flux to pressure. Collecting terms and using the physical interpretation of the distribution moments then leads to the result

$$j_x(\epsilon) = \frac{-1}{N_a \sigma_a (1 - e^{-\epsilon/k_B T}) + n \sigma_s} \frac{c}{\epsilon} \frac{\partial}{\partial x} P_x, \quad (2.3.6)$$

which is general for a 1D system. Equation (2.3.6) still requires knowledge of the distribution function, and the only way such an expression can be applied is by making a further approximation. Under the assumption that the photon distribution is close to isotropic, then the above expression becomes

$$j_x(\epsilon) = -l(\epsilon)c \frac{\partial}{\partial x} \int \mu^2 f_0 d\Omega = -\frac{l(\epsilon)c}{3} \frac{\partial}{\partial x} f_0 ,$$

where  $l(\epsilon)$  is the photon mean free path

$$l(\epsilon) = \frac{1}{N_a \sigma_a (1 - e^{-\epsilon/k_B T}) + n \sigma_s (1 + \cos \theta)} . \quad (2.3.7)$$

Generalising to 3D results in

$$\mathbf{j}(\epsilon) = -\frac{l(\epsilon)c}{3} \nabla f_0 . \quad (2.3.8)$$

The above expression, describing the flux of particles due to an isotropic, inhomogeneous distribution function is a statement of the diffusion approximation, and is valid in situations where the mean free path of photons  $l(\epsilon)$  is much smaller than the dimension of the plasma system.

The diffusion approximation is exceptionally useful as large systems such as stars, or those with small photon mean free paths such as high  $Z$  plasmas are amenable to its application. The approximation can be put in a more useful form through the introduction of the Planck distribution to describe photons in thermal equilibrium, equation (2.2.4), which adds the requirement that  $l(\epsilon)$  is small compared to any temperature gradients. Then the total energy is given by the Stefan-Boltzmann law

$$u = \int_0^\infty \epsilon f_{\text{planck}}(\epsilon) d\epsilon = \frac{\pi^2}{15c^3 \hbar^3} (k_B T)^4 , \quad (2.3.9)$$

which allows the flux of energy  $\mathbf{F}$  to be written as

$$\mathbf{F} = -\frac{c}{3\rho} \frac{1}{\kappa_R} \nabla u . \quad (2.3.10)$$

In the above equation the Rosseland mean opacity  $\kappa_R$  and mean free path  $l_R(\epsilon)$  are defined by

$$\frac{1}{\kappa_R} = \rho l_R = \frac{15\rho}{4\pi^4} \int_0^\infty l(x) \frac{x^4 e^{-x}}{(1 - e^{-x})^2} dx . \quad (2.3.11)$$

The above expressions for the energy flux through a plasma is an extremely important relation in the calculation of plasma dynamics since it allows the calculation of the transport of energy between elements in a fluid code by photons. It is particularly useful as the gradient in  $u$  is easy to calculate when the photon temperature is known at different points in the plasma, and because the Rosseland mean opacity contains all of the details of the photon absorption and emission processes that occur in the plasma. This means that if the Rosseland mean opacity as a function of temperature and density is known, no atomic physics calculations are required. The calculation of the Rosseland mean, on the other hand, is a complex atomic physics problem which must be performed accurately in order to give a good description of the radiation in a system. It is also difficult to fully measure this quantity due to the large range of conditions that are required to model most plasma systems.

## 2.4 Emission and Absorption Spectra

The modelling of heat transport through the average opacity is not the only application of opacity calculations; the frequency resolved opacity is also of great importance in modern experimental plasma physics. In this section we describe how the measurable emission and absorption spectra of a plasma system are related to the opacity, and what information they can provide. Such measurements are extremely important in plasma physics due to the difficulties associated with making direct measurements of such volatile, unstable, and often distant, systems.

Spectroscopy has been of fundamental importance to many areas of physics for many years, and as such is very highly developed. Diffraction of light using prisms, gratings or crystals allows the accurate measurement of the spectral properties of a material, properties that provide a wealth of information about the micro- and macroscopic state (see section 2.5 below). The information reflected in the measured spectrum is encapsulated in the plasma opacity and as such this quantity is essential in understanding experiment.

The radiative transfer equation for an LTE plasma is taken from equation (2.2.5) along with the definition of the opacity (2.2.7):

$$\mu \frac{\partial}{\partial x} I(\epsilon) = -\kappa(\epsilon) \rho I(\epsilon) + \kappa(\epsilon) \rho I_{\text{planck}}(\epsilon) ,$$

where we have multiplied through by  $\epsilon$  to consider the distribution of intensities, and we consider a 1D plasma with negligible scattering. The general solution of this equation for forward propagating photons ( $0 \geq \mu \geq 1$ ) is

$$I(\epsilon, x) = I(\epsilon, 0) e^{-\frac{\tau(\epsilon)[0, x]}{\mu}} + \int_0^x \frac{\rho(x') \kappa(\epsilon, x')}{\mu} I_{\text{planck}}(\epsilon, x) e^{-\frac{\tau(\epsilon)[x', x]}{\mu}} dx' , \quad (2.4.1)$$

where  $\tau[x_1, x_2]$  is the optical depth between the points  $x_1$  and  $x_2$ ,

$$\tau(\epsilon)[x_1, x_2] = \int_{x_1}^{x_2} \rho(x) \kappa(\epsilon, x) dx , \quad (2.4.2)$$

defined as the mass absorption coefficient integrated along the line of sight between the two positions in the plasma. For a homogeneous plasma this simplifies to

$$I(\epsilon, x) = I(\epsilon, 0) e^{-\rho \kappa(\epsilon) x} + I_{\text{planck}}(\epsilon) \left( 1 - e^{-\rho \kappa(\epsilon) x} \right) , \quad (2.4.3)$$

where the first term describes the attenuation of the applied field  $I(\epsilon, 0)$  and the second describes emission from the plasma. In the above we have set  $\mu = 1$  to model a beam of photons travelling along the line of sight, and made explicit the dependence on the (now constant) opacity. In most opacity experiments one of two regimes will be used to infer the opacity, according to the value of the optical depth of the sample. In the first a very strong field is applied to the sample so that the Planckian self emission can be neglected. In this case equation (2.4.3) reduces to the Beer-Lambert law and the comparison of the applied and transmitted photon fields allows  $\kappa$  to be measured. To this end it is usual to plot the transmission  $T(\epsilon) = I(\epsilon, L)/I(\epsilon, 0)$ . Such a situation can also be achieved by ensuring the plasma is optically thin ( $\tau \ll 1$ ), keeping self emission small. The second option is to measure the emitted photon field with no applied background; in this case the frequency resolved emitted field is measured and compared to the final term in equation (2.4.3). A

convenient method of analysis is to expand the exponential in this term for small optical depth to obtain the opacity as a multiplicative modification to the Planckian. These experiments are convenient as they do not require a backlighter, however the sample must be of sufficient temperature in order to produce enough self-emission. The two types of opacity measurement are shown in figure 2.1.

Due to the form of the solution (2.4.3), experiments on plasmas which are inhomogeneous can be very difficult to analyse. For this reason much attention is given to ensuring that the region of plasma that is sampled is as free from temperature and density gradients as possible. A useful result can be found by considering the absorption due to a set of  $N$  optically thin, homogeneous slabs of plasma and passing from integration to summation in equation (2.4.1). The result is

$$I(\epsilon, x) = I(\epsilon, 0) \prod_{n=1}^N e^{-\tau_n} + \sum_{n=1}^N \tau_n I_{\text{planck}}(\epsilon, n) \left\{ \prod_{m=n+1}^N e^{-\tau_m} \right\},$$

which allows several opacity calculations for different plasma conditions to be combined to give an approximate correction for gradients. More complex cases which can occur in astrophysical plasmas require detailed analysis and further modelling to describe the temperature and density profiles in the plasma. This is particularly true in cases where optical depth is important, as the pumping of atomic transitions in one part of

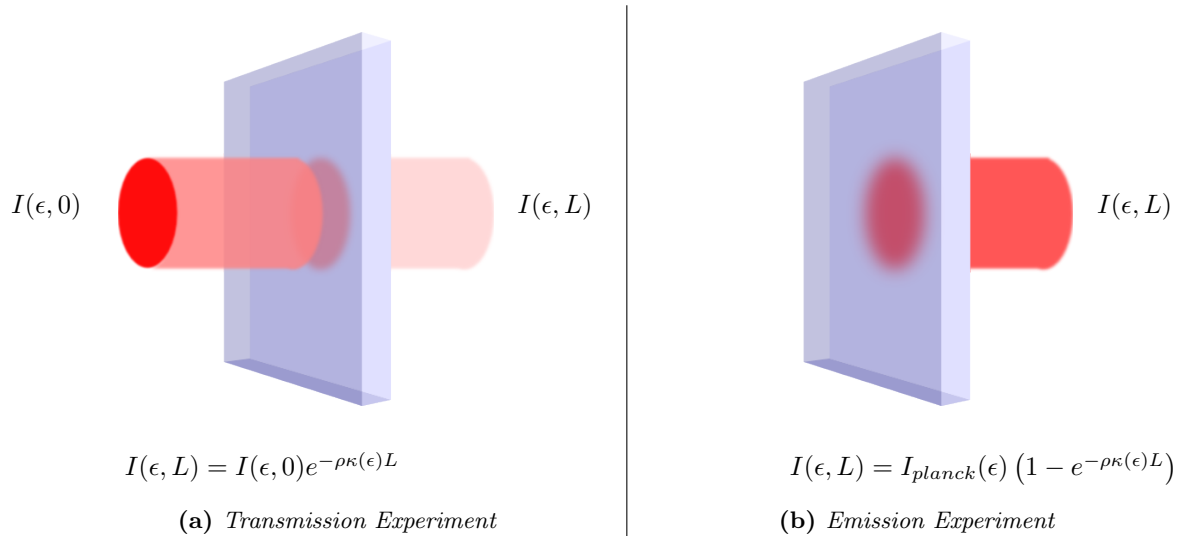


**Figure 2.1:** Cartoons of typical opacity experiments based on the solution of the radiative heat transport equation (2.4.3). In (a) the transmission of radiation through a plasma is used to measure its opacity; in (b) no field is applied and the emitted radiation is measured directly.

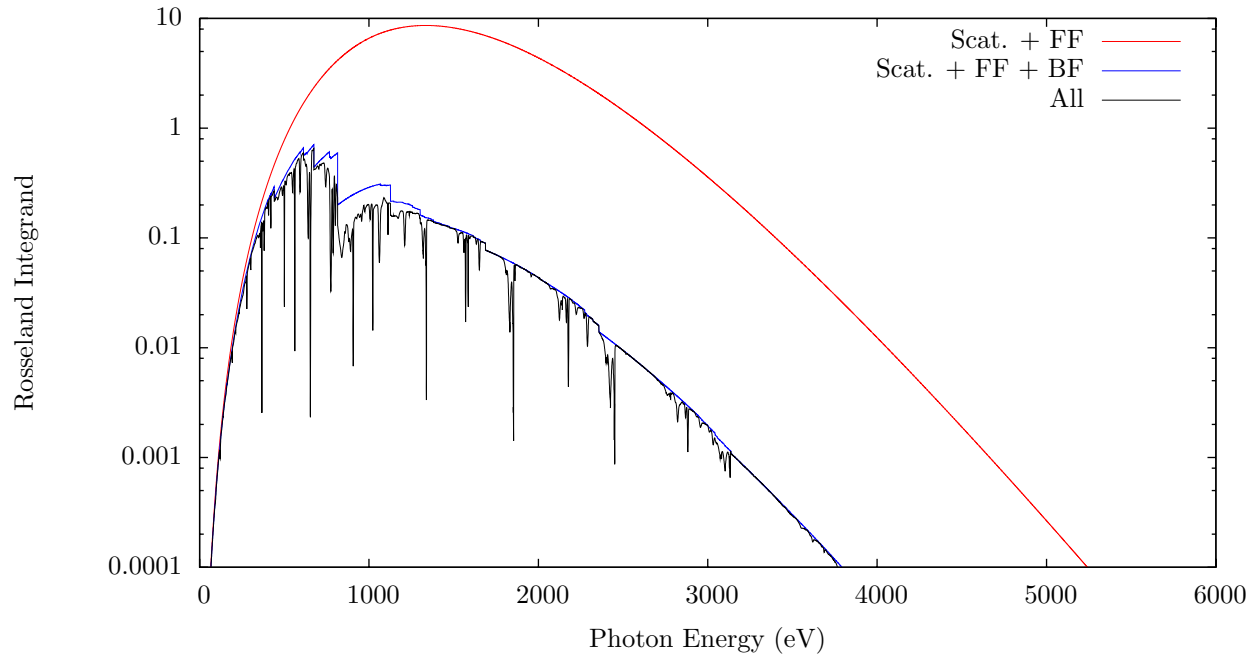


**Figure 2.2:** *The integrand of the Rosseland mean opacity, equation (2.3.11), for a Grevesse solar mixture of elements under the conditions at the base of the convective zone in the Sun. The various lines show the contributions of different processes; red gives the contribution of only scattering and free-free absorption, blue shows these plus bound-free absorption edges, and black shows the effects of all absorption mechanisms. The importance of absorption by ions is made clear in this figure; the large reduction in integrand due to absorption lines has a large effect on the Rosseland mean opacity.*

the plasma by radiation from another can have a dramatic effect on spectra. In this situation the assumption of LTE breaks down and a detailed, self consistent solution of the radiative heat transfer equation and ion populations must be found.

It is instructive to consider the effects of the various absorption processes we have discussed in the previous sections. Since the opacity is additive in the absorption rates and cross sections the assessment of their relative importance is simple. In figure 2.2 we show the contributions of each process to the Rosseland mean opacity by plotting the

| Included Processes       | Rosseland Mean ( $\text{cm}^2/\text{g}$ ) |
|--------------------------|---|
| Scattering + Free - Free | 1.13                                      |
| + Bound-Free             | 11.4                                      |
| + Bound-Bound            | 15.5                                      |

**Table 2.1:** *The Rosseland mean opacity at the base of the convective zone of the Sun, including various absorption processes.*

integrand of equation (2.3.11) as a function of photon frequency. The plot is for a Grevesse mixture of elements in the sun [20], and the conditions are  $T = 182\text{eV}$ ,  $\rho = 0.154\text{g/cc}$  corresponding to a radius of

around  $R = 0.72 R_{\odot}$  [21]. This is the radius at which convection is measured to start to occur in the sun, and as such the opacity under these conditions is a very important quantity in solar modelling [4]. The figure also shows the relative importance of the various different processes, as they are included into the description; the corresponding Rosseland mean opacities are shown in table 2.1. Continuous free-free absorption and scattering are included to begin with, giving a smooth integrand. Bound-free absorption is then added leading to a series of absorption edges that tend to bring the entire curve downwards, resulting to a change in the Rosseland mean of an order of magnitude. Finally, absorption lines are added leading to a further increase of 37%. This will lead to an equal decrease in energy flux and would have a significant effect on plasma simulations.

The opacity also has a very important role to play in the observation of plasma systems, due to its fundamental relationship with the emission profile and the way an applied radiation field will be absorbed. This relationship not only allows direct measurement of the opacity, it allows the application of opacity calculations in order to provide information that would be otherwise unavailable. These applications are described in detail in the following section, however it is important to note that in general it is the frequency resolved profiles that are of interest in this case; as such the extra structure that arises due to absorption by ions is essential in providing a reliable analysis.

## 2.5 Quantum Mechanical Description of Line Opacity

In this section we consider the quantum mechanical interaction between an electron and an electromagnetic field. This process, along with the notation used, is shown in figure 2.3; the interaction between the field of an incoming photon and an electron causes the absorption of the photon and a change of state of the electron. As explained in previous sections the absorption of photons in this way is described by a rate that is related to the strength of the EM field and to the quantum mechanics of the electron system. We aim to characterise an

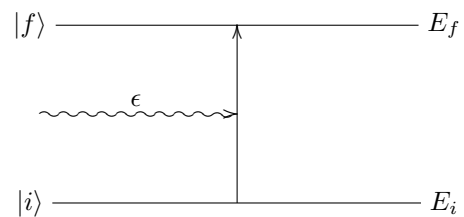


**Figure 2.3:** *The state and transition notation used in this thesis. The absorption of a photon of energy  $\epsilon$  causes a transition from state  $|i\rangle$  to state  $|f\rangle$ .*



absorption event in these terms by treating the EM field as a perturbation to the stationary electron system.

In order to describe the absorption of photons due to bound-bound electronic transitions it is necessary to characterise the resulting absorption lines. We start from the Hamiltonian for an electron moving in a potential  $V_0$  interacting with a radiation field of vector potential  $\mathbf{A}$  and scalar potential  $\phi$ ;

$$\hat{H} = \frac{1}{2m} (\mathbf{p} + e\mathbf{A})^2 - e\phi + V_0 , \quad (2.5.1)$$

and expand into component terms. Using the Coulomb gauge in which  $\nabla \cdot \mathbf{A} = 0$  and  $\phi = 0$  this becomes

$$\hat{H} = \frac{\mathbf{p}^2}{2m} + V_0 + \frac{e}{m} \mathbf{A} \cdot \mathbf{p} , \quad (2.5.2)$$

where we have neglected terms of order  $\mathbf{A}^2$ . The first two terms of the above equation define the electron system and confining potential, in other words the unperturbed atom. This is discussed in the following sections; at this stage it will be denoted  $\hat{H}_0$ . The final term describes interactions with the vector potential of the radiation and will be treated as a time dependant perturbation, and called  $V$ . In this case the time evolution of the atomic system due to the radiation field is described by the matrix elements of the time development operator  $\tilde{T}(t, t_0)$ , which is defined by the relations

$$|\tilde{\psi}(t)\rangle = \tilde{T}(t, t_0) |\tilde{\psi}(t_0)\rangle ; \quad (2.5.3)$$

$$|\tilde{\psi}(t)\rangle = e^{\frac{i}{\hbar} \hat{H}_0 t} |\psi(t)\rangle . \quad (2.5.4)$$

In the above equation the tilde denotes the interaction representation, defined by the transformation (2.5.4), which allows the time evolution of the electron states due to the EM field to be separated from other processes. The transition probability is given by the matrix elements (squared) of  $\tilde{T}$  between initial and final states. These are calculated using standard time dependant perturbation theory [22]; the result is

$$P_{if} = \frac{16\pi^4 e^2}{\hbar^2} \epsilon_{if}^2 |A(\epsilon_{if})|^2 |\langle f | \hat{\mathbf{e}} \cdot \hat{\mathbf{r}} | i \rangle|^2 ,$$

where  $\epsilon_{if} = \epsilon_f - \epsilon_i$  is the transition energy,  $A(\epsilon_{if})$  is the Fourier mode of the the radiation field at the transition energy, and  $\hat{\mathbf{e}}$  is the unit vector in the direction of polarisation of the field. In deriving the above expression we have invoked the ‘electric dipole approximation’ where the variation of the electric field over the range of the atomic state is neglected. This places limitations on the types of transitions that can occur, however these transitions are the strongest for elements with  $Z \lesssim 100$ . In our calculations we will only consider those transitions that can occur under this approximation, which are often termed E1 transitions.

Averaging over the vector  $\hat{\mathbf{e}}$  for unpolarised light and defining the absorption cross section in analogy with the scattering cross section results in

$$\int_{\Delta\epsilon} \sigma_a(\epsilon) d\epsilon = \frac{\pi}{3\epsilon_0 \hbar c} \epsilon_{if} |\langle f | e \hat{\mathbf{r}} | i \rangle|^2 .$$

The integral on the left is over the width of the absorption line, which is assumed to be small. In practice the initial and final states have some degeneracy in the magnetic quantum numbers  $m_i, m_f$ ; these are taken into account by averaging the absorption cross section over the initial states and summing over the final states, resulting in the total absorption cross section

$$\sigma_a = \frac{\pi}{3\epsilon_0 \hbar c} \frac{\epsilon_{if}}{g_i} \sum_{m_i, m_f} |\langle f, m_f | e \hat{\mathbf{r}} | i, m_i \rangle|^2 , \quad (2.5.5)$$

$$\equiv \frac{\pi}{3\epsilon_0 \hbar c} \frac{\epsilon_{if}}{g_i} S_{if} , \quad (2.5.6)$$

where we have defined the absorption line strength  $S_{if}$ . Another useful quantity is the oscillator strength for the transition, which is defined to relate the integrated cross section to the classical result;

$$\sigma_a = \frac{\pi \hbar e^2}{2\epsilon_0 m c} f_{if} ,$$

therefore

$$g_i f_{if} = \frac{2m}{3e^2 \hbar^2} \epsilon_{if} S_{if} . \quad (2.5.7)$$

The line strength is a usefull quantity since it is symmetric between the initial and final states ( $S_{if} = S_{fi}$ ).

In this thesis we will use the  $S_{if}$  notation given above with the defined relation to the oscillator strength  $f_{if}$ .

The results given above, along with the expression for the opacity (2.2.8), now allow the contribution to the opacity to be calculated in terms of the states of electrons in the plasma. These states are still to be determined; we will discuss this problem in the following sections.

## 2.6 Plasma Ionic Wavefunctions

The expressions for the opacity given above require the atomic wavefunctions of all ion states. In this section we give the framework with which these are formed.

### 2.6.1 General Results

In the following sections quantum theory will be used to analyse the problem of an ion in a plasma. Certain general results will be useful in this description, which we will introduce here.

We define the commutator of two operators  $[\hat{A}, \hat{B}]$  as

$$[\hat{A}, \hat{B}] = \hat{A}\hat{B} - \hat{B}\hat{A} , \quad (2.6.1)$$

which is very useful in analysing the general properties of a system. For example, if the commutator is zero then it is possible to find simultaneous eigenstates of the two operators  $\hat{A}$  and  $\hat{B}$ . A physical observable can have a definite value if the operator representing that observable commutes with the Hamiltonian  $\hat{H}$ . In this case the observable is a constant of motion and their associated quantum number is required to specify a particular state. Such quantum numbers are termed ‘good’.

We define the angular momentum through the classical result, replacing variables with operators in the usual way;

$$\hat{\mathbf{J}} = \hat{\mathbf{r}} \times \hat{\mathbf{p}} = -i\hbar \mathbf{r} \times \nabla ,$$

the components of which obey the commutation relations

$$[\hat{J}_i, \hat{J}_i] = 0, \quad [\hat{J}_i, \hat{J}_j] = i\hbar \hat{J}_k, \quad [\hat{J}_i, \hat{\mathbf{J}}^2] = 0, \quad (2.6.2)$$

where  $(i, j, k)$  are cyclic permutations of the components  $(x, y, z)$  of the vector operator  $\hat{\mathbf{J}}$ . Following Bethe and Salpeter [23] we will associate any vector operator satisfying (2.6.2) with an angular momentum. Finally note that since the components of  $\hat{\mathbf{J}}$  do not commute, only one can be known with precision; by convention we take this to be the  $z$  component  $\hat{J}_z$ . The square of the total angular momentum  $\hat{\mathbf{J}}^2 = \hat{\mathbf{J}}_x^2 + \hat{\mathbf{J}}_y^2 + \hat{\mathbf{J}}_z^2$  commutes with  $\hat{J}_z$  and using the properties given above it can be shown that the simultaneous eigenfunctions  $|jm\rangle$  satisfy [24]

$$\hat{J}^2 |jm\rangle = j(j+1)\hbar^2 |jm\rangle \quad j = 1/2, 1, 3/2, \dots, \quad (2.6.3)$$

$$\hat{J}_z |jm\rangle = m\hbar |jm\rangle \quad m = -j, -j+1, \dots, j. \quad (2.6.4)$$

In atomic physics we often encounter cases where different parts of the system move with different angular momenta. The angular momenta necessarily describe different subsets of the system's co-ordinates but they do not have to be independent, since any interaction between their respective co-ordinates means that the motion of one will exert a torque on the other. This torque then breaks the conservation of the individual angular momenta and it is only the total that is a constant of the motion [25]. It is, therefore, useful to analyse the possible values of the total angular momentum when two systems are added together. This analysis makes no assumptions regarding the interaction between the two systems and so the individual momenta may or may not be conserved.

We describe the angular momenta of the component systems through the operators  $\hat{\mathbf{J}}_1$  and  $\hat{\mathbf{J}}_2$ , and the total as

$$\hat{\mathbf{J}} = \hat{\mathbf{J}}_1 + \hat{\mathbf{J}}_2.$$

Then we describe the total angular momentum through the quantum numbers  $J$  and  $M$ , representing the magnitude and orientation ( $z$  component) respectively. The definition of the total angular momentum gives

the trivial result  $M = m_1 + m_2$ , and the commutation relations given above show that it is possible to find simultaneous eigenfunctions of the operators  $\hat{\mathbf{J}}^2$ ,  $\hat{J}_z$ ,  $\hat{\mathbf{J}}_1^2$  and  $\hat{\mathbf{J}}_2^2$ ; this means that the state of total  $JM$  resulting from  $j_1$  and  $j_2$  is a mixture of states of different  $m_1$ ,  $m_2 = M - m_1$ . Then for given values of  $j_1$  and  $j_2$  the possible values of  $J$  and  $M$  are determined by the possible combinations of  $m_1$  and  $m_2$ . This gives

$$J = j_1 + j_2, j_1 + j_2 - 1, \dots, |j_1 - j_2|,$$

and the wavefunction can be expanded as a linear combination of eigenfunctions of the individual angular momenta [25]

$$|j_1 j_2 JM\rangle = \sum_{m_1} C_{j_1, m_1, j_2, M-m_1}^{J, M} |j_1 m_1\rangle |j_2 m_2\rangle, \quad (2.6.5)$$

$$= (-1)^{j_1 - j_2 + M} \sqrt{2J+1} \sum_{m_1} \begin{pmatrix} j_1 & j_2 & J \\ m_1 & m_2 & -M \end{pmatrix} |j_1 m_1\rangle |j_2 m_2\rangle. \quad (2.6.6)$$

In the above expression  $C_{j_1, m_1, j_2, M-m_1}^{J, M}$  is a Clebsch-Gordon coefficient,  $\begin{pmatrix} j_1 & j_2 & J \\ m_1 & m_2 & -M \end{pmatrix}$  is a  $3j$  symbol, and  $|j_1 m_2\rangle$  is the eigenfunction of the first angular momentum system. Note that since the total wavefunction given in equations (2.6.5) and (2.6.6) is a linear combination of product wavefunctions it does not necessarily reflect the antisymmetry of electron wavefunctions, which must be included in a full atomic model. This significantly complicates matters.

## 2.6.2 Relativistic Quantum Mechanics

The description of the unperturbed wavefunctions from which the transition strengths and absorption rates are calculated is a major part of an opacity calculation. The first stage in building these wavefunctions is to form a description of the single particle states that electrons can occupy, a problem which we will address in this section. Building a state vector for the entire ion requires further analysis which will be described in the following section. There are various levels of approximation; the first is nonrelativistic Schrödinger theory, where an electron moves in the confining potential with a potential energy much less

than its mass-energy. This model does not explicitly include the effects of electron spin or the variation of the electron's mass with velocity, however these results can be included through a perturbation analysis. For the hydrogenic case the result, expressed as the ratio of the relativistic energy perturbation to the nonrelativistic part of the energy, is [25]

$$\frac{\alpha^2 Z^2}{4n^2} \left[ \frac{4n}{j + 1/2} - 3 \right] .$$

For a  $1s_{1/2}$  core states of relevance to the absorption of X-rays, this exceeds 1% when  $Z > 27$ . Such mid to high  $Z$  elements are very important in determining the opacity of plasmas even when they occur in small concentrations, and so we will approach this problem using the fully relativistic Dirac theory. This process will also elucidate the effects of relativity as described above.

The relativistic motion of a single quantum mechanical particle is described through the Dirac equation [23];

$$\begin{aligned} \hat{H}|\psi\rangle &= i\hbar \frac{\partial}{\partial t} \psi = \epsilon|\psi\rangle , \\ \hat{H} &= V(\mathbf{r}) + \beta mc^2 + \boldsymbol{\alpha} \cdot (c\hat{\mathbf{p}} + e\mathbf{A}) , \end{aligned} \quad (2.6.7)$$

where  $V(\mathbf{r})$  and  $\mathbf{A}$  are the scalar and vector potentials for all fields in the system and  $\hat{\mathbf{p}}$  is the momentum operator. The Dirac and Pauli matrices are  $\boldsymbol{\alpha}, \beta$  and  $\boldsymbol{\sigma}$  respectively;

$$\boldsymbol{\alpha} = \begin{pmatrix} 0 & \boldsymbol{\sigma} \\ \boldsymbol{\sigma} & 0 \end{pmatrix} , \quad \beta = \begin{pmatrix} \mathbf{I} & 0 \\ 0 & -\mathbf{I} \end{pmatrix} , \quad (2.6.8)$$

$$\sigma_1 = \begin{pmatrix} 0 & 1 \\ 1 & 0 \end{pmatrix} , \quad \sigma_2 = \begin{pmatrix} 0 & -i \\ i & 0 \end{pmatrix} , \quad \sigma_3 = \begin{pmatrix} 1 & 0 \\ 0 & -1 \end{pmatrix} , \quad \mathbf{I} = \begin{pmatrix} 1 & 0 \\ 0 & 1 \end{pmatrix} . \quad (2.6.9)$$

The above description implicitly includes electron spin. It should be noted that the Dirac equation defines electron wavefunctions with four components rather than just one in the Schrödinger picture. Defining the

spin, orbital and total angular momentum operators as

$$\hat{\mathbf{S}} = \frac{1}{2}\hbar\boldsymbol{\sigma} , \quad (2.6.10)$$

$$\hat{\mathbf{L}} = \hat{\mathbf{r}} \times \hat{\mathbf{p}} , = i\hbar\hat{\mathbf{r}} \times \boldsymbol{\nabla} \quad (2.6.11)$$

$$\hat{\mathbf{J}} = (\hat{\mathbf{L}} + \hat{\mathbf{S}}) , \quad (2.6.12)$$

with associated quantum numbers  $s, m_s, \ell, m_\ell, j, m_j$  (defined in analogy with the general results (2.6.3) and (2.6.4)) we arrive at the important results [23] ;

- $[\hat{\mathbf{L}}^2, \hat{\mathbf{J}}^2] = [\hat{\mathbf{S}}^2, \hat{\mathbf{J}}^2] = 0$

It is possible to find simultaneous eigenvectors of the magnitudes of all three angular momenta

- $[\hat{J}_z, \hat{\mathbf{L}}^2] = [\hat{J}_z, \hat{\mathbf{S}}^2] = 0$

Similarly, the z component of the total angular momentum can still be defined along with  $\ell$ ,  $s$  and  $j$ . This result, together with the previous, agrees with the previous section in which it was suggested that for a state with a well defined total angular momentum, only the magnitudes of the component vectors retain their meaning.

- $[\hat{L}_i, \hat{J}_z], [\hat{S}_i, \hat{J}_z] \neq 0 \quad ; \quad i = x, y, z$

The components of the angular and spin angular momenta cannot be fixed simultaneously with the values of the angular momenta described above.

- $[\hat{\mathbf{L}}, \hat{H}] = -[\hat{\mathbf{S}}, \hat{H}] = i\hbar\boldsymbol{\alpha} \times \hat{\mathbf{p}} \quad (\text{Central Potential})$

In the relativistic theory the components of the spin and orbital angular momenta are not constants of motion, as opposed to the nonrelativistic theory in which they are conserved. This is a consequence of the interaction between spin and orbital angular momenta. However this result leads to

- $[\hat{\mathbf{J}}, \hat{H}] = [\hat{\mathbf{L}}, \hat{H}] + [\hat{\mathbf{S}}, \hat{H}] = 0 \quad (\text{Central Potential})$

Then the magnitude and direction of the total angular momentum operators,  $j$  and  $m_j$ , are good quantum numbers. This is a fundamental result for any system with a central potential.

- $[\hat{\mathbf{S}}^2, \hat{H}] = 0$

The magnitude of the spin angular momentum is well defined along with the energy. This is not the case for the magnitude of the orbital angular momentum, which Bethe & Salpeter show to have a non-conserved component of order  $(\frac{v}{c})^2$ .

These results now set the framework under which we will describe single electron states. The only good quantum numbers are  $s$ ,  $j$  and  $m_j$ , however we will see that in the weakly relativistic Pauli theory  $\ell$  is a good quantum number and so we retain this designation. States will be denoted using the usual principle quantum number  $n$  along with the quantum numbers  $j$  and  $m_j$  describing the magnitude and  $z$ -component of the total angular momentum respectively.

The effect of the relativistic treatment can be appreciated by expanding the various operators and identifying the gradient of the vector potential, to give the familiar equation

$$\left\{ -\frac{\hbar^2}{2m} \nabla^2 + V(\mathbf{r}) - \frac{1}{2mc^2} (E + e\phi)^2 - i\frac{e\hbar}{mc} (\mathbf{A} \cdot \nabla) + \frac{e^2}{2mc^2} |\mathbf{A}|^2 + \right. \\ \left. + \frac{e\hbar}{2mc} (\boldsymbol{\sigma} \cdot \mathbf{H}) - i\frac{e\hbar}{2mc} (\boldsymbol{\alpha} \cdot \mathbf{E}) \right\} |\psi\rangle = E|\psi\rangle . \quad (2.6.13)$$

The first two terms of this equation are the terms of the nonrelativistic Schrödinger equation; the next term represents the variation of electron mass with velocity. The fourth and fifth terms result from the interaction with an applied vector potential as discussed in section 2.5, and the final two terms result from the electron spin interacting with induced magnetic and electric fields. In the case of a central field  $V(\mathbf{r}) \equiv V(r)$ , with no applied vector potential (which has already been treated as a perturbation), the final result is accurate to order  $(v/c)^2$  [23],

$$\left\{ -\frac{\hbar^2}{2m} \nabla^2 + V(r) - \frac{1}{2mc^2} (E - V(r))^2 - \left( \frac{\hbar}{2mc} \right)^2 \left( \frac{dV}{dr} \right) \left( \frac{\partial}{\partial r} - \frac{2}{r} \mathbf{L} \cdot \mathbf{S} \right) \right\} |\psi\rangle = E|\psi\rangle . \quad (2.6.14)$$

In this expression it is clear that the mass variation term is present in its original form, but the interaction of the electron spin with self-generated fields have simplified into the Darwin and spin orbit interactions. The Darwin term describes the variation in the potential energy due to the non-localised nature of the electron.



The final term, the spin orbit interaction, is very important in relativistic calculations as it represents an interaction energy between the orbital and spin angular momenta of the electrons. It should be noted that in this approximation, which is the basis of the Pauli theory, the Hamiltonian commutes with  $\hat{\mathbf{L}}^2$  and so  $\ell$  is a good quantum number (this is not the case in the Dirac theory).

Returning to the Dirac Hamiltonian (2.6.7) the form of the eigenvectors can be found using the angular momentum properties described earlier. We begin by forming a simultaneous eigenfunction of  $\hat{\mathbf{L}}^2$ ,  $\hat{\mathbf{S}}^2$ ,  $\hat{\mathbf{J}}^2$  and  $\hat{J}_z$  as before;

$$\chi_{\ell jm_j} = \sum_{m_s} C_{\ell, m_j - m_s, 1/2, m_s}^{j, m_j} Y_{\ell}^{m_j - m_s} \xi_{1/2}^{m_s}, \quad (2.6.15)$$

where  $Y_{\ell}^{m_i}$  is a spherical harmonic, and  $\xi_s^{m_s}$  is a two component spin eigenfunction. Since for a single electron we know that  $j = \ell \pm 1/2$  it is customary to combine the state designations  $\ell$  and  $j$  into a single quantum number  $\kappa$  where

$$\kappa = \begin{cases} -(\ell + 1) & \text{if } j = \ell + 1/2 \\ \ell & \text{if } j = \ell - 1/2 \end{cases}.$$

We have also noted that in the full Dirac theory, the eigenfunctions of the Hamiltonian commute with  $\hat{\mathbf{S}}^2$ ,  $\hat{\mathbf{J}}^2$  and  $\hat{J}_z$  but not  $\hat{\mathbf{L}}^2$ ; then following Grant [26] we form our four component wavefunctions as

$$|\psi\rangle = \begin{pmatrix} i\chi_{-\kappa m} \frac{Q(r)}{r} \\ \chi_{\kappa m} \frac{P(r)}{r} \end{pmatrix}, \quad (2.6.16)$$

which since  $j = |\kappa| + 1/2$  has the correct properties. We have already seen that the relativistic treatment causes mixing of electron states of the same  $\ell$ ; in the above form it can now be seen that  $Q(r)$  describes the component with  $\ell = j + 1/2$  and  $P(r)$  the component with  $\ell = j - 1/2$ . In the Pauli theory one of these components is neglected, hence  $\ell$  is well known. When the above wavefunction is operated on by the Hamiltonian (2.6.7) with no vector potential and a central field it becomes

$$\hat{H}\Psi = \begin{pmatrix} i\chi_{-\kappa m} \left[ \hbar c \left( \frac{d}{dr} + \frac{\kappa+1}{r} \right) \frac{P(r)}{r} + (V(r) + mc^2) \frac{Q(r)}{r} \right] \\ \chi_{\kappa m} \left[ -\hbar c \left( \frac{d}{dr} - \frac{\kappa-1}{r} \right) \frac{Q(r)}{r} + (V(r) - mc^2) \frac{P(r)}{r} \right] \end{pmatrix}. \quad (2.6.17)$$

The differential equations in the above expression play the part of the usual formula for the radial part of the wavefunction in normal Schrödinger theory. It is these expressions that must be solved in order to describe the possible states of a single electron in a fully relativistic treatment. The explicit dependence on  $\kappa$  demonstrates that in such a description the single electron energies will depend on  $j$  due to the inclusion of the spin-orbit interaction (as expected from the earlier perturbation analysis). For a given potential the wavefunctions can be found through minimisation of the energy eigenvalue; the problem of finding the potential is discussed in later sections.

## 2.7 Quantum Mechanics of Many Electron Atoms

Elements with a mid to high nuclear charge  $Z$  produce a large potential well and so even at high temperatures such atoms will retain a large number of bound electrons. As an example consider figure 2.4 in which we plot the average ionisation of iron along the density and temperature track of the sun. Even under conditions of  $T \sim 1.3$  KeV and  $\rho \sim 150$  g/cc (beyond the range of current experiments) in the core, iron atoms retain more than 6 bound electrons. Clearly the single electron picture developed in the previous section is not appropriate.

The state of an ion is described by the many electron Hamiltonian, which is the sum of the single electron result (2.6.14) with the potential equal to the interaction of each electron with the nucleus, and each other electron;

$$\hat{H} = \sum_i \left[ -i\hbar \boldsymbol{\alpha}_i \cdot \boldsymbol{\nabla}_i + \beta mc^2 - \frac{1}{4\pi\xi_0} \frac{Ze^2}{r_i} \right] + \sum_{i>j} \frac{e^2}{4\pi\xi_0} \frac{1}{r_{ij}}, \quad (2.7.1)$$

where  $r_i = |\mathbf{r}_i|$ ,  $r_{ij} = |\mathbf{r}_i - \mathbf{r}_j|$ , and we have neglected all the relativistic terms besides the spin-orbit interaction. The first term is a sum of single electron Dirac operators for each electron, which we have discussed in the previous section. As described previously this causes a coupling of the orbital and spin angular momenta of each electron orbital. Finally the Coulomb interaction between electrons is included. This final term depends on the angular distribution of the two electrons, and therefore constitutes an interaction between their orbital angular momenta.

Together, the spin-orbit and Coulomb interactions mean that it is only the total angular momentum

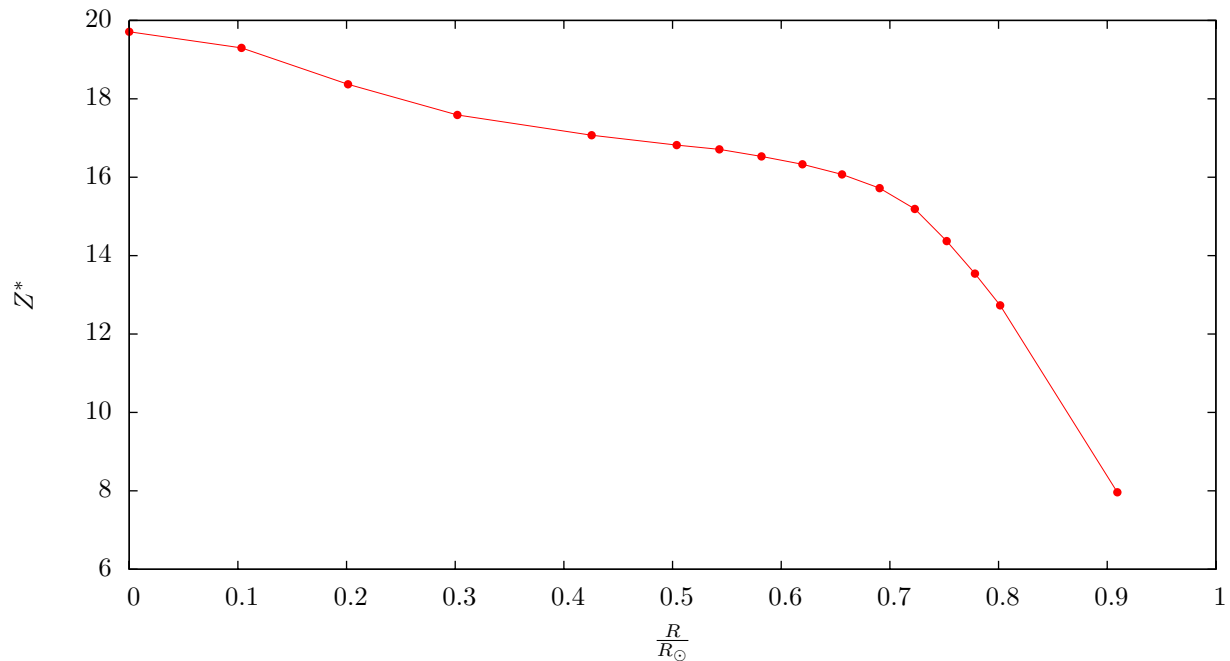


**Figure 2.4:** The average ionisation of iron ( $Z = 26$ ) along the temperature and density track of the sun. Calculations were performed using the a Grevesse mixture of 20 elements [20] and the IMP equation of state routines. Even under the very high temperatures and densities of the solar core, iron retains 6 bound electrons, which must be treated using many electron atomic physics. In modern experimental plasma physics such conditions are not currently accessible, making this treatment even more important. It is also interesting to notice that the position where the ionisation suddenly drops corresponds to the predicted base of the convective zone, hinting that these many electron ions are important for solar modelling.

of the atom that is conserved, and so the only good quantum numbers are  $J$  and  $M$ . The possible values of these quantum numbers are determined by the allowed combinations of the component momenta as described in section 2.6. The Hamiltonian explicitly depends on these quantum numbers and so the different arrangements of component momenta will have different energies, but not necessarily different values of  $J$  and  $M$ . It is therefore useful to retain some quantum numbers that are not conserved but do describe the details of the coupling that gives rise to a particular energy level. These individual energies all arise from the same configuration but have different wavefunctions, and so an opacity calculation should have the capacity to describe each one in some way.

The calculation of the details of these states can be approached in several ways, the most popular being the Slater-Condon method [27, 28] which is based on the fact that the eigenfunctions of an operator are left unchanged by an orthogonal transformation; hence the Hamiltonian can be represented using any basis

set and diagonalised, to give the correct eigenfunctions and eigenvalues. The volume of work required is greatly effected by the proximity of the initial basis set to the eigenfunctions (ie, the magnitude of the off-diagonal elements of  $\hat{H}$  in the initial representation). In modern calculations basis functions are generated by neglecting one or other of the coupling terms in  $\hat{H}$  and using the powerful Racah algebra [29, 30, 31] to form the Hamiltonian. This can then be numerically diagonalised to find the correct wavefunctions and energies.

The numerical diagonalisation of the Hamiltonian is a time consuming process and must be performed for every ion configuration in an opacity calculation. For this reason fast opacity models tend to use a simplified model in which the set of  $J$  values arising from a given configuration are described by a single energy, equal to the mean energy of all levels of the configuration. Electrons are assumed to move independently in a central potential due to the nucleus and all other electrons, which is found using self consistent field models (described in the following sections). In this case the single electron wavefunction can be found as given in the previous section (see equations (2.6.15)-(2.6.17)) and the many electron wavefunction is given by the Slater determinant

$$|\Psi\rangle = \frac{1}{\sqrt{N!}} \begin{vmatrix} \psi_1(\mathbf{r}_1) & \psi_2(\mathbf{r}_1) & \cdots & \psi_N(\mathbf{r}_1) \\ \psi_1(\mathbf{r}_2) & \psi_2(\mathbf{r}_2) & \cdots & \psi_N(\mathbf{r}_2) \\ \vdots & \vdots & \ddots & \vdots \\ \psi_1(\mathbf{r}_N) & \psi_2(\mathbf{r}_N) & \cdots & \psi_N(\mathbf{r}_N) \end{vmatrix}. \quad (2.7.2)$$

In this expression the subscript is shorthand for the quantum numbers  $n\ell jm_j$ . Since the spin-orbit interaction is included in the determination of single electron wavefunctions and the electron-electron interaction is approximated in the central potential, no further angular momentum coupling is performed and the above is assumed to describe the wavefunction in full. This is therefore a  $jj$  coupled approximation, appropriate for strongly relativistic situations in which the spin orbit coupling dominates over Coulomb interactions. The energy of a configuration, defined by the set  $\{n\ell j\}$ , is simply the expectation value of the Hamiltonian for this state averaged over the quantum numbers  $\{m_j\}$ . For a general determinantal wavefunction the

configuration energy has the form

$$E = \sum_{i=1}^N I_i + \sum_{i=1}^N \sum_{j=1}^N H_{ij} , \quad (2.7.3)$$

where  $I_i$  is the single electron energy, and  $H_{ij}$  is the interaction energy between the  $i^{\text{th}}$  and  $j^{\text{th}}$  electron.

Grant [26] showed that for a determinantal wavefunction made up of relativistic single particle orbitals (2.6.16) these are

$$I_i = -c \times \int_0^\infty \left\{ P_i \left[ \hbar \left( \frac{d}{dr} - \frac{\kappa_i}{r} \right) Q_i + \left( mc + \frac{1}{4\pi\epsilon_0} \frac{Ze^2}{cr} \right) P_i \right] - Q_i \left[ \hbar \left( \frac{d}{dr} + \frac{\kappa_i}{r} \right) P_i + \left( mc - \frac{1}{4\pi\epsilon_0} \frac{Z}{cr} \right) Q_i \right] \right\} dr , \quad (2.7.4)$$

and

$$H_{ij} = -\frac{e^2}{4\pi\epsilon_0} \sum_k \left\{ d^k(j_i m_i; j_i m_i) d^k(j_j m_j; j_j m_j) F_{ij}^k - [d^k(j_i m_i; j_j m_j)]^2 G_{ij}^k \right\} , \quad (2.7.5)$$

where the  $F_{ij}^k$  and  $G_{ij}^k$  are Slater integrals [27] and the angular coefficients are given by Grant to be

$$d^k(j_1 m_1; j_2 m_2) = (-1)^{\frac{1}{2} + m_2 + 2(j_1 - j_2)} \sqrt{(2j_1 + 1)(2j_2 + 1)} \begin{pmatrix} j_1 & j_2 & k \\ \frac{1}{2} & -\frac{1}{2} & 0 \end{pmatrix} \begin{pmatrix} j_1 & j_2 & k \\ -m_1 & m_2 & m_2 - m_1 \end{pmatrix} . \quad (2.7.6)$$

Averaging over the possible values of  $m_i$  and  $m_j$  then results in the average-of-configuration interaction energy

$$\bar{H}_{ij} = F_{ij}^0 - \frac{2j_1 + 1}{2j_i + 1 - \delta_{ij}} \sum_{k \geq \delta_{ij}} \begin{pmatrix} j_i & j_j & k \\ \frac{1}{2} & -\frac{1}{2} & 0 \end{pmatrix}^2 G_{ij}^k , \quad (2.7.7)$$

the second term of which is the exchange energy that results from the use of determinantal wavefunctions. In the above approximation, the modification of the total wavefunction due to the electron-electron interaction is neglected, however this is included in the configuration energy. In IMP calculations of configuration energies single electron radial wavefunctions are found by minimising the energy of electron states (equation 2.6.17) for a given potential using the method of Desclaux *et al.* [32], and the resulting Slater integrals are used in equation (2.7.7). The calculation of the potential is performed in the average atom approximation

and so the  $I_i$  and  $H_{ij}$  do not depend on the details of the configuration (although the configuration energy does since the summations in equation (2.7.3) are over occupied shells only) and so the energy of a transition is simply the difference between the average-of configuration energies. For an  $i \rightarrow f$  transition the transition energy is then

$$\epsilon_{fi} = I_f - I_i + \sum_{k \in C_f} H_{fk} - \sum_{k \in C_i} H_{ik} , \quad (2.7.8)$$

where as before the summation runs over all occupied states of the initial and final configurations  $C_i$  and  $C_f$ . Finally, we calculate the single electron transition strength using the sum rule [25]

$$S_{if} \equiv \sum_{m_i m_f q} |\langle j_f m_f | r \mathbf{C}_q^{(1)} | j_i m_i \rangle|^2 = e^2 |\langle j_f || r \mathbf{C}^{(1)} || j_i \rangle|^2 ,$$

where  $\mathbf{C}^{(1)}$  is a vector operator representing the spherical harmonics with  $\ell = 1$ . The final result is [33]

$$S_{if} = e^2 (2j_i + 1)(2j_f + 1) \begin{pmatrix} j_i & 1 & j_f \\ \frac{1}{2} & 0 & \frac{1}{2} \end{pmatrix}^2 \left[ \int (P_i P_f + Q_i Q_f) r dr \right]^2 , \quad (2.7.9)$$

which allows the fast evaluation of the linestrength from radial wavefunctions.

## 2.8 Plasma - Ion Interactions

The quantum mechanical description developed in the preceding sections deals with an atom that consists of a set of electrons interacting with the nucleus and with each other. These are then perturbed by a radiation field. In a plasma, where the atom is surrounded by other atoms of various ion stages and by other electrons, the picture is much more complicated. In order to gain a realistic picture of an atomic system the interactions with these other particles must be taken into account; these interactions are a very interesting feature of plasma systems and provide valuable information about the properties of the system. In this section we will discuss two of the most important effects of the surrounding plasma on our calculations, the change in atomic energy levels due to the background charge density, and due to high frequency fluctuations in local fields due to plasma motion.

The nature of the interactions with other particles, and therefore the way they must be described, depends

on the plasma conditions and on the particle with which the atom interacts. We can split these interactions into two types according to their effect on atomic spectra; the first will be those that cause an almost constant shift in the positions of electronic energy levels, both relative to each other and relative to the free electrons. Such interactions should be taken into account in the calculation of the electron energy levels of plasma ions. The other type will be interactions that randomly perturb energy levels producing a change in the width and shape of transition lines. Such line broadening effects can be taken into account through the lineshape function used previously.

At low temperatures or high density where atoms are closely packed the formation of molecules and electron energy bands has a significant effect on spectra, the description of which requires a detailed treatment of the positions of other atoms [34]. With increasing temperature or decreasing density a given atom will interact with other atoms less and less, allowing the interaction to be taken into account using the average arrangement of atoms in the plasma. The detail to which this distribution is described is determined by the plasma conditions and the accuracy desired.

The formation of a model for the effect of the plasma on bound energy levels requires a description of the charge density due to the plasma inside and around the ion in question since this charge density modifies the potential felt by electron states. The interaction of bound electrons with this extra plasma density will then appear alongside the nuclear and interelectron potentials in the Dirac equation and modify energies and wavefunctions. The suitability of the model chosen is largely determined by the extent to which plasma electrons and ions are found within the confines of the ion bound states; to that end it is convenient to define an ‘ion cell’ as the average volume occupied by an atom in the plasma and to consider the potential inside and outside of this volume.

In the very low density case the interaction between the internal structure of the ion system and the surrounding plasma can be neglected; the ion can then be considered as a point of charge  $Ze$  immersed in a plasma consisting of electrons and various ions of charge  $Z_i e$ . Calculating the density of these charges using Maxwell-Boltzmann statistics and finding the self-consistent potential from the Poisson equation results in

the Debye-Hückel (DH) theory. This predicts a potential surrounding the central ion

$$V(r) = \frac{Ze}{4\pi\epsilon_0} \frac{e^{-r/\lambda_D}}{r}, \quad (2.8.1)$$

where  $\lambda_D$  is the Debye length for the plasma,

$$\lambda_D = \sqrt{\frac{\epsilon_0 k_B T}{e^2 [N_e + \sum_i Z_i^2 N_i]}}, \quad (2.8.2)$$

and  $N_e$ ,  $N_i$  are the average densities of the electrons and the  $i^{\text{th}}$  ion species respectively. It can be seen that the effect of the plasma is to screen the nuclear potential over a characteristic length  $\lambda_D$ ; the assumption that this screening is not significant within the atom requires that the Debye length is much larger than the radius of an ion. Although the energy levels of the ion are not greatly changed the release of an electron from the central atom will change the internal interaction energy of the surrounding plasma. This leads to a change in the ionisation energy of the central ion,

$$\Delta E = -2ZE_H \left( \frac{a_0}{\lambda_D} \right),$$

where  $E_H$  is the ionisation energy of Hydrogen and  $a_0$  is the Bohr radius. It can be seen that weakly bound states with low ionisation energies are shifted to positive energy; this process is known as ‘pressure ionisation’ and is very important in many plasma systems. The various approximations in the DH theory mean that it is only valid for weakly coupled plasmas and for radii that are well outside the ion radius.

For higher densities, the penetration of the ion cell by free electrons becomes significant and these act to partially screen the nucleus from the bound electrons. In this case the ‘ion-cell’ model is more appropriate, in which bound and free electrons are confined to the ion cell and their charge density is used to calculate the potential. It is assumed that plasma ions do not enter the central ion cell and so charge neutrality requires that the total charge in the ion cell is zero; this means that the electric field and potential are zero at the ion cell boundary. Finally, the positive and negative charges outside the cell are assumed to cancel at all points in space so that the potential is always zero there. This allows the ion cell model to be invoked



through boundary conditions on the equations governing the atomic potential. This schematic can be used to develop various models that provide a total atomic potential for use in the solution of the Dirac equation. The various possibilities are discussed in the following section.

Alongside the methods described above in which the free electron and (to a certain extent) ion densities are treated correctly in the atomic model, opacity codes can use detailed models of isolated atoms followed by a perturbation analysis to find the shift in energy levels due to a given plasma potential. This has the advantage that a library of atomic states can be built for use with plasmas of all temperatures and densities and the effects of the plasma added later; a large part of the computational effort is then separated from the formation of the opacity. The IMP calculations that we will describe in this thesis use the ion-cell approach and so most of the discussions given later are relevant to this.

The models that we have described above allow the average density profile of the surrounding plasma to be taken into account when calculating atomic energy levels, and therefore on transition line positions and strengths. The accuracy with which the plasma density is calculated determines the accuracy of these shifts. In actuality the density profile depends on the atomic state; this self consistency is not included in the average atom models we consider in the majority of this thesis. The plasma constituents also have an effect on opacity calculations since they may not be static on the timescale of atomic transitions; the interaction energy between the two ‘optical’ atomic states involved in absorption (or emission) and the surrounding plasma can change during the transition. This changes the energy and strength, and when averaged over the plasma a given transition line acquires a shape that reflects the motion of the plasma and the interaction potential between plasma and atom.

In our calculations we use the ion-sphere model, which includes an approximate description of the distribution of plasma ions and electrons. The most important effect that is left out of this model is that of the interaction with the high frequency fluctuations in the electric field on the atom due to fast-moving (compared to ions) electrons. The effect of an applied electric field is known as the Stark effect; the change in the energy states of an atom are given by the matrix elements of the interaction with the field. For a

general atomic state  $|\gamma JM\rangle$  in a weak field, perturbation theory gives

$$\Delta E_{\gamma JM} = 4e^2 |\mathbf{E}|^2 \sum_{\gamma' J'} \begin{pmatrix} J & 1 & J' \\ -M & 0 & M \end{pmatrix}^2 \frac{\langle \gamma J \| \sum_i \mathbf{r}_i \| \gamma' J' \rangle^2}{E_{\gamma J} - E_{\gamma' J'}},$$

where following Cowan [25] we use  $\gamma$  to denote all other quantum numbers required to specify the state, and we have used the Wigner-Eckart theorem to separate out the angular dependence of the matrix element. The main features of this expression are the quadratic dependence on the electric field strength, which is a result of the weak field treatment, and the asymmetry around the unperturbed ( $M$  degenerate) level. The electric field acts to split the levels belonging to a given  $\gamma J$  and to shift their centre of gravity - absorption lines are then split and shifted. In the case of a fluctuating field, absorption lines will be broadened and shifted according to the probability distribution of the electric field at the atom.

Modelling Stark broadening in a plasma then requires a description of the interaction between the motion of electrons in the plasma and the atom in question. The first attempt at this was made by Lorentz [35], and his model reproduces the important features. The interaction of the atom with a plasma electron is considered to halt the absorption of the EM field - such collisions occur at a given rate  $\tau$ . The pulse lengths of the incoming radiation that can be absorbed are then described by Poisson statistics, which when Fourier transformed gives the lineshape. This treatment, in which the interaction with most electrons is weak and strong interactions occur infrequently is known as the ‘electron impact’ approximation; it is valid for reasonably low density and high temperatures. It results in a Lorentzian lineshape (which is a feature of the electron impact approximation), the width of which is equal to the inverse of the collision rate.

More accurate descriptions of the problem generally result in the same lineshape, but introduce a modified width and a shift in the line centre. Baranger gave a fully quantum mechanical treatment of the problem in a series of papers in 1958 [36, 37, 38], where the interaction of the atom with the potential due to electrons is taken into account, along with the motion of the perturbers in the potential due to the atom. This width and shift of the Lorentzian line is determined by the change in state of the perturbing electrons, and Baranger gives expressions for the line profile in terms of electron scattering amplitudes. We will investigate the application of this model in our opacity calculations in section 5.4.

### 3 Opacity Calculations

The theoretical background given in the previous section can be used to calculate the opacity of a given plasma to high accuracy. In practice, however, such a complete consideration of the physics involved is very time consuming and approximations must be made to make opacity calculations, and eventually in-line radiation-hydrodynamic simulations, feasible.

In this section we describe the approximations that are typically made to make this problem tractable. We pay particular attention to the models used in faster codes such as IMP (aspects of which will be described in detail), which necessarily use larger approximations than other models. Such codes provide a good test of the effectiveness of fast opacity models, a topic which is very important in the future development of in-line calculations, and one that forms a large part of the following chapters of this thesis.

#### 3.1 History

Opacity calculations have been of scientific interest since long before experimental plasma physics or its motivations existed. Early work on plasma opacity followed developments in astronomy and in particular solar modelling, and became very popular as astronomers started to try to make sense of the large variation in the measurable properties of stars. In particular the earliest developments were motivated by attempts to link the observable properties of stars to their internal structure, and by doing so to make sense of the ongoing stellar surveys.

Some of the earliest work was by Kramers in 1923 [39], who argued that the classical treatment of continuous absorption by plasmas should be sufficient to describe stellar structure. Eddington then made a series of important contributions [40] by realising that radiative equilibrium was essential to a star's structure. This then allowed the masses of stars to be related to their luminosity, making sense of the Hertzsprung-Russell diagram. He went on to show that the Kramers absorption cross section, which agreed with laboratory measurements, was far too low for his models of stars.

Spectral measurements of the Sun by Russell [41] helped to solve this problem by demonstrating the high number fraction of hydrogen in the sun, and the relative importance of heavy metals to spectral properties.

This work demonstrated that the modelling of stars, and in particular radiation transport, was much more complicated than previous work had assumed.

The early 1930s saw the birth of large-scale opacity calculations, based on the quantum mechanical analysis of continuous absorption by Gaunt [42, 43], and the calculations of Strömberg [44]. These were extended over the next 20 years [45, 46, 47], culminating in the publication of large opacity tables by Keller [48]. During this time, however, researchers were becoming more nervous about the neglect of absorption lines in the calculations [49], and alongside this the nuclear reactions responsible for energy production in the sun were discovered and used to provide more information on the composition of stars [50, 51].

By the early 1960s research computers were sufficiently powerful to allow the systematic investigation of the effect of absorption lines, and very quickly it was realised that they could not be neglected in many cases [52, 53, 54, 55]. It was during this time that the first problems were noticed with the depth of the convective zone in the sun, which was blamed for the so called ‘Li depletion problem’ [56]. Soon after, the pulsation periods of Cepheid variables were used to compare stellar pulsation and evolution theories with poor agreement [57, 58, 59]. Attempts to improve matters were focussed on larger and larger scale calculations, culminating in the well-known Los Alamos opacities [60], however these did not solve the solar modelling problems.

Lack of progress in explaining stellar pulsation prompted a re-examination of the theory used in these opacity calculations, after it was shown that an increase in the opacity of heavy elements ( $Z > 2$ ) could explain the Cepheid variable problem [61, 62]. In the late 1980s this increase was found by including  $\Delta n = 0$  transitions [63], term structure [64] and intermediate coupling [65, 66] using the new OPAL opacity code [67]. These improvements were quickly accepted as the solution [64], backed up by newly developed experimental techniques [68].

The development of laboratory approaches to opacity measurements provided a new focus for opacity codes, and saw the development of new models [1]; it quickly became clear that in many cases the atomic physics of the problem should be treated in as accurate a way as possible, giving birth to large projects such as the Opacity Project (OP) [69, 70] and OPAL codes releasing very detailed opacity tables for solar modelling.

At the start of the new millennium, the OP and OPAL codes were in good agreement despite using different approaches, which was interpreted as evidence that calculations were basically correct [71]. As was the case almost a century before, however, solar observations then demonstrated that there may be a problem when helioseismological measurements of the depth of convection zone disagreed with modelling by almost 19 error bars [9]. It has been suggested that this problem can be solved by a localised increase in the opacity close to the base of the convective zone, indicating a problem with the calculated opacity of heavy elements [4, 72]. Even more recently, very detailed observations of the abundances of these heavy elements have significantly reduced the predicted opacity [73, 74]; in order to agree with observations it has been suggested that a whole new source of opacity is required [75].

### 3.2 The Structure of Fast Plasma Opacity Calculations

The general starting point for most LTE plasma opacity calculations is the details of the elements in the plasma, their relative abundances, and the temperature and density of the plasma. The required output is the opacity in either frequency resolved or averaged form. The definition of the Rosseland mean (equation (2.3.11)) means that in fact the main result required is the frequency resolved opacity, which is needed to sufficiently high resolution and large enough range that the numerical integration of equation (2.3.11) will be accurate.

When in LTE, the plasma temperature and density of the plasma in question fully define the system, but the initial and final electron states that lead to the various components of the opacity cannot be expressed directly in terms of these variables. The first part of an opacity calculation must, then, build an atomic model for the plasma and solve it to provide all possible electron state wavefunctions and energies. We have discussed the formation of these quantities from fundamental quantum mechanics; the problem faced by opacity codes is then the determination of the potential in which the electrons move. This potential must include the electron-electron interaction which couples the atomic model and opacity to the details of the configuration being modelled. This represents a very large time penalty and so in many codes efforts are made to decouple atomic models from the generation of the opacity. The first way that this decoupling can be achieved is by considering as many contributions to the opacity as possible in an average way. To that

---

end we split the opacity into two contributions;

- Opacity due to free electrons - Scattering and free-free absorption are usually included using analytic models that depend on the average properties of the plasma, for example the average ionisation  $Z^*$ ,
- Opacity due to ions - The bound-bound and bound-free absorption processes are included through the quantum mechanical models described previously. These models are then simplified as described in the next section, in such a way that large portions of the atomic physics calculation are not required with ion configuration resolution.

In this way opacity codes can be split into several sections, which are shown diagrammatically in figure 3.1. Initially the state of the plasma must be found given information regarding the plasma temperature  $T$ , density  $\rho$ , and composition. This equation of state returns thermodynamic properties of the plasmas such as the pressure, chemical potential and average ionisation. Accurate models for this must be found self consistently with a quantum mechanical treatment of the ions, and so it is normal to combine the equation of state calculation with an atomic model that also calculates single electron energies and wavefunctions.

Following the completion of the atomic model and equation of state, the scattering and absorption by free electrons is included using analytic models. The advantage of such models is that a single loop over the output photon energy grid is required for each contribution; since the grid must be fine to allow the calculation of the Rosseland mean, this gives a significant time advantage. Similar models for the bound-bound and bound-free contribution can be used however these tend to be oversimplifications for radiative-transfer applications [76].

It is therefore necessary to perform configuration resolved calculation of bound-bound and bound-free absorption. This process involves the generation of all the ion stages that occur in the plasma, and then for each of these all important transitions of all the bound electrons. In this way each of the initial ion stages considered by the code contribute a large number of absorption lines and edges to the opacity. We will see in section 6 that it is convenient to consider all transitions in a given ion; the problem then reduces to ensuring that the most important ions are considered. We give a full discussion in section 6.

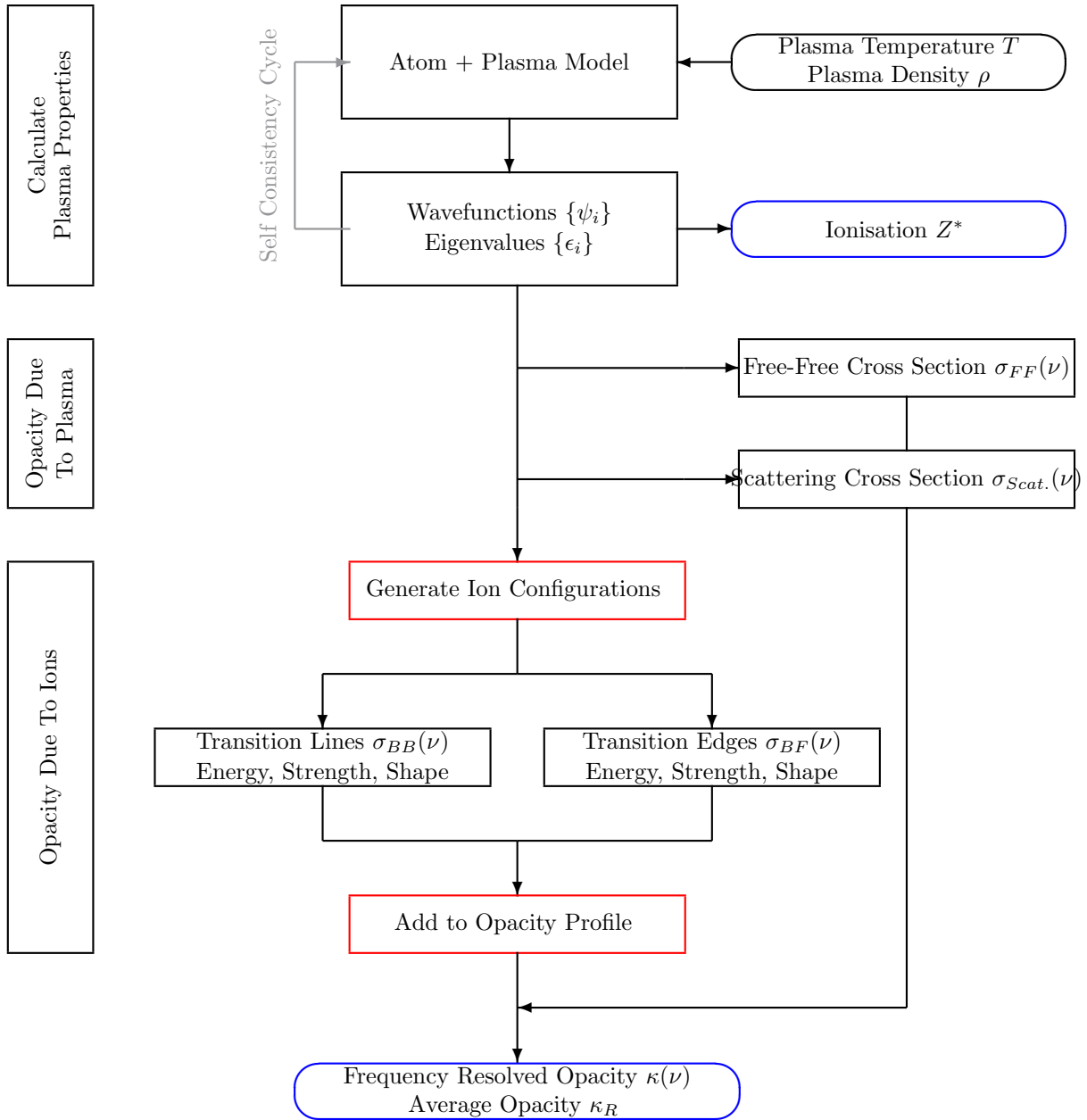


**Figure 3.1:** The general structure of opacity codes. Calculations can be split into a series of separate calculations which are then combined to give the full frequency resolved opacity. In the above blue ovals represent output from the code, and processes drawn in red account for a large proportion of the total calculation time. The option of a self consistent field model is shown in grey.

### 3.3 Self Consistent Field Models for Bound Electrons

The theory given in section 2 requires various quantities such as the oscillator strengths and configuration energies. We have addressed the problem of forming these from the single electron states of an ion; these are found from the atomic potential and the problem of finding this still remains. In order to avoid the need to specify the ion state in detail it is usual to resort to the ‘average atom’ (AA) model to do this, in which a statistical description of the bound electrons is found self consistently with their states and energies. In this section we will derive general results which allow the development of various levels of approximation for the atomic potential.

We begin by considering the Dirac Hamiltonian, which we reproduce from equation (2.7.1),

$$\begin{aligned}\hat{H} &= \sum_i \left[ -\frac{\hbar}{2m} \nabla_i^2 - \frac{Ze^2}{4\pi\xi_0} \frac{1}{r_i} + \xi_i(r_i)(\mathbf{L}_i \cdot \mathbf{S}_i) \right] + \sum_{i>j} \frac{e^2}{4\pi\xi_0} \frac{1}{r_{ij}}, \\ &= \sum_i \hat{h}_i + \sum_{i>j} \frac{1}{4\pi\xi_0} \frac{e^2}{r_{ij}}.\end{aligned}$$

A convenient method of determining the details of the electron states is the variational method, in which the relevant thermodynamic potential is minimised in order to find relationships between the wavefunctions and thermodynamic quantities. To that end we consider a statistical ensemble of all states of the ion and find the equilibrium conditions for state energies, wavefunctions and occupations. We then aim to determine the requirements for equilibrium, which will give the most likely ion state in the plasma. The relevant ensemble is the grand canonical ensemble and its corresponding thermodynamic potential

$$\Omega = E - TS - \mu N ,$$

which we average over all states of the ion to obtain

$$\begin{aligned}\langle \hat{\Omega} \rangle &= \sum_n p_n \langle \hat{\Omega}_n \rangle \\ &= \sum_n p_n \langle \Psi_n | \hat{H} + k_B T \ln \hat{W} - \mu \hat{N} | \Psi_n \rangle ,\end{aligned}$$



where  $\hat{W}$  is the statistical weight operator,  $\hat{N}$  is the number operator and  $|\Psi_n\rangle$ ,  $p_n$  are the wavefunction and probability of the  $n^{\text{th}}$  ion state. As before we use determinantal wavefunctions in which case the matrix elements are [76]

$$\begin{aligned} \langle \Psi_n | \hat{H} + k_B T \ln \hat{W} - \mu \hat{N} | \Psi_n \rangle &= \sum_{\nu} n_{\nu} \int \psi_{\nu}^*(q) \hat{h}_{\nu} \psi_{\nu}(q) dq \\ &+ \frac{1}{2} \sum_{\nu, \lambda} n_{\nu} n_{\lambda} \frac{e^2}{4\pi\xi_0} \iint \frac{|\psi_{\nu}(q)|^2 |\psi_{\lambda}(q')|^2}{|\mathbf{r} - \mathbf{r}'|} dq dq' \\ &- \frac{1}{2} \sum_{\nu, \lambda} n_{\nu} n_{\lambda} \frac{e^2}{4\pi\xi_0} \iint \frac{\psi_{\nu}^*(q) \psi_{\nu}(q') \psi_{\lambda}^*(q') \psi_{\lambda}(q)}{|\mathbf{r} - \mathbf{r}'|} dq dq' \\ &+ k_B T \sum_{\nu} [n_{\nu} \ln n_{\nu} + (1 - n_{\nu}) \ln (1 - n_{\nu})] - \mu \sum_{\nu} n_{\nu} . \end{aligned} \quad (3.3.1)$$

The above expression is the defining relation for the Hartree-Fock (HF) model [76], and is commonly used in the calculation of atomic structure for spectroscopic purposes. In opacity calculations, however, it proves too unwieldy due to the third term on the right hand side. This term is a cross term that arises from the matrix element of the coulomb operator for determinantal wavefunctions; it is a direct consequence of the antisymmetry of many electron wavefunctions. It should not be neglected, however its inclusion significantly increases calculation time. In the Hartree-Fock-Slater (HFS) model this term is included in an approximate manner which is convenient for calculations. The exchange energy is approximated as a functional of the electron density [76] (the parameterisation of which will be considered later)

$$E_{ex} = -\frac{1}{2} \sum_{\nu, \lambda} n_{\nu} n_{\lambda} \frac{e^2}{4\pi\epsilon_0} \iint \frac{\psi_{\nu}^*(q) \psi_{\nu}(q') \psi_{\lambda}^*(q') \psi_{\lambda}(q)}{|\mathbf{r} - \mathbf{r}'|} dq dq' \approx - \int \varphi[\rho(\mathbf{r}), T] d\mathbf{r} , \quad (3.3.2)$$

which since the exchange energy is assumed to depend only on the local value of the electron density alone is known as the local density approximation (LDA).

Given its fairly simple approach, the LDA gives remarkably good results. There are, however, some problems. The use of the LDA means that the potential due to the nucleus and all electrons (see below) does not have a Coulomb form for large  $r$  and so highly excited valence configurations can be poorly described. For the hot plasmas that we are interested in, this is not significant. A second problem that is more important

for our purposes has been pointed out by Wilson *et al.* [77], who noticed that the energy of absorption lines originating from core shells are poorly described by LDA models. They determine that this inaccuracy is particularly severe for transitions out of the  $2s$  shell, and that it is insensitive to the particular form of  $\varphi[\rho(\mathbf{r}), T]$ . After extensive investigation of the alternative options Wilson *et al.* conclude that a different approach to the entire atomic calculation is required; in this work we will continue using the LDA in the knowledge that core-shell excitations may be poorly described.

Before we proceed to find the equilibrium state of the average atom, we consider the volume of work that is required in calculating the thermodynamic potential. In its current form the potential requires summations over all states of electrons in the ion field; this includes both bound and free states. Free electrons are characterised by a continuum of allowed energies and so they constitute a very large number of states to be included in the summations in equation (3.3.1). This poses a large computational problem and so we aim to reduce the workload by invoking the semiclassical approximation for electron states with energy larger than some cutoff  $E_0$ . In this way the summations in equation (3.3.1) are split into two contributions, the full quantum mechanical expressions already stated for electrons of energy  $E < E_0$ , and integrals over the phase space distribution of electrons with  $E > E_0$ ,  $n(q, \mathbf{p})$ . The charge density, for example, then becomes

$$\rho(q) = \sum_{\nu} n_{\nu} |\psi_{\nu}(q)|^2 + \int_{p_0}^{\infty} n(q, \mathbf{p}) \frac{d\mathbf{p}}{(2\pi)^3} , \quad (3.3.3)$$

where the summation runs over all states with  $E < E_0$ . Following this approximation we aim to determine not only the probabilities and wavefunctions of the discrete quantum states, but also the distribution of semiclassical electrons  $n(q, \mathbf{p})$ .

The equilibrium state is found by minimising the grand thermodynamic potential, under the constraint that the wavefunctions  $\psi_{\nu}(q)$  are normalised. The minimum condition reads

$$\delta\Omega(\epsilon_0) + \delta \sum_{\nu} \Lambda_{\nu} \int |\psi_{\nu}(q)|^2 dq = 0 ,$$

where we use  $q$  to denote the spatial and spin co-ordinates of the electron state, and the Lagrange multiplier

$\Lambda_\nu$  ensures the normalisation of wavefunctions. These are related to the energies of the states in the below analysis. The solution to the above equation is a Dirac equation for the single particle orbitals

$$\left[ -\frac{\hbar}{2m} \nabla^2 + \xi_i(r_i)(\mathbf{L} \cdot \mathbf{S}) + V(\mathbf{r}) \right] \psi_\nu = E_\nu \psi_\nu ,$$

where the potential includes the nuclear, electron-electron and exchange potentials. The average occupation numbers of bound states are

$$n_\nu = \frac{1}{1 + e^{\frac{E_\nu - \mu}{k_B T}}} , \quad (3.3.4)$$

and for the semiclassical electrons the equilibrium distribution function has a similar form

$$n(q, \mathbf{p}) = \frac{1}{1 + e^{\frac{E - \mu}{k_B T}}} \quad E = \frac{p^2}{2m} - V(\mathbf{r}) . \quad (3.3.5)$$

The above results are the Hartree-Fock (HF) equations, and can be solved in various approximations. In detailed calculations the statistical treatment of bound state occupation numbers can be neglected and the various  $n_\nu$  can be set to 1 or 0 in order to form a specific configuration. This is the situation discussed previously, in which a solution of the HF equations is required for every configuration in an opacity calculation. The statistical approach has now provided a way past this problem, by allowing the average atom to be described through the energy of each orbital and Fermi-Dirac statistics. In this approximation a single solution of the HF equations is required to describe all configurations in a plasma, and while the electron orbital energies and wavefunctions will be approximate they will be sufficient provided the range of configurations required is not too large. We will investigate this issue in section 6.

The actual solution of the HF equations in their current form is complicated by two features; the first is the fact that in order to find the potential, the wavefunctions must be known, and vice versa. This can be solved numerically using standard ‘self-consistency’ methods to any desired accuracy. The second is the form of the potential, which in the above will be non-central. The effects of the non-central component of the potential, arising from the electron-electron interaction, have been discussed; the most effective method

is to assume a central potential and to include the effects of other terms as a perturbation. In this case the potential becomes

$$V(r) = \frac{1}{4\pi\xi_0} \frac{Ze^2}{r} - \frac{e^2}{\xi_0} \left[ \frac{1}{r} \int_0^r r'^2 \rho(r') dr' + \int_r^{r_0} r' \rho(r') dr' \right] + V_{ex}(r) , \quad (3.3.6)$$

and the electron wavefunctions have the form (2.6.16), with the radial parts described by the pair of differential equations

$$\begin{aligned} \frac{d}{dr} P + \frac{\kappa}{r} P + \left( 2c + \frac{V(r) - E}{c} \right) Q &= 0 , \\ \frac{d}{dr} Q - \frac{\kappa}{r} Q - \frac{V(r) - E}{c} P &= 0 . \end{aligned} \quad (3.3.7)$$

The term in square brackets in equation (3.3.6) represents the potential due to a spherically symmetric charge distribution  $\rho(r)$ ; it is obtained by neglecting all non-central terms in the multipole expansion of the electron-electron interaction and spherically averaging the charge density. It is also identical with the solution of the Poisson equation for the averaged charge distribution. The radial equations (3.3.7) can also be solved relatively easily, and since the wavefunctions now have the correct form the analytic results given in section 2.7 can be used.

The choice of the boundary between quantum and semiclassical electrons ( $E_0$ ) is important to the accuracy of the model, and in fact in certain limits the equations set out above reduce to other more simple models. The IMP code as originally described by Rose [1] uses the Thomas-Fermi model in which all electrons are treated semiclassically ( $E_0 \rightarrow -\infty$ ) and the exchange potential is neglected. This was refined through the inclusion of the exchange potential as parameterised by Rozsnyai [78];

$$V_{ex}(r) = [1 - \lambda^2(r)] \frac{3}{2} \left( \frac{3\rho(r)}{\pi} \right)^{1/3} + \lambda^2(r) \frac{\pi\rho(r)}{k_B T} , \quad (3.3.8)$$

$$\lambda(r) = \max \left\{ 1, \frac{2k_B T}{(3\pi^2 \rho(r))^{2/3}} \right\} . \quad (3.3.9)$$

As a precursor to this work the IMP code has been upgraded to allow the solution of the full HFS model,

using the same exchange functional. The numerics of these changes, along with some examples, are given in chapter 5.

### 3.4 Unresolved Transition Arrays

In previous sections we have discussed the effects of having several electrons bound to a nucleus. We showed that electron-electron interactions result in an energy that depends on the total angular momentum quantum numbers; the various ways that the component angular momenta of electrons can add together mean that for a given electron configuration generated in a DCA calculation there are a set of possible energies. Then a configuration  $\rightarrow$  configuration transition is split into a potentially large number of term lines. DCA calculations cannot resolve this structure, which can lead to large inaccuracies in results [79].

A powerful method of including this extra structure is the ‘unresolved transition array’ (UTA) model, in which the statistical distribution of term lines is used to correct DCA calculations [80]. The main feature of this approximation is that it results in a smooth lineshape that does not show any features that can be associated with individual term lines. In many applications this is sufficient to describe the absorption spectra; in fact the original motivation for the development of the UTA model was the experimental observation of such broad features.

In current IMP calculations the UTA model of Bauche-Arnoult *et al.* is employed to describe the term structure. The effect of term structure is assumed to produce a Gaussian broadening of transition lines, of width equal to the variance in the transition energies of a given configuration - configuration transition. In the original work Bauche-Arnoult *et al.* derived these quantities from first principles, in terms of Slater integrals and angular coefficients. The final expressions require relatively large calculations for every transition line and so it is advantageous to use simpler models. In IMP calculations, therefore, the variance of term lines is approximated as the sum of the variances of the energies of the upper and lower configurations. These are calculated using formulae derived by Moszkowski [81], and are found easily. The assumption that the variances add is based on the assumption that there is no correlation between the positions of the initial and final states in their parent configurations. In fact there is an approximate ordering of states according to their total angular momentum which combined with the selection rule on  $\Delta J$  means that this is not the

---

case. This is discussed in more detail in section 7.1.3.

The Gaussian UTA model described above has been used for many years and is particularly successful in the description of experimentally produced plasmas. The success is based largely on the increased broadening in such systems that is introduced by instrumentation, which smooths the absorption profile into the unresolved structures produced by UTA models. This extra broadening is not present in radiation transport problems and so term structure can play an important role in these applications. The Gaussian UTA model has seen continuous development since the original formulation, where improvements have focused on the inclusion of higher order moments in improved functional forms [82], the inclusion of correlations between term line energy and strength [83, 84], and statistical models [83, 85] (see section 5.3). These improvements are discussed and tested in the following chapters of this report.

## 4 Opacity Experiments

Laboratory measurements of the LTE opacity of plasmas is a far newer field than opacity calculations, and although experimental approaches are continually improving the difficulty of reaching the required conditions and making accurate measurements means that simulations still rely on theoretical models for the opacity. The wide range of conditions that occur during the evolution of a plasma target means that it is likely that simulations will always rely heavily on calculated opacities, and so there is substantial interest in developing experimental techniques to test opacity models. In this section we give a brief discussion of the experimental techniques that have been developed to measure the opacity of plasma; in particular we concentrate on plasmas in LTE.

### 4.1 History

The early tests of opacity calculations, observations of solar structure, have already been described in section 3.1; little could be said about the results of calculations besides the fact that they appeared to be wrong. This problem stemmed from the fact that the opacity was an input to very complex solar models that incorporated many assumptions. Direct measurements of plasma opacity were made possible by the invention of the laser [86], however it would take several decades before that technology could provide the required power to probe the radiative region of a star.

Experimental opacity research was initially motivated by the wealth of information that could be gained by using emission and absorption spectroscopy as a diagnostic. Early work in diagnosing imploding ICF targets demonstrated the power of such methods to measure important parameters of the implosion [87, 88]; these investigations relied heavily on atomic models and detailed analysis of experimental spectra. It was quickly realised that as well as a diagnostic, opacity experiments could be used to probe very interesting physics; the important experiment of Davidson *et al.* [89] showed that plasmas could be produced that allowed the tests of calculations in physically interesting regimes and shortly afterwards Da Silva *et al.* [90] showed experimentally that  $\Delta n = 0$  transitions are essential in describing the opacity close to the onset of convection in the sun. At the same time laser produced plasmas were allowing the investigation of non-LTE

plasmas [91].

In the early late 1990s experimental investigations were beginning to focus on the difficult problem of mid to high- $Z$  plasmas, and methods were devised to reach higher plasma temperatures and densities. These experiments were often specifically designed to test codes, and in particular the various methods of approaching the atomic physics that had been proposed by this time. This motivation has continued, and experimental techniques are still under development to extend the regimes in which opacity calculations can be tested.

## 4.2 Requirements for Plasma Opacity Measurements

As discussed it is not currently possible to measure the opacity of a plasma for a sufficiently wide range of conditions to allow the calculation of plasma dynamics without using first-principles opacity calculations. It is therefore the aim of experiments to provide data that can be used to reliably test models. The constraints that this aim places on experimental designs were developed soon after opacity experiments became feasible [92]; in this section we will give a brief discussion.

A typical experiment will consist of a sample of material that must be heated and possibly compressed to the desired conditions. Since we are interested in LTE the target must be able to maintain its density rather than blow apart. The opacity is then measured from the frequency resolved emission or transmission as described in section 2.4, using a spectrometer. We are interested in the extreme UV (EUV) and X-ray regions and in these cases crystal spectrometers must be used. The integral over the line of sight in equation (2.4.2) can then be unfolded to find the opacity provided that knowledge of the variation in density and temperature over the line of sight is known; in practice reliable results can only be achieved by making efforts to ensure that the plasma is uniform. These conditions requires an experimental design where the sample is constrained in some way and is heated as uniformly as possible. Given the power deposition required the heating is best achieved using a radiation field and in the following section we show that the nature of the plasma system means that a soft X-ray field is desirable.

Since the opacity itself is a sensitive function of temperature and density it is essential to characterise both of these properties of the test plasma. In early experiments hydrodynamic simulations were used to predict



the evolution of the target given knowledge of the heating radiation, however this approach cannot predict the conditions in the target with sufficient accuracy to benchmark opacity codes. More recent experiments all measure the temperature and density of the plasma directly. The temperature cannot, however, be reliably determined spectroscopically from the opacity sample itself since this depends on the opacity model being tested. A popular solution to this problem is to dope samples with a small concentration of a well known element and to measure the temperature of that spectroscopically. Provided that the two elements are well mixed and that equilibrium is achieved this then gives the temperature of the opacity sample. The density can be measured in a similar way or by radiographing the sample at the time of the opacity measurement.

The large power deposition involved in plasma experiments means that targets evolve rapidly in time and so to ensure uniformity it is necessary to sample only a small portion of time over which the changes in density and temperature are small. This can be achieved using gated detectors, or by employing a fast backlighter that only illuminates the target for a short time. The opacity can then be measured for different plasma conditions using the same experimental setup by changing the time at which the probe field is switched on. Hydrodynamic simulations are an extremely useful tool in designing targets and determining the timing of probe beams.

### 4.3 Radiative Heating of Plasmas

The power that can be delivered to a target using a strong radiation field far exceeds that of any other approach; in the following section we will discuss the common methods of generating these strong radiation fields. We begin, however, by analysing the interaction of an electromagnetic (EM) wave with a plasma in order to determine the ideal characteristics to give volumetric heating of the sample. An accurate description of the plasma + EM wave system requires a consistent treatment of the plasma constituents and of the electrostatic fields they generate. We aim to characterise the long range, collective behaviour of the plasma and to do this we use the two fluid model as described by Kruer [93].

The formation of this model is similar to the analysis of the radiative transfer equation given in sections 2.2 and 2.3. The rate of change of the phase space distribution  $f_j(\mathbf{x}, \mathbf{v}, t)$ , which in this case describes the

distribution of the  $j^{\text{th}}$  species in space, velocity and time, is evaluated resulting in the Vlasov equation

$$\frac{\partial f_j}{\partial t} + \mathbf{v} \cdot \nabla f_j = -\frac{q_j}{m_j} \left( \mathbf{E} + \frac{1}{c} \mathbf{v} \times \mathbf{B} \right) \cdot \frac{\partial f_j}{\partial \mathbf{v}} + \left( \frac{\partial f_j}{\partial t} \right)_{\text{coll.}} . \quad (4.3.1)$$

The right hand side of this equation is the familiar convective derivative; the first term on the left hand side describes the acceleration of particles by EM fields, and the second describes the change in the distribution function due to collisions with all species. Changes due to ionisation and recombination are neglected in this model. The Vlasov equations for different species are coupled together through the electric and magnetic fields and by the collision terms. The plasma system is usually described using two Vlasov equations, for the electrons and ions respectively, plus Maxwell's equations for the electric and magnetic fields.

As with the kinetic description of photons, usefull results are obtained by taking moments of the Vlasov equation. The first two moments give the continuity and force equations respectively,

$$\frac{\partial n_j}{\partial t} + \nabla \cdot (n_j \mathbf{u}_j) = 0 , \quad (4.3.2)$$

$$n_j \left( \frac{\partial \mathbf{u}_j}{\partial t} + (\mathbf{u}_j \cdot \nabla) \mathbf{u}_j \right) = \frac{n_j q_j}{m_j} \left( \mathbf{E} + \frac{1}{c} \mathbf{u}_j \times \mathbf{B} \right) - \frac{1}{m_j} \nabla p_j - \sum_{k \neq j} \left( \frac{\partial}{\partial t} n_j \mathbf{u}_j \right)_k , \quad (4.3.3)$$

where we have introduced the mean density and velocity, isotropic pressure and rate of transfer of momentum with the  $k^{\text{th}}$  species as  $n_j$ ,  $\mathbf{u}_j$ ,  $p_j$  and  $(\partial/\partial t)(n_j \mathbf{u}_j)_k$ . This system can then be closed with the assumption of an equation of state for the  $j^{\text{th}}$  species.

These equations can be solved analytically in various regimes to give very useful results. By considering high or low frequency oscillations in the particle positions, velocities, pressures and the electric field the plasma can be shown to support two modes of oscillation; high frequency oscillations in the electron density which propegate according to the dispersion relation

$$\omega^2 = \omega_{pe}^2 + 3k^2 v_e^2 , \quad (4.3.4)$$

where  $v_e$  is the electron thermal velocity and  $\omega_{pe}$  is the electron plasma frequency given by

$$\omega_{pe} = \sqrt{\frac{e^2 n_0}{\varepsilon_0 m_e}} . \quad (4.3.5)$$

Note that in the above collisions have been neglected; in reality the oscillatory motion of the electrons in the plasma wave is randomised through collisions with ions, leading to damping of the wave and heating of the plasma. Similar analysis of low frequency oscillations in the ion density yield the ion acoustic plasma modes with dispersion relation

$$\omega = \pm k v_s , \quad (4.3.6)$$

where the ion sound speed is

$$v_s = \sqrt{\frac{Z k_B T_e + 3 k_B T_i}{m_i}} . \quad (4.3.7)$$

The plasma can support a range of frequencies of oscillations, however from the point of view of the collective absorption of radiation it is the electrons that are most important due to their low inertia. Oscillatory electron modes do not exist for  $\omega < \omega_{pe}$  since electrons are able to move and damp out the field in this case. We then expect that a driven EM wave will only be able to propagate if it has a frequency greater than the plasma frequency.

The dispersion relation for an applied field of frequency  $\omega_r$  is found by using the force equation to derive the current in the plasma and substituting into Maxwell's equations [93]. When collisions are included the real and imaginary parts of the wavevector of the electric field are

$$k_r = \frac{1}{c} \sqrt{\omega_r^2 - \omega_{pe}^2} , \quad (4.3.8)$$

$$k_i = \frac{1}{2} \frac{\omega_{pe}^2}{\omega_r^2} \frac{\nu_{ei}}{v_g} , \quad (4.3.9)$$

where  $\nu_{ei}$  is the frequency at which electron-ion collisions take place assuming that the ions do not move, and  $v_g \equiv \partial \omega_r / \partial k$  is the group velocity of the wave. As expected, for  $\omega_r > \omega_{pe}$ , the wave is able to propagate with some attenuation due to collisions; for  $\omega_r < \omega_{pe}$  the plasma cannot support the wave and it is reflected.

Depending on the frequency of the applied field and the density of the target, then, this simple picture predicts that the radiation will be either reflected or transmitted; when it is transmitted it will transfer its energy to the plasma electrons and heat them. In practice an intense field will heat an overdense target on its front edge since the field still penetrates; this then expands and a density gradient is set up. The field will then propagate through the underdense region where a wealth of processes allow further coupling of EM energy into the plasma.

It has already been mentioned that for the purposes of a plasma opacity experiment, great efforts are made to ensure that gradients in the temperature and density are minimised. Clearly, then, the situation where the target is overdense with respect to the heating radiation is not ideal for this application since large gradients are unavoidable. We therefore desire an underdense target, which can be achieved by using low density targets or high frequency radiation. For most LTE applications we require as large a density as possible and so in many experimental designs the sample is tamped or shocked to get as close to solid density as possible. The nature of the heating radiation must then be chosen to suit these dense targets. Consider an iron target, ionised to  $16^+$  at 10% of solid density. Then the plasma frequency is  $\omega_{pe} \simeq 20$  PHz (equivalent to  $\sim 10$  eV) and a soft X-ray driver must be used.

The X-ray driver will then be absorbed by the opacity sample in several ways. Energy will be passed to electrons through collisional absorption and the generation of plasma waves as well as inverse bremsstrahlung. The energy of the heating photons is also large enough that they can cause ionisation and excitation of plasma ions directly; if the field is strong then this may drive the ion populations out of LTE and so it is important that the density can be maintained so that electron-electron and electron-ion collisions are fast enough to overcome radiative transitions. To that end samples are usually ‘tamped’ - surrounded with layers of low Z material (usually plastic) that will slow down the expansion of the opacity sample. The density can be further increased by driving shocks into the target. Since in most cases LTE opacity experiments strive to reach the largest density possible, both of these approaches are important features of experimental designs.

The driver field can be used to measure the absorption of the plasma and therefore the opacity, however this approach is not ideal; the pulse length of the heating radiation is generally quite long and the sample conditions evolve during that time. These temporal variations have the same effect as spatial gradients

making it difficult to obtain a good opacity measurement. It is easier to use a second, shorter, pulse of radiation to backlight the target to find the opacity during some small portion of the target's evolution. This has the additional advantage that the backlighter field can be weak enough to avoid heating the target. The pump and probe fields must then be chosen to avoid the co-incidence of spectral features that may confuse the analysis of observed spectra.

## 4.4 Typical Plasma Opacity Experiments

The previous two sections have set out the basic requirements for a plasma opacity experiment, and how to achieve them. All that remains is a method of providing the large flux of X-rays to drive and probe the sample. In this section we will describe laser opacity experiments, which are the most common, and experiments using X-rays generated on Z-pinch machines, which have the potential to provide very large fluxes of driver radiation.

### 4.4.1 High Power Laser Experiments

High powered lasers have provided scientists with the ability to provide very large intensities to opacity targets however the majority of systems rely on Nd:YAG amplifier technology which provides intense radiation in the infrared region (typically at  $1064 \text{ nm} = 1.2 \text{ eV}$ ). The intensity is sufficient to allow efficient production of second or third harmonic radiation using nonlinear crystals, decreasing the wavelength to provide radiation in the ultraviolet ( $\sim 6 \text{ eV}$ ). In fact many laser systems are specifically designed to deliver frequency doubled or tripled light due to its favourable absorption. In the previous section it was seen that even for a relatively low density target this is around a factor of 2 too low in photon energy; in order to provide the desired volumetric heating the laser energy must be converted to X-rays.

Early on in the development of laser plasma experiments it was found that a high  $Z$  foil can efficiently convert laser energy into soft X-rays through thermal emission after being heated [94]. This provided the means to generate X-ray fluxes that can heat opacity targets as desired. Modern laser opacity experiments then usually consist of a sample placed close to a high  $Z$  material which is irradiated with laser light. The sample is designed to give the desired plasma conditions and uniformity as described and the heater material

is chosen to provide a well known driver field for the laser parameters. This is often chosen to be gold, in the form of a foil [95, 96, 97, 90, 98, 89] or a cavity surrounding the sample [99, 100, 101, 102, 103]. The same process by which heating radiation is generated can be used to provide a backlighting field, and in this case the laser target material is chosen to give a relatively featureless spectrum in the probed region. Recent experiments have also employed new breakthroughs in X-ray laser technology to provide backlighter radiation [104], and to heat the target [105].

The hydrodynamic isolation of the sample from the drive laser in this scheme prevents laser driven shocks from entering the target, which would cause rapid time variation in plasma conditions. If such a shock were allowed to enter the opacity sample then the plasma would not be uniform over the integration time of the experimental diagnostics, and the unfolding of data would rely on radiation - hydrodynamic simulations. If, however, data can be collected with sufficient time resolution (by using a short pulse backlighting beam or high resolution streak camera) then a drive laser produced shock can be used to probe much higher densities than would otherwise be available [106]. Such an approach allows data to be collected that are very useful in testing the performance of opacity codes at high density; we use an example of this data in the following sections.

#### 4.4.2 Pulsed Power Experiments

One of the defining features of wire-array pulsed power experiment is that the plasma is resistively heated, and that magnetic fields generated by the large driven currents cause the plasma to implode. The hot plasma emits X-rays during the whole of its evolution; a long period of relatively low power radiation during the implosion, followed by a very intense pulse of X-rays when the plasma stagnates on axis. On the largest machines wire arrays are the most powerful source of X-rays currently available; the Z machine at Sandia national laboratory can provide  $> 200$  TW of X-rays in a 6 ns (FWHM) burst [107]. This very powerful, long duration pulse allows the heating of relatively large samples under uniform conditions and so wire-array Z pinches are very interesting for opacity research.

Although the use of a Z pinch drive is very promising, there have been few experiments so far. Proof of principle experiments have demonstrated that the use of the Z machine to measure X ray opacity and

---

emissivity and to study photoionised plasmas is feasible; these experiments are still under development. Recent experiments have, however, measured the opacity of LTE iron under conditions of relevance to the bottom of the convective zone in the sun for the first time [108]. This experiment was similar in approach to the laser opacity experiments discussed previously, using a tamped iron foil that was heated and backlit by the nearby tungsten wire array plasma. The success of this experiment is based on the relative insensitivity of the ion balance to the plasma density, allowing the experiment to closely reproduce the ion balance in the sun at a fraction of the actual density. Such an approach is very useful in testing the relative positions and strengths of absorption lines and the models used by opacity codes; the description of more density-dependant processes (for example line broadening) is more difficult.

## 5 Improvements to the IMP Opacity Code

During this research the IMP code has been continuously upgraded from the form described by Rose [1]. In this section a brief overview of the changes, which take the form of both numerical upgrades and changes to the opacity model, will be given. Changes to the numerical method used in DCA calculations are described first; further upgrades have improved code performance by around a factor of 3. Following this the various changes to the opacity model are described.

### 5.1 Generation of Configurations

It was mentioned in section 3 that a large proportion of an opacity calculation is concerned with the generation of ion configurations and the subsequent calculation of absorption lines and edges. For this reason it is of interest to first approach this problem as efficiently as possible, and second to try to limit the number of configurations that must be included in a given calculation. The method by which ion configurations are generated is then very important, and has been upgraded in order to produce the data used in the following sections of this thesis.

In original IMP calculations ion configurations are generated by placing principle quantum number shells of an ion into one of three categories based on their average populations; ‘core’ shells which are assumed to be fully occupied in all configurations, ‘Rydberg’ shells which are empty in all configurations, and a single ‘valence’ shell which is allowed to have its population varied from empty to full in order to generate a set of ion configurations. The valence shell is that with the largest population variance

$$\frac{\sum_{i \in n} g_i p_i (1 - p_i)}{\sum_{i \in n} g_i},$$

where  $g_i$  and  $p_i$  are the degeneracy and probability of occupation of a given  $n\ell j$  single electron state, and  $\sum_{i \in n}$  denotes summation over all electron states in a given  $n$  shell. In this way calculations are said to ‘open’ a single shell; in IMP calculations the approximation is supported by considering the neglected configurations in the average atom approximation. This scheme is successful in describing plasmas in which the populations



of core and Rydberg shells have a low variance. However situations in which two or more shells are open are frequently encountered. In such cases the single valence shell approach described above will neglect ion configurations that make an important contribution to the plasma opacity.

The obvious solution to this problem is through the extension of the IMP DCA model to allow two or more valence shells when necessary. It is this extension that has been implemented in the version of IMP used in this thesis, however significant computational problems can arise. To show this, consider a plasma in which the average number of bound electrons is close to 28, on the boundary between the  $M$  and  $N$  shells. This example is of relevance to the discussion of Nb data in following sections. In this case neither the  $M$  or  $N$  shells can be considered to be completely empty or full and both should be opened. If this is done, the DCA calculation will include a huge number of configurations (see section 6), requiring CPU months to perform. This is not feasible, and so a modified scheme is required.

In these calculations we open up to three valence shells but consider only configurations that satisfy some user defined constraints. A minimum and maximum population is defined for each of the open shells and these are used to limit the number of configurations in the DCA calculation. These constraints can then be varied to give a good balance between code runtime and the accuracy of the final result. This problem is investigated in section 6.

In the current IMP calculations a recursive subroutine is used to generate ion configurations. This routine calls itself once for each single electron state in the valence shells. Each instance of the routine then controls the number of electrons that occupy its own state and compares the populations of each shell with the defined constraints. In this way configurations which do not meet the desired constraints are not generated; this saves a significant amount of calculation time over calculations in which all configurations are generated and only a subset of these are used in opacity calculations. This scheme is also convenient since it allows easy parallelisation of the DCA routines by sending different instances of the generation routine to different CPUs. This has been exploited using openMP in the present calculations, leading to calculations that scale linearly with the number of cores used to run the code.

This model allows for a much more flexible consideration of ion configurations in IMP opacity calculations. The calculation of the broadening of absorption lines due to the non-zero populations of Rydberg levels, as

found in the original IMP calculations, must also be modified to deal with partially open valence shells. The model used in IMP involves a summation over the high  $n$  Rydberg states [109];

$$\sigma_{if}^2 = \sum_l g_l p_l (1 - p_l) (H_{il} - H_{fl})^2, \quad (5.1.1)$$

where  $H_{ij}$  is the interaction energy between the electrons in states  $i$  and  $j$  as described in section 2.7, and  $l$  runs over all Rydberg states. Each term in the expression represents the variance in the population of a state, in the binomial approximation, multiplied by the change in energy of the jumping electron due to interactions with that state. This expression cannot be evaluated for states within a partially open valence shell since the occupation probabilities of these states are not known. The effect of such states is important, however, since they interact strongly with the initial state of a transition and produce relatively large shifts in transition energy. This problem arises since we no longer consider the full shell configuration as part of the DCA calculation; a solution would be to redefine Rydberg states as those states that are empty when the lowest states of the shell are populated with the maximum number of valence electrons and to continue the DCA calculation in the usual way. Such a definition is unsatisfactory since the valence and Rydberg states would not be separated by an appreciable energy gap, making the average population of the Rydberg states large.

We instead consider the electrons in a valence shell to fall into two classes; DCA electrons, the states of which are treated explicitly, and other statistical electrons that act as spectators to the transitions made by each DCA electron. What we then require is the variance in the number of statistical electrons in each valence state, which is correlated with the configuration of DCA electrons. If we consider a configuration of DCA electrons  $C = \{n_i\}$  and calculate the probability that  $k$  perturbing electrons reside in the  $j^{\text{th}}$  valence state we find

$$P_j(k) = \left[ \prod_{i \neq j} \binom{g_i}{n_i} p_i^{n_i} (1 - p_i)^{n_i} \right] \binom{g_j}{n_j + k} p_j^{n_j + k} (1 - p_j)^{g_j - n_j - k}, \quad (5.1.2)$$

where we have again used binomial statistics. This probability can be used to calculate the variance of the

number of statistical electrons in each valence state, taking into account the presence of the DTA electrons;

$$\sigma_j^2 = \frac{\sum_{k=0}^{g_j-n_j} k^2 P_j(k)}{\sum_{k=0}^{g_j-n_j} P_j(k)} - \left[ \frac{\sum_{k=0}^{g_j-n_j} k P_j(k)}{\sum_{k=0}^{g_j-n_j} P_j(k)} \right]^2, \quad (5.1.3)$$

which can be used in place of the full binomial variance in equation (5.1.1). The use of this expression is complicated by the fact that the variance given above concerns only a portion of the allowed populations of the  $j^{\text{th}}$  state, meaning that it is unlikely that these perturbing states produce a symmetric broadening of absorption lines. In fact, spectator electrons are likely to strongly effect the initial state of a transition and produce an asymmetric modification. It should also be noted that the limits in equations (5.1.3) should be modified to reflect perturbing configurations included in the DCA portion of calculations. The upper limit given in (5.1.3) is appropriate for configurations with the maximum allowed number of electrons; for configurations with fewer electrons the summation should be terminated earlier. In the first approximation we leave the widths of lines with less than the maximum electrons unchanged and for those with the maximum number of electrons we introduce a correction of

$$\sum_{l \in C} \sigma_l^2 (H_{il} - H_{fl})^2. \quad (5.1.4)$$

The effect of this correction can be seen in figure 5.1 which displays the bound - bound opacity of iron at 200 eV and 1 g/cc. In the figure we show the absorption lines that arise from a single configuration  $[\text{Ar}]:3d^2$ . Black lines demonstrate the results from a full DCA calculation, where transitions that differ by spectator electrons in the valence shells are treated explicitly. The red and blue lines show a limited DCA calculation with up to 10 electrons in the M shell, with the correction neglected and included respectively. It can be seen from the figure that the correction does not give a good description of the extra structure in a full calculation. This is due to the relatively large perturbations that these spectator electrons produce, which leads to a splitting of lines rather than a broadening. The asymmetric nature of this splitting leads to a generally overbroadened line.

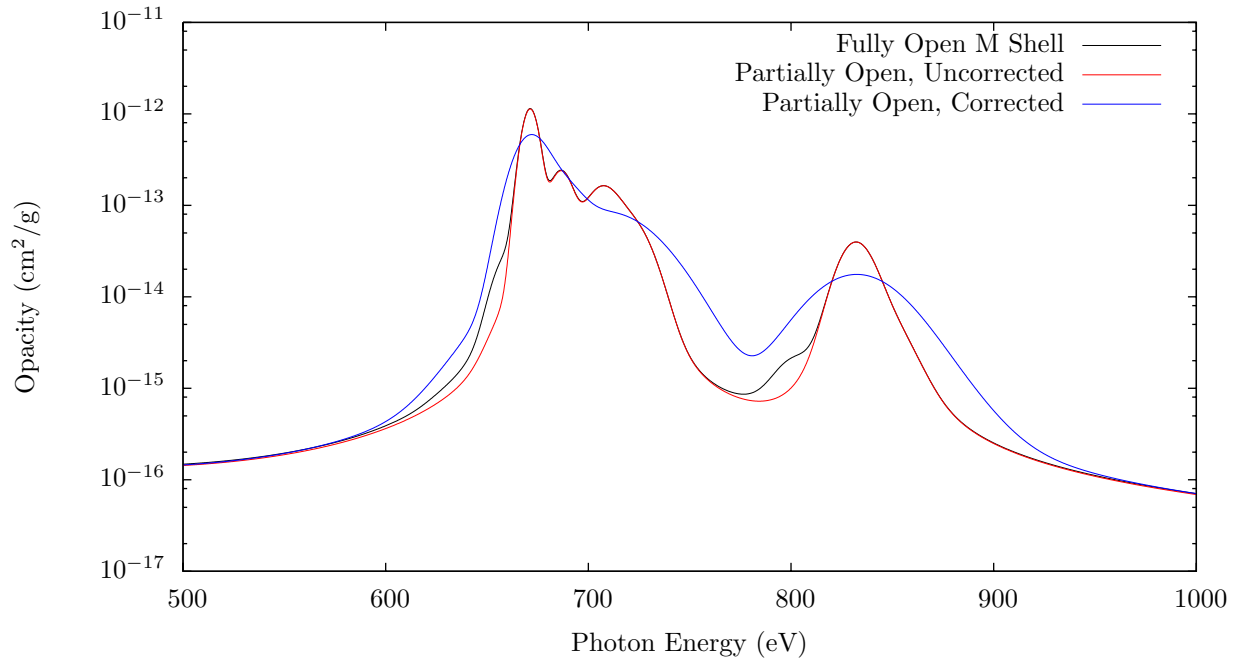


**Figure 5.1:** Absorption lines arising from the  $[Ar]3d^2$  configuration in iron at 200 eV and 1 g/cc. The black line shows the results in which the M shell is fully treated in DCA calculations; red shows the results where the number of electrons is limited to 10, but no correction is made for the partially filled shell; blue shows the same calculation including the correction given in equation (5.1.4)

This situation is improved when the DCA calculation is sufficiently large that perturbing configurations have a small probability. In this situation all lines that are large enough to appear in the spectrum are treated in DCA calculations, and the dielectronic width is negligible. We will see in later sections that ensuring that opacity codes operate in this regime is essential to avoid convergence errors in the final result; in effect opacity codes must operate in a regime where the dielectronic width is unimportant. For this reason the corrected width will not be included in further work.

## 5.2 The Relativistic Hartree-Fock-Slater Self Consistent Field

Previous versions of the IMP code use a Thomas-Fermi model for the atomic potential, which is then used in the solution of the Dirac equation as described in the previous two sections. This model relies on a semiclassical description of all electrons in the system through Fermi-Dirac statistics, and as such cannot reproduce the effects of bound electron structure on the atomic potential. The model has been updated for this work so that the bound electron structure is included self consistently with the potential. In effect the

HFS model described in section 3.3 is now used.

In the Thomas-Fermi model, the atomic potential 3.3.6 reduces to a differential equation that can be solved numerically. Once the solution is found it is used in the solution of the Dirac equation for single electron radial wavefunctions  $P(r)$  and  $Q(r)$ . A more realistic treatment of the atomic potential can be found using the solutions of the Dirac equation to calculate bound electron densities as described previously. Since this new model essentially modifies the charge density to include bound electrons the modifications to IMP routines are relatively minor. The complications arise since there is now an explicit dependence on the radial wavefunctions and so intermediate solutions of the Dirac equation are required; in modified IMP calculations the wavefunctions from this intermediate solution are used to generate a bound charge density for the average atom. This is then compared to the charge density originally used to generate the atomic potential, and a self consistency calculation is performed. To aid convergence we use the scheme described by Nikiforov, Novikov and Uvarov [76] in which the potential used in an iteration is a linear combination

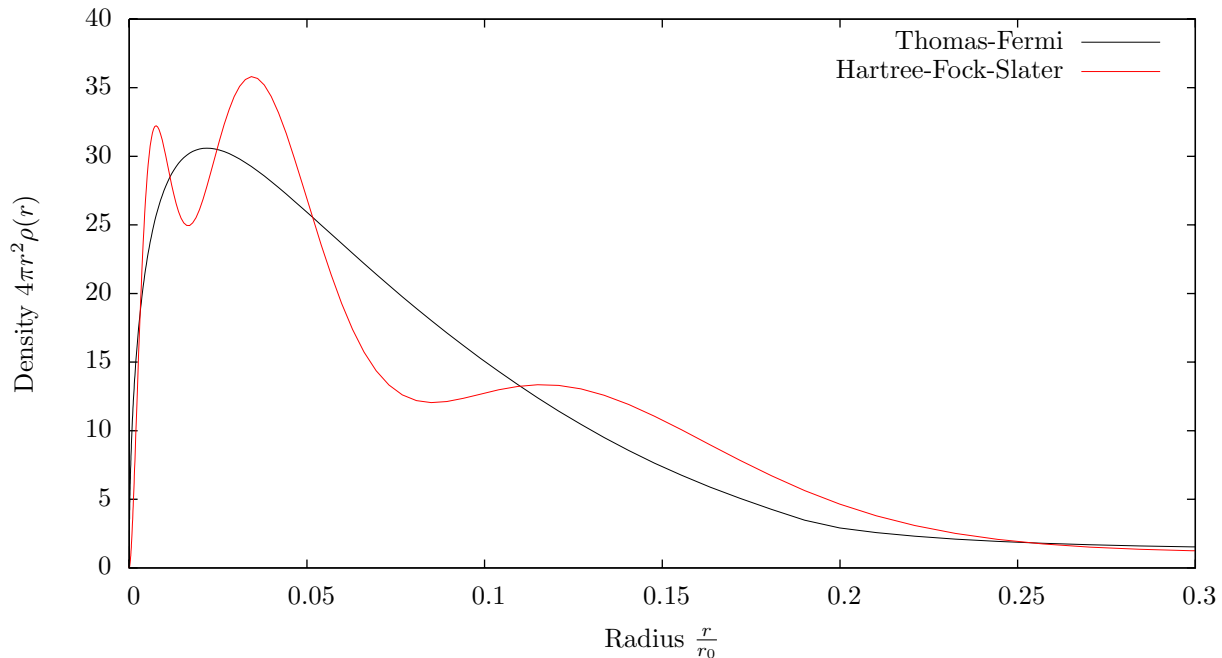


**Figure 5.2:** The radial distribution of charge around the an iron nucleus in a plasma at 50 eV and 1 g/cc. The black line shows the results from a Thomas-Fermi model in which the charge density is not made self consistent with electronic wavefunctions; the red line shows the Hartree model where wavefunctions are used to find electron density. The Hartree model is able to describe structures in the density due to bound electrons which appear as a set of bands. In this example the three bands are the K,L and M shell electrons.

of the input and output potentials of the previous iteration. The damping factor is determined in order to minimise the mismatch between the two stages of a calculation as described in the reference.

An example of the results of this updated model is shown in figure 5.2, in which we plot the charge density as a function of radius around an iron nucleus. The plasma conditions are  $T = 50$  eV and  $\rho = 1$  g/cc, under which the average atom retains electrons in the  $K, L$  and  $M$  shells. These shells can be seen clearly in the HFS model density; the effect of the semiclassical description of bound electrons in the Thomas-Fermi model is also clear where the Thomas-Fermi model does not include oscillations in the bound electron density.

| Electron State | Thomas-Fermi | HFS   |
|----------------|--------------|-------|
| $1s$           | 7.635        | 7.636 |
| $2s$           | 1.050        | 1.050 |
| $2\bar{p}$     | 0.958        | 0.958 |
| $2p$           | 0.944        | 0.944 |
| $3s$           | 0.222        | 0.222 |
| $3\bar{p}$     | 0.182        | 0.183 |
| $3p$           | 0.179        | 0.180 |
| $3\bar{d}$     | 0.113        | 0.114 |
| $3d$           | 0.112        | 0.113 |
| $4s$           | 0.041        | 0.041 |
| $4\bar{p}$     | 0.030        | 0.030 |
| $4p$           | 0.029        | 0.029 |
| $4\bar{d}$     | 0.013        | 0.013 |

**Table 5.1:** *The energies of single electron states in an iron plasma of temperature 50 eV and density 1 g/cc. Although the improved model leads to large changes in the electron charge density (figure 5.2), the effect on energy level structure is negligible.*

From the point of view of opacity calculations, the energy eigenvalues of energy levels and oscillator strengths between them are most important, and these quantities are more sensitive to changes in the atomic potential than the charge distribution. The differences in atomic potential in the TF and HFS models are in fact very small and so it is expected that the nature of the model will make little difference to the results of opacity calculations. The one electron energy level structure as calculated for the same iron plasma as used previously are shown in table 5.1, where it can be seen that the small differences in the potential lead to negligible changes in the energy level structure. Similarly, for the  $3.2 \times 10^4$  transitions that originate from the  $M$  shell of this plasma, the average change in oscillator

strength is  $\sim 0.1\%$ .

The various models available in updated IMP calculations can also be tested against experiment. A good test of the equation of state in these calculations is provided by the experimental data of Hoarty *et al.* [106]. This experiment used thin sample layers of aluminium buried in CH plastic tampers, with a thin layer of

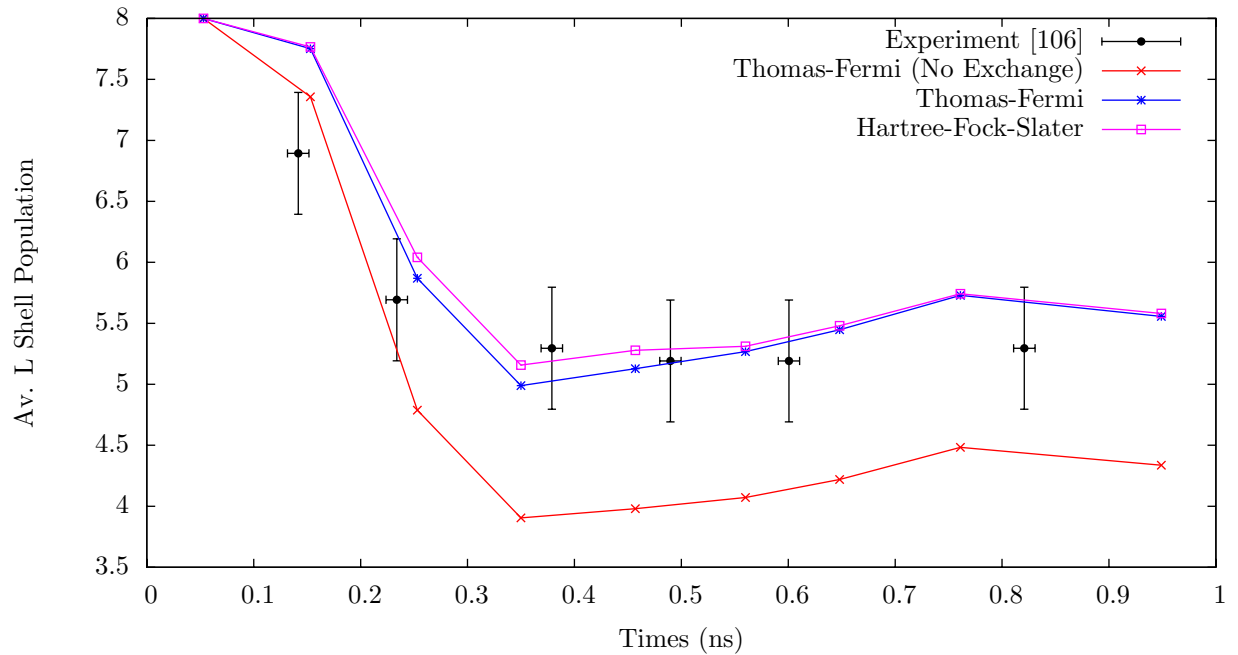


**Figure 5.3:** The average  $L$  shell population of an aluminium plasma during the experiment of Hoarty et al. [106]. Experimental data, error bars and plasma conditions are taken from the reference; calculations are made using the IMP code in various approximations. The exchange potential is essential in describing the experiment correctly; only slight differences are seen between the TF and HFS models.

gold on one outer surface. When irradiated by the HELEN laser this surface converts laser energy into X rays which uniformly heat the Al target. A shock is driven by the laser through the gold and into the target, which combined with the plastic tampers keeps the density close to solid.

The experiment employed several diagnostics that make it very useful for our code testing. Time resolved transmission data were collected for the purpose of investigating the effect of electron impact broadening; these will prove useful in section 5.4. Alongside these, measurements of the ablation pressure allowed the time dependant temperature and density of the sample to be determined. We model the average population of the  $L$  shell, measured spectroscopically by Hoarty *et al.*, using the IMP code in various approximations.

We use the temperature and density profiles from the original reference as an input for IMP, and plot the  $L$  shell population from the average atom calculation in figure 5.3. We plot calculations using the TF model, TF model with exchange included, and the HFS model. Also shown are the experimental data along with their error bars (with thanks to Dr. Dave Hoarty). It can be seen that the neglect of exchange effects gives an unreliable result; when this is included in either the TF or HFS models a very good description of

the experimental data is found. This serves to validate the use of the exchange potential (3.3.8), however it should be noted that Hoarty *et al.* use a detailed atomic model to infer the conditions used in our calculations and so conclusions regarding the details of the exchange potential in IMP are dependant on these calculations. Finally, the two calculations which include exchange give essentially the same results; this is unsurprising since level populations diagnose the accuracy of energy eigenvalues and the results in table 5.1 have shown that little difference is seen between the two models in that respect. The points where a slight discrepancy is seen are the points where the shock reaches the sample and the temperature and density are largest.

The experimental data given in figure 5.3 are very useful in testing the HFS model since they diagnose the populations of states that lie far from the continuum; IMP calculations show that states up to  $3\bar{d}$  remain bound. These states will be only weakly effected by perturbations from the surrounding plasma and so the model used for continuum lowering should not change the results. We now turn to a second set of experimental data, those of Gregori *et al.* [110], which allow us to test this aspect of the IMP code.

In this experiment carbon foam cylinders were coated with Rb and illuminated with 35 beams of the OMEGA laser.  $K$  shell emission from the Rb then heated the carbon while the symmetry of the drive maintained the density at 0.72 g/cc. The sample was probed by a Ti plasma close by; X-ray backscatter measurements then allowed the plasma ionisation  $Z^*$  to be measured. The production of the Ti plasma was delayed with respect to the main drive to allow measurements at different plasma temperatures to be made. Since these measurements depend on the population of all electron states the experimental data are more sensitive to the position of the continuum than in the experiment of Hoarty *et al.* We show the experimental data along with the same atomic models as before in figure 5.4.

In this case, as before, there is no difference between the different models used in IMP provided that the exchange potential is included. None of the models give an accurate description of all three experimental points, with all models underestimating the ionisation at the higher temperature. This suggests that the calculations have electron orbitals that are bound when in fact they have been removed into the continuum; the continuum is therefore too high in energy and the absorption edges can be expected to be shifted to high energy. We will see more possible evidence of this in the analysis of the transmission through a niobium



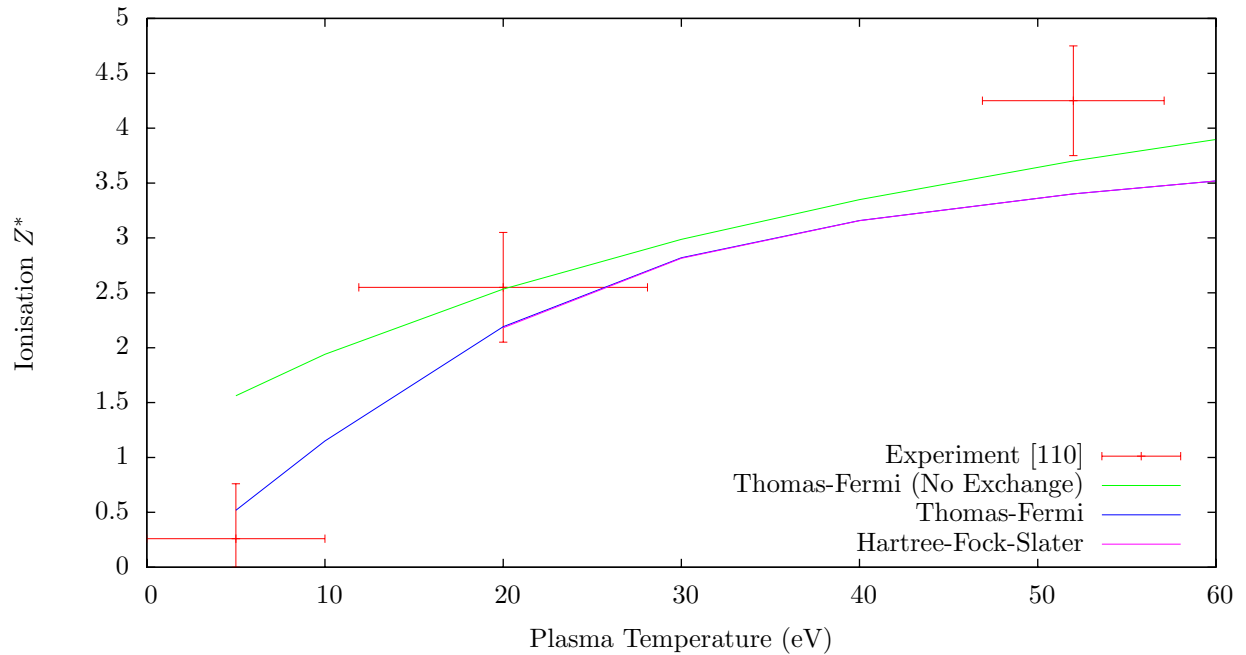


**Figure 5.4:** Comparison of the experimental data of Gregori et al. [110] for the mean ionisation of carbon at  $\rho = 0.72$  g/cc as a function of temperature with various IMP calculations. As before there is little difference between the TF and HFS models provided the exchange potential is included. All models underestimate the ionisation at high temperature suggesting that there may be a problem with the description of continuum lowering in IMP.

sample in section 6.

It has been described in previous sections that another downfall of the atomic models used in IMP is the use of the average atom approximation for level occupation numbers. The next stage of approximation, in which an atomic model is solved for the specific configuration of interest, is not feasible in our calculations as it clearly will require an atomic model to be solved for every configuration in our calculations.

### 5.3 Random Transition Arrays

The unresolved transition array model described in the previous section is an important approximation, the investigation of which forms a significant portion of the work in the following chapters of this thesis. It is essential in allowing simple models such as the DCA model of IMP to describe atoms with many electrons, which in turn is the situation where fast models are of greatest interest. The implicit assumption of a line density that is large enough to prevent the formation of absorption windows within the line is not generally true, particularly in the description of radiation transport where only plasma broadening processes can cause

term lines to merge.

A good compromise between the UTA model and full term-resolved atomic physics calculations is the random transition array (RTA) model, originally proposed by Duffy [83]. In this model we assume a statistical description of term lines in energy and strength (see section 7) and take a set of random samples to represent the components of a UTA. These are then added to the absorption spectrum individually. In this way, if the individual line broadening is too small to result in an unresolved lineshape, the RTA will produce a diffuse absorption line as required without expensive configuration-resolved atomic physics. The random positioning of the component ‘term lines’ is assumed to be unimportant since it is the presence of absorption windows that determines the Rosseland mean opacity.

Given a distribution of term lines, the generation of a set of samples is straightforward using standard Monte-Carlo methods [111]. In the case of a normal distribution of lines, the cumulative distribution function can be analytically evaluated making this quite efficient. In the case of the more complex distributions we will consider in later sections, the computationally more expensive ‘rejection method’ is used in IMP calculations. The only other information that is required is the number of samples to take.

In this calculation we use work due to Zirnbauer and Brink [112] to find the moments of the distribution of  $M_J$  values that arise from a configuration; this can then be used to find the number of lines using work due to Bauche & Bauche-Arnoult [113] and more recently Gilleron and Pain [114]. The main development here is the re-formulation of the combinatoric expressions for the moments of the  $M_J$  distribution in a form that is convenient for the recursive DCA routines of IMP. The results of Zirnbauer and Brink’s work, the degeneracy, variance and kurtosis of the  $M_J$  values of a configuration  $C = \{n_i\}; i = 1 \dots w$ , are given respectively by Gilleron and Pain as

$$g_C = \prod_i^w \binom{2j_i + 1}{n_i} ,$$

$$\sigma_C^2 = \sum_{i=1}^w q_i \nu_i ,$$

$$\kappa_C = 3 - \frac{1}{\sigma^4} \sum_i^w q_i (a_i + b_i q_i) ,$$

where

$$\begin{aligned} q_i &= \frac{n_i(2j_i + 1 - n_i)}{2j_i} , & \nu_i &= \frac{1}{3}j_i(j_i + 1) , \\ a_i &= \frac{1}{15}j_i(2j_i + 1)(j_i + 1)^2 , & b_i &= -\frac{1}{15}j_i^2(j_i + 1) , \end{aligned}$$

and these values are required for both the upper and lower configurations. If we consider the one electron transition  $i \rightarrow j$  and denote the final configuration  $C'$ , the above expressions can be rearranged to give

$$g_{C'} = g_C \times \frac{n_i}{(g_i - n_i + 1)} \frac{(g_j - n_j)}{n_j + 1} , \quad (5.3.1)$$

$$\sigma_{C'}^2 = \sigma_C^2 - \frac{1}{3}(j_i - n_i + 1)(j_i + 1) + \frac{1}{3}(j_j - n_j)(j_j + 1) , \quad (5.3.2)$$

and

$$\begin{aligned} \kappa_{C'} &= 3 - \frac{\sigma_C^4}{\sigma_{C'}^4} (3 - \kappa_C) \\ &\quad + \frac{1}{\sigma_{C'}^4} \frac{j_i - n_i + 1}{j_i} \left( a_i + 2q_i b_i - b_i \frac{j_i - n_i + 1}{j_i} \right) \\ &\quad - \frac{1}{\sigma_{C'}^4} \frac{j_j + n_j}{j_j} \left( a_j + 2q_j b_j + b_j \frac{j_j - n_j}{j_j} \right) . \end{aligned} \quad (5.3.3)$$

In the above results each subsequent term contains information regarding different stages of a DCA calculation; generation of the configuration, selection of initial state, and selection of final state each introduce independent correction factors. This simplicity is made even more clear by noting that the coefficients  $a_i$ ,  $b_i$  and  $\nu_i$  depend only on the details of the  $i^{\text{th}}$  single electron orbit, not its population, and so must be calculated only once. The number of configurations is very small compared to the number of absorption lines and so the fact that the majority of the computational work can be done at a configuration - resolved level is a useful result.

In IMP calculations the calculation of the above moments is split up to give the most efficient calculation possible. Once known the moments for a given initial and final configuration are combined to give the total number of electric dipole transitions between the two configurations using the work of Bauche & Bauche-

Arnoult [113]. This then determines the number of samples to take from the desired distribution function to form the RTA lineshape;

$$N = \frac{3g_1g_2}{8\sqrt{\pi}\sigma^3} \left[ \left(1 - \frac{1}{2\sigma^2}\right) + (\kappa - 3) \left(\frac{5}{16} - \frac{25}{96\sigma^2}\right) \right] , \quad (5.3.4)$$

$$\sigma^2 = \frac{\sigma_1^2 + \sigma_2^2}{2} , \quad (5.3.5)$$

$$\kappa = \frac{\kappa_1 + \kappa_2}{2} . \quad (5.3.6)$$

It should be noted that the more recent work of Gilleron and Pain suggest that the above work, which is based on a Gram-Charlier expansion of the distribution of  $M_J$  values, can be improved by using a generalised Gaussian expansion. In the work presented here we use the Gram-Charlier since it requires less computational resources (the generalised Gaussian approach requires the evaluation of several  $\Gamma$  functions), and investigation has suggested that the two approaches agree to within  $< 3\%$ . In our IMP calculations we re-normalise each RTA to ensure that the correction linestrength has been added and so small errors in the number of component lines are not considered to be important. Finally, combining the expressions derived previously, equations (5.3.1)-(5.3.3), with the equations for the number of term lines (5.3.4)-(5.3.6) results in a relatively simple model that has been implemented in IMP.

The effect of the RTA model on the opacity can be seen in figure 5.5. Here we return to the example used in previous sections, namely iron at 200 eV and 1 g/cc, and calculate the radiative opacity in the UTA and RTA approximations. In this example the number of absorption lines is increased from  $1.1 \times 10^6$  to  $45 \times 10^6$ , and the profile is much more diffuse; the result is that the Rosseland mean opacity is lowered by  $\sim 1\%$ . In cases where absorption lines are more important this effect can be expected to be more pronounced. In the calculations we include dielectronic and Doppler broadening on each component term line; since the two opacity profiles are not the same this demonstrates that transition arrays are resolved and so the RTA model gives the best approximation to full DTA opacity calculations. If the calculations shown in figure 5.5 include other mechanisms such as the effect of interactions with the plasma (see the following section) or the effect of a spectrometer, then we may recover the UTA model. In fact in many experimental applications the instrument width can dominate and so the UTA model is often sufficient for modelling; in problems of

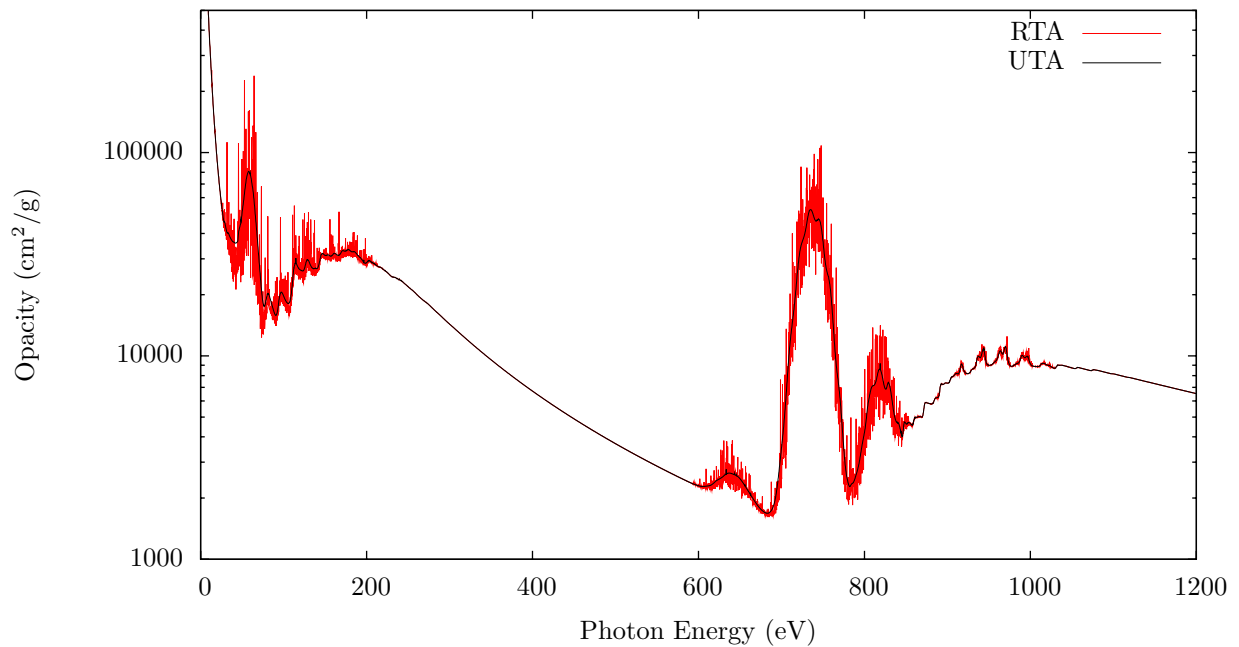


**Figure 5.5:** *The opacity of iron at 200 eV and 1 g/cc calculated using the random transition array (RTA) and unresolved transition array (UTA) models. The extra complexity that can be added using the RTA is clear; the differences also suggest that in reality the absorption profile is not unresolved since the RTA would reduce to the UTA model in that case*

radiation transport this is often not the case.

The implementation of the RTA model in IMP was motivated by an in depth study of UTAs and their effect on opacity calculations. A full account of this is given in section 7.

## 5.4 Electron Impact Broadening

The application of opacity codes to higher densities requires a more detailed treatment of the effect of the surrounding plasma on the states of ions. As discussed in section 2.8 these interactions manifest themselves as perturbations to atomic energy levels and introduce a extra shape to absorption lineshapes and edges. At intermediate densities perturbations to atomic transitions by electrons are important and so should be included in calculations.

Such effects have been known to be important to astrophysical emission lines for many years and so much work has been devoted to the subject [115], culminating in a series of papers by Baranger [36, 37, 38] in which a fully quantum mechanical treatment is set out. These results are formulated in terms of the

‘impact approximation’, in which the average electron - atom collision is weak and so the change in atomic wavefunction due to the interaction is neglected. This is a low density or high temperature approximation. The emitted power from an atomic transition in the presence of a set of electron perturbers is calculated quantum mechanically given the assumption that the perturbers do not interact with each other; the electron impact approximation consists of assuming that it is the state of the system at large times after the interaction that is important. The significant result is that the lineshape due to collisions with electrons is Lorentzian and that the half width  $\gamma_{EI}$  can be calculated from the inelastic scattering cross sections  $\sigma$  and elastic scattering amplitudes  $f$  of the initial and final atomic states;

$$P_{ei}(\epsilon) = \frac{1}{\pi} \frac{\gamma}{(\epsilon - \epsilon_0)^2 + \gamma^2} , \quad (5.4.1)$$

$$\gamma_{EI} = \frac{1}{2} \hbar N \left\langle v \left[ \sum_{i'} \sigma_{i'i} + \sum_{f'} \sigma_{f'f} + \int |f_i(\theta, \phi) - f_f(\theta, \phi)|^2 d\Omega \right] \right\rangle_{Av} , \quad (5.4.2)$$

where the summations run over all transition channels that are available to the initial and final atomic states. The  $\sigma_{ij}$  are inelastic cross sections for transitions between the  $i^{\text{th}}$  and  $j^{\text{th}}$  atomic states; the final term is the change in the scattering amplitude of the atom due to the transition and represents elastic collisions. As well as the width the centre of the absorption line is shifted according to an expression similar to equation (5.4.2).

Calculation of the scattering cross sections required by the above model from first principles can be a significant problem and so there has been a large amount of work devoted to finding a simplified model. These are based on the work of Born and Bethe, in which the inelastic cross section is given by

$$\sigma_{i'i} = \frac{8\pi^2}{3^{3/2}} \frac{E_H}{E_e} |\langle i' | \mathbf{r} | i \rangle|^2 g(E_e) , \quad (5.4.3)$$

where  $E_e = 1/2 m_e v^2$  is the kinetic energy of the perturbing electron and  $g(E_e)$  is a Gaunt factor. This encapsulates any modifications to the Bethe-Born result due to quantum mechanics, electron energy thresholds, elastic scattering, *etc.* Griem [116] produced his ‘semiempirical’ model for  $g(E_e)$  by considering the classical path approximation (valid for light perturbers and weak collisions) and including a correction for

strong collisions and elastic scattering. Dimitrijevic and Konjevic [117] then extended this work to high ionisation stages; the same authors then approximated (5.4.3) using hydrogenic matrix elements to derive their well-known simple model [118].

In IMP calculations it is not necessary to use hydrogenic matrix elements since they are already calculated in the form of the oscillator strengths for dipole transitions. We therefore find the summations in equation (5.4.2) as a sum over the 20 largest single electron dipole transitions out of the initial and final jumping electron states, averaged over a Maxwellian electron distribution. For the Gaunt factor we use the modified semiempirical model discussed above;

$$\bar{g}(x) = \begin{cases} 0.7 - \frac{1.1}{Z} + g & \text{if } \Delta n = 0 \\ g & \text{otherwise} \end{cases},$$

$$g = \begin{cases} g_{QC} & \text{if } g_{QC} \geq 0.2 \\ 0.2 & \text{otherwise} \end{cases},$$

$$g_{QC} = \frac{\sqrt{3}}{\pi} \left\{ \frac{1}{2} - \frac{1}{2} \left[ \frac{(Z+1)\eta}{4\pi^2} \right]^2 + \log \left[ \frac{(Z+1)}{2n^2} \frac{E}{|E_{i'i}|} F(\varepsilon) \right] \right\},$$

$$E = \frac{3}{2} k_B T \quad \eta = Z \sqrt{\frac{E_H}{E}} \quad \varepsilon = \frac{1}{2} \eta \frac{|E_{i'i}|}{E} \quad F(\varepsilon) = \varepsilon \sqrt{\frac{5 + 4\varepsilon + \varepsilon^2}{1/2 + 2\varepsilon + \varepsilon^2 - 1/2\sqrt{1 + 8\varepsilon}}}.$$

In the evaluation of the above the ion stage  $Z$  is replaced by the mean ionisation  $Z^* + 1$ , and the transition energy is calculated in the average atom approximation. Finally, single electron oscillator strengths between the initial and final radiative states and each perturbing state are used in equation (5.4.3) to give the required cross sections. These approximations allow the electron impact widths to be calculated outside of the DCA loop with almost no numerical penalty. The use of single electron oscillator strengths is a particularly poor approximation however the corresponding errors can be expected to be consistent with the inaccuracies in the method of Dimitrijevic and Konjevic (on which this approach is based), and the computational advantages are large.

To that end we return to the Aluminium data of Hoarty *et al.* [106], which we discussed in section 5.2. This experiment measured transmission spectra for aluminium at around 60 eV and 1 g/cc, under which

conditions the plasma is strongly coupled ( $\Gamma \sim 3$ ) and so the interaction between the plasma and the atomic system is large. Indeed, Hoarty *et al.* report that the large  $1s \rightarrow 2p$  transition in the data can only be correctly described when electron impact broadening is used, and that this broadening mechanism is dominant. We therefore aim to compare large scale modelling of the experimental data using the upgraded IMP calculations to that using the CASSANDRA code. Calculations using CASSANDRA use an improved equation of state and atomic model, have extra line broadening effects, and include a more complex description of electron impact broadening compared to IMP and so the comparison should be very informative.

The data are shown in figure 5.6, where we begin by plotting the experimental and IMP results. In the reference it was suggested that gradients in the sample could be accounted for by combining calculations performed at  $T = 55$  eV,  $\rho = 0.9$  eV;  $T = 59$  eV,  $\rho = 1.0$  g/cc;  $T = 63$  eV,  $\rho = 1.1$ ; this has been done for the IMP data, and a Gaussian instrument function corresponding to a resolving power of 500 has been included. The IMP calculations themselves have been run using the HFS model described previously and the UTA model. In order to include the Lorentzian lineshape due to electron impact broadening the code now uses Voigt profiles (this will be discussed in the following section). The IMP calculations presented in figure 5.6 require around 4 CPU minutes of runtime for each set of plasma conditions.

In the figure heavy red lines show data from IMP that include electron impact broadening; fine lines show the same calculations where these widths are neglected. The IMP data have been shifted upwards in energy by 10 eV to align the  $1s \rightarrow 2p$  absorption features. The effect of electron impact broadening on the calculation is clear, and acts to smooth out the various  $1s \rightarrow 3p$  transition arrays at the high energy end of the spectrum. The shapes and widths of transition arrays appear to be better described by the unbroadened model however the overall transmission through the sample is much higher than in the experiment. This poor agreement is over the entire spectral range of the experiment and is largest in regions of high transmission; this suggests that there may be a problem with the areal density used to calculate the transmission.

The data shown in figure 5.6 have been calculated using the areal density quoted by Hoarty *et al.*,  $\rho L = 6 \times 10^{-5}$  g/cm<sup>2</sup>. If instead the areal density is used as a fitted parameter then the best fit between broadened IMP data and experiment occurs when  $\rho L = (1.52 \pm 0.06) \times 10^{-4}$  g/cm<sup>2</sup>. This is a large change from the value quoted in the reference but is in reasonable agreement with the initial areal density of the



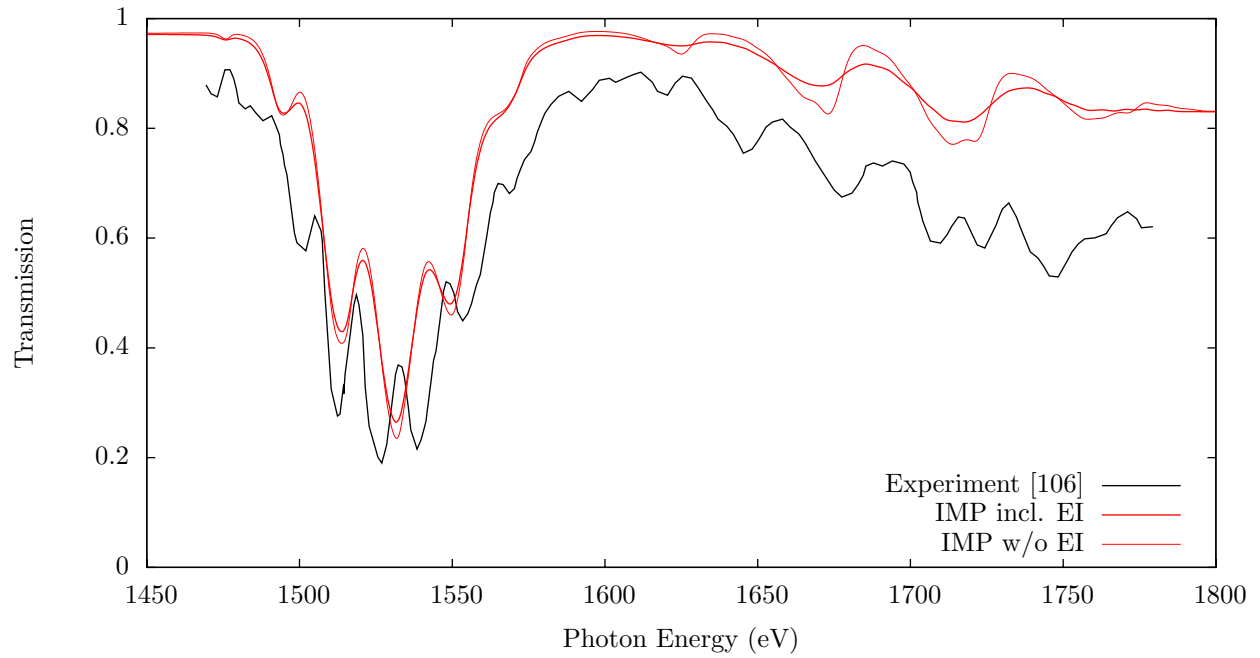


**Figure 5.6:** The transmission through an Aluminium plasma of areal density  $\rho_a = 6 \times 10^{-5} \text{ g/cm}^2$ . The experimental data due to Hoarty et al. are compared with the IMP model with and without electron impact (EI) broadening. The total transmission is poorly described over the entire spectral range.

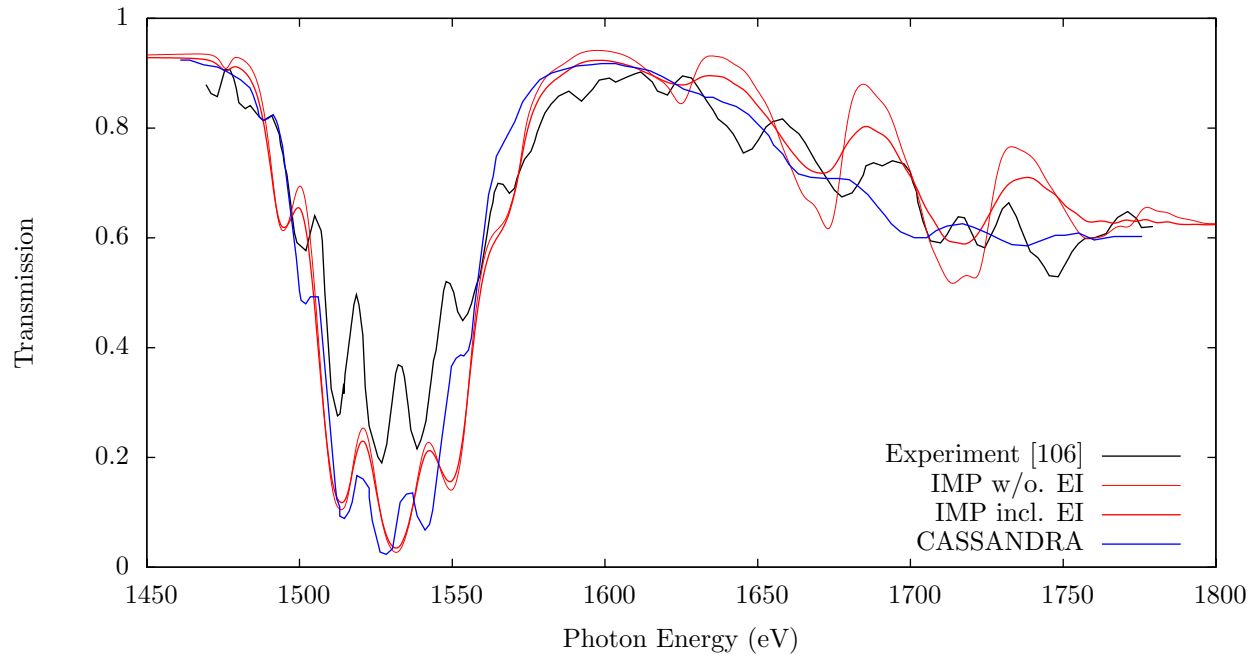


**Figure 5.7:** The same IMP calculations as shown in figure 5.6 are shown, calculated with a fitted areal density of  $(1.52 \pm 0.06) \times 10^{-4} \text{ g/cm}^2$ . This gives a much improved description. Also shown are calculations using the CASSANDRA opacity code, which includes a much more detailed opacity model. The IMP calculations now compare with experiment and large calculations extremely well, validating the simple electron impact model described in the text.

solid Al foil target,  $2.7 \text{ g/cm}^3 \times 0.5 \mu\text{m} = 1.35 \times 10^{-4} \text{ g/cm}^2$ . The IMP data with this new areal density are plotted along with CASSANDRA results in figure 5.7. The figure shows an excellent agreement between the two opacity codes and the experiment; the increased areal density has brought the overall transmission in line with the experiment (as expected) and the widths of the various transition arrays in the experimental data are well described by the IMP code provided the electron impact width is included. The line widths in IMP calculations compare favourably with the more detailed CASSANDRA calculations, suggesting that the errors in the fast model described above are comparable with those of slower models. In the region of the  $1s \rightarrow 2p$  transition the transmission is too low when calculated using both models, however the agreement between IMP and CASSANDRA suggests that this is not a problem with the simplicity of the IMP approach. It is more likely to be due to departures from LTE or the simple description of sample gradients. In general the IMP code gives an excellent description of the data.

In the reference Hoarty *et al.* suggest that the structures that we have identified as  $1s \rightarrow 3p$  transition arrays are actually due to experimental noise and the  $K$  shell edge, implying that the  $3p$  states are not bound in the experimental plasma. In the IMP calculations single electron states up to  $3\bar{d}$  remain bound and so if no evidence for the  $1s \rightarrow 3p$  in the experimental spectrum this would be evidence of problems in the description of continuum lowering in IMP. We have already seen evidence for this in the description of the mean ionisation of carbon in section 5.2. In fact the structures in the experimental spectrum around 1600-1750 eV align well with the  $1s \rightarrow 3p$  structures predicted by IMP and so we conclude that there is little evidence for problems with the continuum lowering model at the high density of this experiment.

## 5.5 Absorption Lineshapes

In the simplest approximation the electron impact broadening process described previously introduces a Lorentzian line profile (5.4.1) which must be convolved with the Gaussian lineshape due to inhomogeneous broadening processes. This results in the Voigt line profile

$$V(\epsilon) = \frac{1}{\sqrt{2\pi}\sigma_\epsilon} e^{-\frac{(\epsilon_0 - \epsilon)^2}{2\sigma_\epsilon^2}} \otimes \frac{\gamma}{\pi} \frac{1}{(\epsilon - \delta\epsilon)^2 + \gamma^2} = \frac{1}{\pi^{3/2}} \frac{1}{\sigma_\epsilon} \frac{\gamma}{\sigma_\epsilon} \int_{-\infty}^{\infty} \frac{e^{-z^2}}{\left(\frac{z - \epsilon_0 + \Delta\epsilon}{\sqrt{2}\sigma_\epsilon}\right)^2 + \left(\frac{\gamma}{\sqrt{2}\sigma_\epsilon}\right)^2} dz, \quad (5.5.1)$$

where  $\gamma$  is the half width of the Lorentzian function,  $\sigma$  is the standard deviation of the Gaussian, and  $\Delta\epsilon$  is the relative shift of the two profiles. The integral cannot be found analytically and so must be numerically integrated or approximated at considerable numerical cost.

The importance of the Voigt profile to the interpretation of atomic spectra has been realised for many years and so there are many options for calculating the integral in equation (5.5.1). Direct numerical integration is inefficient but may be used to generate lookup tables however the interpolation errors can be severe; a more efficient method is to perform the convolution in Fourier space analytically and to numerically transform back using fast routines [111]. The integral can also be split into separate regimes and evaluated using quadrature routines [119, 76], which converge in a reasonable ( $\sim 10$ ) number of terms. Such approaches are suitable when a small number of profiles are required however in the case of large-scale, high resolution opacity calculations they represent a very large computational overhead. We instead resort to the use of algorithms that have been designed to be fast. If the errors in line shape associated with these algorithms are small compared to the calculation of the line widths they will be sufficient provided they are correctly normalised; if this is not the case line strength will be lost from the code.

We consider two fast algorithms, due to Whiting [120] and Humlicek [121], which are summarised in a paper by Schreier [122]. These routines provide very fast evaluation of the Voigt function by splitting the profile into various regions and applying functional fits. Their accuracy is rated by their ability to reproduce the correct full width at half maximum (FWHM) and so it is informative to examine the lineshapes in more detail. To that end we compare the Voigt profile as calculated using each algorithm with full calculations in figure 5.8. In the figure we plot the RMS fractional error in the profile, averaged over 50 full width half maxima, when compared to results from direct numerical evaluation of equation (5.5.1). The figure demonstrates that the Humlicek method gives far better results than the Whiting method; this can be seen from the 10% error contours which are marked in the figure with cyan lines. The region in which the Humlicek method is better than 10% accurate spans much of the calculation range, whereas for the Whiting method this is not the case. The interesting regime where the two line components are of comparable width is not well described by the Whiting method whereas the error in the Humlicek result has a minimum in this case; we therefore propose to use the Humlicek algorithm in IMP calculations when required. In this case

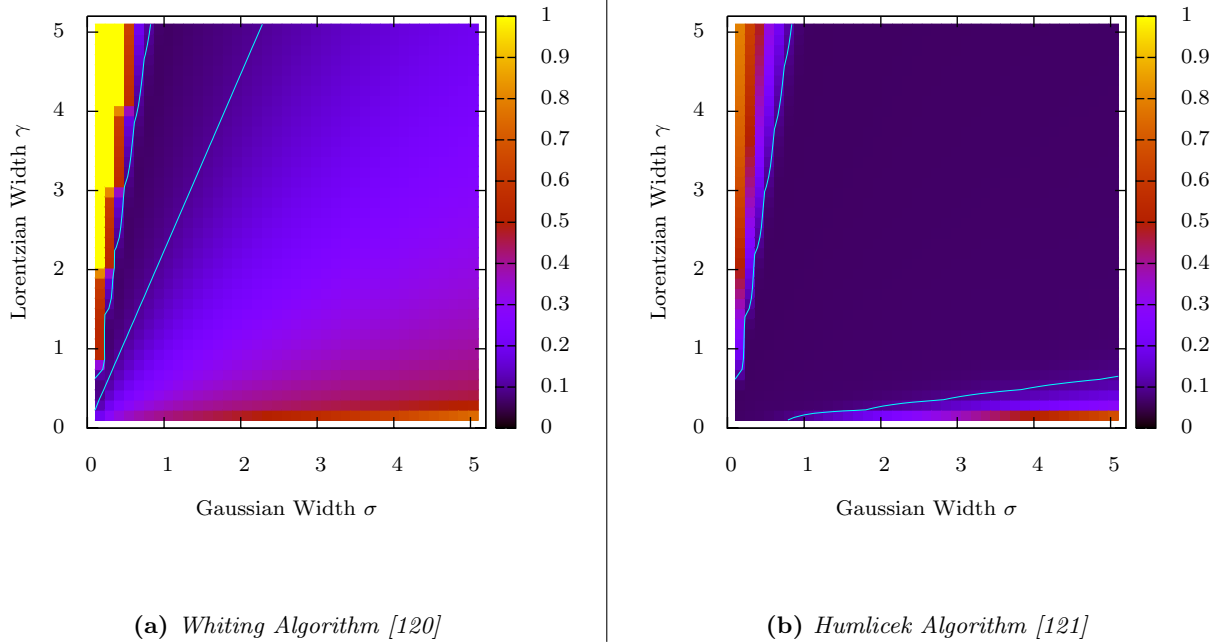


**Figure 5.8:** The RMS error in the Voigt profile calculated using the Whiting (a) and Humlicek (b) algorithms when compared to numerical convolution. The values shown are calculated over a range equal to 50 full width half maxima. Also shown are the 10% error contours; it can be seen that while both algorithms fail when one line component dominates, the range where the Whiting model is better than 10% accurate is very small compared to that of the Humlicek algorithm.

the results in figure 5.8(b) show that the lineshape will be better than 10% accurate when  $0.1\sigma < \gamma < 6\sigma$ ; outside this range, however, it is still more accurate to use the Humlicek result than to resort to the single component lineshapes.

All that remains is to test the normalisation of the Voigt profile obtained from Humlicek calculations. Calculations over the same range of widths as in the previous analysis show that in regions where the profile itself is reliable the normalisation agrees to much better than 0.1%. Updated IMP calculations can therefore use the Humlicek algorithm without correcting the normalisation numerically.

## 6 Convergence of Fast Opacity Calculations

Regardless of the complexity or focus of an opacity code, the problem of a partially ionised plasma will always be a difficult one. In order to describe heat transport a large spectral range is required and so the volume of calculations places limits on the calculation time for each absorption feature. We have introduced methods by which this individual calculation time can be reduced; in this section the problem of optimising a calculation such that these are performed the minimum number of times is discussed.

### 6.1 The Volume of Calculations in Forming the Opacity

The DCA model used in IMP opacity calculations has been described in section 5.1, and in this section we aim to show the problems that can arise even when using this simplified model.

We begin by considering the number of configurations that are generated when a principle quantum number shell is opened. This quantity can be calculated in various ways depending on the level of resolution required; the most complete consideration considers all states  $n\ell jm_j$  separately, in which case the number of configurations is

$$N_{nljm_j} = \sum_{i=0}^{2n^2} \binom{2n^2}{i} = 2^{(2n^2)},$$

where  $n$  is the principle quantum number of the open shell. It is more efficient to treat states according to the quantum numbers  $n\ell j$  only, in which case the number of configurations becomes

$$N_{nlj} = \prod_{\{j\}} (2j + 1).$$

The number of configurations that must be included in these approximations for different open shells are shown in table 6.1, where it can be seen that the effect of a reduced state resolution gives a very significant decrease in the number of configurations that are generated over the course of a DCA calculation. We also show the number of configurations when described by the occupation of shells only. Note that in plasmas with no applied external field the largest resolution is not required since states of the same  $n\ell j$  are degenerate. It is also important to note that the number of configurations increases very quickly with increasing  $n$  in

| $n =$            | 1 | 2   | 3                 | 4                 | 5                    | 6                    | 7                    | 8                    |
|------------------|---|-----|-------------------|-------------------|----------------------|----------------------|----------------------|----------------------|
| $N_{n\ell jm_j}$ | 4 | 256 | $2.6 \times 10^5$ | $4.3 \times 10^9$ | $1.1 \times 10^{15}$ | $4.7 \times 10^{21}$ | $3.2 \times 10^{29}$ | $3.4 \times 10^{38}$ |
| $N_{n\ell j}$    | 3 | 45  | 1575              | $9.9 \times 10^4$ | $9.8 \times 10^6$    | $2.7 \times 10^{11}$ | $2.7 \times 10^{13}$ | $2.3 \times 10^{16}$ |
| $N_n$            | 3 | 9   | 19                | 33                | 51                   | 73                   | 99                   | 129                  |

**Table 6.1:** The number of configurations that must be calculated in a DCA opacity calculation opening various principle quantum number  $n$  shells. The different calculations resolve electron states to different levels; it can be seen that a reduced resolution leads to significantly smaller workload and that a higher  $n$  valence shell leads to a very large number of configurations.

both cases, making plasmas with many bound electrons a very difficult problem. In the case of new IMP calculations where 2 or 3 valence shells are opened the relevant entries in table 6.1 must be multiplied.

As we have already discussed, the structure of an opacity code means that the calculation time increases essentially linearly with the number of transition lines included. Each extra configuration gives rise to a large number of transitions and so an increase in the number of initial ion configurations, due to a higher resolution model or a calculation with more open shells, will lead to a rapid increase in the calculation time. In IMP calculations, once a configuration is included all the absorption lines that can arise are included in the spectrum; this means that reductions in the number of configurations can be a very efficient way of decreasing calculation time. It is therefore very interesting to develop a method of including only the most important configurations and the rest of this section will be devoted to this problem.

## 6.2 Identification of Important Absorption Features

We have introduced the need for opacity calculations to include a description of all the bound-bound transitions that can occur in a plasma; in fact only features that produce an appreciable change in the opacity are required to give a good description. The integrated opacity of a transition line is proportional to the transition strength  $S_{if}$  and the probability of an ion residing in the initial state  $p_i$ . In order to gain a good description of the bound-bound opacity, then, it is only necessary to include absorption lines for which  $(S_{if} \times p_i)$  is larger than some cutoff which is chosen according to the desired accuracy of the final result.

In order to form an efficient method of choosing important transitions, some predictive capability is required; it is very inefficient to generate large numbers of transitions only to throw them away when the line strength is found to be small. Such an approach has proven useful in calculations using atomic databases

or hybrid models however the storage required for such models, and the time required to sort the input data, make such approaches unsuitable for the fastest opacity calculations. In this section we will focus on an alternative, and more easily applicable, approach based on the probability of the initial state. We will see that in this case a more structured approach can be taken.

When in LTE the probability of the initial ion configuration  $Q = \{n_i\}$  is [76]

$$P_Q = \frac{g_Q}{\Omega} e^{-\frac{1}{k_B T} (E_Q - \mu N_Q)} , \quad (6.2.1)$$

where  $g_Q$  is the total degeneracy of the configuration and  $\Omega$  is the partition function;

$$g_Q = \prod_i \binom{g_i}{n_i} , \quad (6.2.2)$$

$$\Omega = \sum_Q g_Q e^{-\frac{1}{k_B T} (E_Q - \mu N_Q)} . \quad (6.2.3)$$

The probability  $P_Q$  could be used to measure the importance of a configuration in a fast opacity calculation, however this approach suffers from the same problems as the examination of the line strength; the relevant configurations cannot be chosen *a priori*, rather all configurations must be chosen,  $P_Q$  calculated, and a choice made based on this probability. We therefore propose to approximate the configuration probability using binomial statistics, and to use the populations of each orbital to estimate the importance of an initial ion. In this case the probability of a configuration is maximised when the population numbers are equal to  $p_i g_i$ , where  $p_i$  is the occupation probability of the  $i^{\text{th}}$  single particle state. Therefore the configurations with the largest probability are those with occupation numbers that are close to the average values in each state.

In order to form the set of the most important configurations for an opacity calculation, it is then necessary to permute the occupation numbers away from their average values. For a high  $Z$  plasma there will be a large number of bound orbitals, all of which should be permuted. In fact only the orbitals with a significant population variance need be permuted, since these changes produce the smallest change in the configuration probability. This is the same argument as that used to choose the valence shells in original IMP calculations. In the binomial case the population variance is equal to  $g_i p_i (1 - p_i)$ , which is a maximum

for states with an occupation probability of  $1/2$ . The configurations that have a probability closest to the maximum can therefore be found by permuting the occupations of the states which lie closest to the Fermi energy.

The scheme described above gives the point at which the most probable configurations are expected to be found, and which single particle orbitals should be allowed to vary in order to stay in the region of the maximum in occupation-number space. It is not clear, however, how permutations of different orbital occupations will effect the probability relative to some other permutation. This is an important piece of information if an opacity code is to intelligently guess which configurations should be used. Such an approach seems unfeasible since the details of the probability distribution in occupation-number space depends on the relative sizes of the energy integrals which in turn depend on the details of the radial wavefunctions for each orbital. A more easily implemented method is to divide occupation number space into regions that contain all configurations that can be expected to contribute to a similar degree. These regions then define a parameter space on which the size of calculations can be defined, where a larger calculation can be expected to be more accurate.

In IMP calculations electron shells can be opened and limits placed on their populations. It is therefore convenient to define our parameter space in these terms; the space then has a number of dimensions equal to the number of open valence shells, and points have coordinates defined by the number of electrons in each shell. Then a point  $(N_{n_1}, N_{n_2}, N_{n_3})$  will represent the set of configurations that lie a certain distance from the mean population of the shell. In the above the numbers  $N_{n_i}$  are the total number of electrons residing in the shell with principle quantum number  $n_i$ . This reduced resolution model is a good compromise between requiring a very detailed description of the configurations to be included, and ensuring that the groups include states that contribute in the same way.

Using this model opacity calculations can be built, starting in a small region close to the mean populations of each shell, in a series of regions until convergence is achieved. This process is shown as a cartoon in figure 6.1, for the case where two valence shells are opened. The yellow point represents the (non integer) mean occupation numbers of the two valence shells, and the red shaded region is the smallest calculation that should be run. The degeneracy of the points included in this region can be quite large and so even this



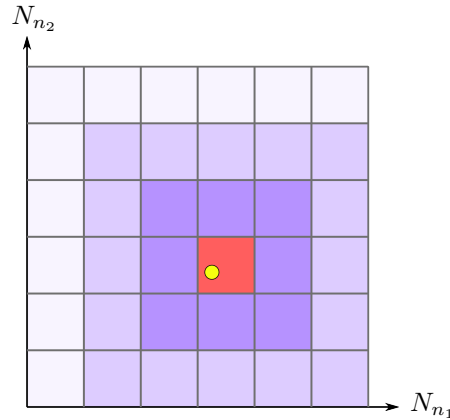


**Figure 6.1:** Cartoon showing the structure of occupation-number space used for opacity calculations. The yellow dot indicates the position of the mean shell populations, and concentric shaded regions correspond to calculations including more and more configurations.

calculation may be quite challenging. The consecutive blue shaded regions then represent calculations that include more and more configurations of smaller and smaller probability. At some point in the process the extra configurations will make little difference to the results of the calculation and so can be neglected.

### 6.3 Achieving Convergence

As the range of occupation-number space included in calculations is increased, the relative importance of configurations decreases and at some point the opacity calculation will converge. Quantifying this convergence is an important aspect of this scheme since it will prevent large numbers of configurations from being included unnecessarily. In this section we will discuss methods for achieving this.

The simplest, and most general, method of quantifying convergence is to inspect the frequency resolved opacity at the end of the calculation and compare it to the results from a slightly larger run. If the two calculations agree to within the desired accuracy the smaller calculation has converged. This has the obvious disadvantage that unless an opacity code has been designed to compare profiles as it goes, at least two calculations must be run for any case. One of these calculations needs to be large enough that the user is confident that it is correct, and since the size of the calculation will change with the plasma conditions this defeats the object of the convergence process in many situations.

We can find another option by considering the contribution to the opacity of a transition line. In the previous sections we used the fact that the contribution is proportional to the initial ion probability to motivate our convergence scheme. This probability is proportional to the partition function  $\Omega$  and so if this quantity is not found correctly then absorption lines will be given the wrong weighting in the output absorption spectrum. The partition function is formally the sum of the probabilities of all possible ion states however in an opacity code it will be calculated as the sum of the probabilities of all ions in the calculation. It is, therefore, very important that the ion stages in an opacity calculation are sufficient to correctly give the partition function.

In certain situations the inclusion of the most probable configurations may not be sufficient to ensure that  $\Omega$  is converged. This can happen due to the very rapid increase in the number of configurations around half-filled shells, the sheer volume of which may lead to a large contribution even if they are individually negligible. This is an important point as this could even cause a calculation to be found to be converged when it is not, and is particularly important when the open valence shells have a large degeneracy in which case the increase in the number of configurations is particularly fast. The important point here is how fast the probability distribution falls off away from the central peak; if the peak is so sharp that it can overcome the increase in number of configurations then the scheme described in section 6.2 should provide a converged partition function. In the remains of this section we will present results that aim to test this.

The number of configurations represented by each point in occupation-number space is a difficult quantity to calculate since occupation numbers of each state in the shell are not independent. Similarly the probability of a given configuration cannot be simply described in terms of the occupation numbers. We therefore resort to using the IMP code to investigate the contribution of each point to the partition function.

We will begin by considering the conditions of a recent experiment due to Hoarty *et al.* [96]. In this experiment X-rays produced by the HELEN laser irradiated a niobium target, buried in a layer of plastic. Spectra were collected in the 2350 – 2700 eV range for four separate plasma conditions. The differences in plasma conditions lead to a large change in the observed spectra however little difference in the probability distribution and so we will only present one set of data, for  $T = 30$  eV and  $\rho = 0.028$  g/cc. Figure 6.2 shows a logarithmic colour map of the contribution to the partition function of configurations at each point

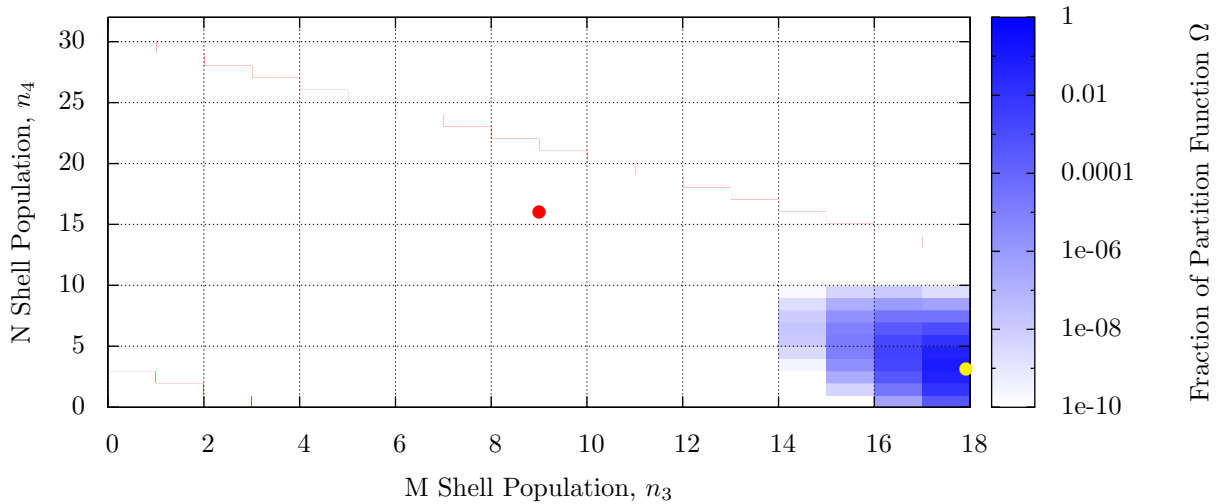


**Figure 6.2:** The fraction of the partition function  $\Omega$  due to configurations at different points of occupation-number space, calculated for a niobium plasma at 30 eV and 0.028g/cc. The yellow point indicates the average occupation numbers, and the red point shows the peak in the degeneracy of regions of the space. It can be seen that the probability distribution is sufficiently peaked that only a small region of occupation number space is required to converge the partition function.

in occupation-number space. Under the conditions of the experiment the mean populations of the  $M$  and  $N$  shells are 17.9 and 3.2 respectively, and so the parameter space is two dimensional. Also marked on the plot are the position of the peak of the probability distribution in yellow, and the peak in the degeneracy in red. It can be seen that the distribution is very peaked, making it easy to converge the partition function to high accuracy using a relatively small subset of the possible configurations. The rapid increase in the degeneracy of the parameter space points does not cause any problems however the distribution is seen to be slightly asymmetric which may be a symptom of the increasing number of configurations along the diagonal in the plot.

In order to investigate the effect of configuration degeneracy further, we reduce the plasma temperature for the same density in order to shift the peak of the probability distribution closer to the centre of the  $N$  shell. The variation in the number of configurations across the peak of the probability distribution is then much larger. The results for four temperatures,  $T = 20, 15, 10$  and 5 eV are shown in figure 6.3. It can be

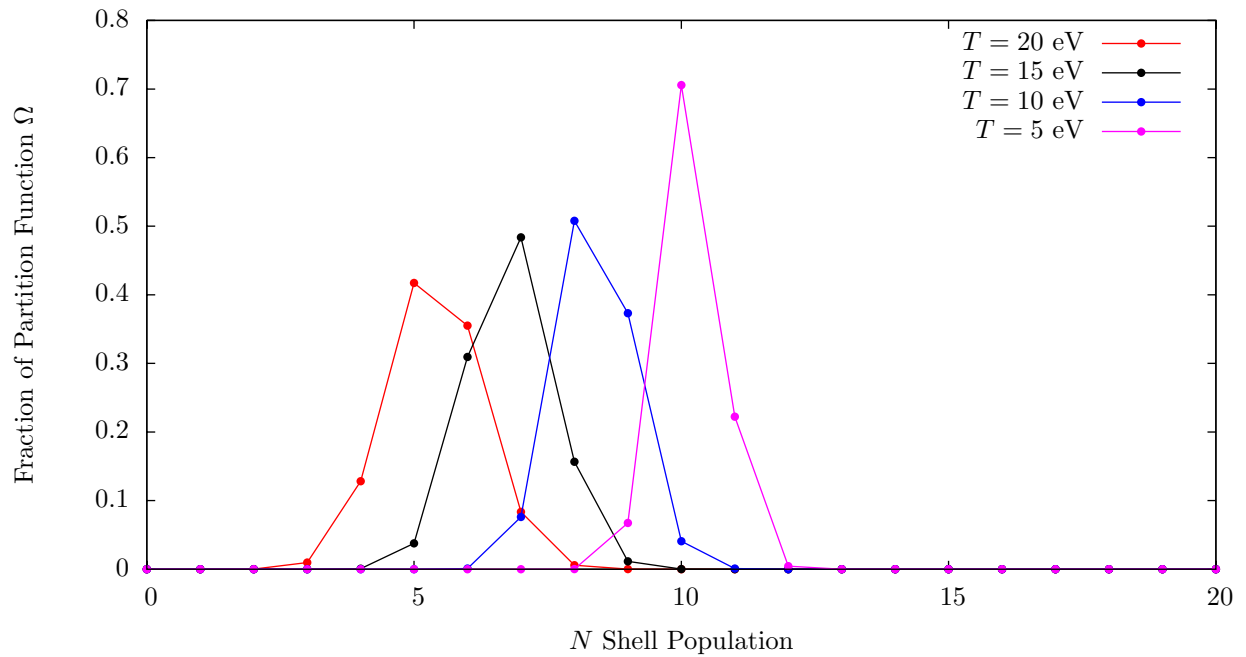


**Figure 6.3:** *As with figure 6.2, but with a reduced temperature. In this case only a single shell must be opened, and the probability distribution is peaked close to the peak in the degeneracy. Even under these conditions, where the number of configurations is rising very rapidly, the partition function can be converged by considering a small region of occupation-number space.*

seen that as the temperature increases the population of the  $N$  shell is reduced, as expected, and that the distribution is broadened. For the lowest temperature, which lies closest to the half-filled shell population (16), the previous result still holds; the partition function is still determined by those configurations of the largest probability, regardless of the degeneracy. In fact, it appears in figure 6.3 that the narrowing of the probability distribution is sufficient to balance the larger number of configurations. This balance is not complete, and many more configurations are required to converge the 5 eV case than the 20 eV.

The results presented in this section have shown that the use of a parameter space based on the occupation numbers of valence shells can give a good method of reducing the number of configurations in calculations and therefore the calculation time. Using this scheme the partition function can be converged quickly, so that the bound-bound and bound-free contributions to the opacity will be correctly weighted. Ensuring that the partition function is converged also ensures that absorption lines of the largest probability and degeneracy are included in the calculation, however in order for the frequency resolved opacity to be converged the line strength must also be taken into account. This requirement can be included by extending the convergence

criteria on the partition function so that the neglected configurations not only contribute a negligible amount to  $\Omega$ , but also that the lines that arise from neglected configurations are not important regardless of their strength. This approach is investigated in the following section.

## 6.4 The Frequency-Resolved Opacity

We return to the experimental work of Hoarty *et al.* [96], and choose two of the experimental data sets, with conditions  $T = 30$  eV,  $\rho = 0.028$  g/cc and  $T = 41$  eV,  $\rho = 0.025$  g/cc. For each of these conditions the convergence of the frequency resolved opacity is investigated as the portion of population-number space included is increased, with the aim of determining the criteria for a converged opacity calculation.

As was seen in the previous section, at both of these conditions both the  $M$  and  $N$  shells are open and so the parameter space for our calculations is two dimensional. Such a situation was dealt with easily in the previous section as we did not generate spectra; since we now wish to examine the frequency-resolved opacity, calculations takes a significantly longer time and it is not possible to include the entire parameter space. We therefore begin in a region closely surrounding the mean shell populations and move outwards until the opacity profile does not change between calculations. For the same reason calculations will use very simple lineshapes and will be at fairly low resolution; this will not effect our conclusions but will make a significant difference to the runtime of calculations.

We begin by considering the lower temperature case, the partition function distribution for which is shown in figure 6.2. In this case the smallest region of parameter space we can consider contains configurations with between 17 and 18 electrons in the  $M$  shell and between 3 and 4 in the  $N$  shell. The size of calculations is then incrementally increased in separate calculations. Various properties of these calculations as the size of the parameter space is increased are shown in table 6.2. The table defines the 5 test calculations performed and compares the number of configurations and calculation times of each. We also give the partition function found from each calculation, referenced to the value found from the largest case, along with a measure of the convergence of the frequency resolved opacity profiles of each. This is found by calculating the root mean square (RMS) fractional difference between the opacity at each photon energy point and the corresponding opacity found in the largest calculation.

| Run | Shell Occupations    | No. Configurations | Calculation Time (CPU-s) | $\Omega$ | Convergence          | $\kappa_R$ (cm <sup>2</sup> /g) |
|-----|----------------------|--------------------|--------------------------|----------|----------------------|---------------------------------|
| 1   | $N_M:17-18; N_N:3-4$ | 1668               | 40                       | 0.675    | 0.488                | $5.25 \times 10^3$              |
| 2   | $N_M:16-18; N_N:2-5$ | 14910              | 158                      | 0.957    | 0.058                | $5.40 \times 10^3$              |
| 3   | $N_M:15-18; N_N:1-6$ | 78840              | 776                      | 0.988    | 0.002                | $5.42 \times 10^3$              |
| 4   | $N_M:14-18; N_N:0-7$ | 308484             | 3004                     | 1.000    | $1.8 \times 10^{-5}$ | $5.42 \times 10^3$              |
| 5   | $N_M:13-18; N_N:0-8$ | 964080             | 11194                    | 1.000    | -                    | $5.42 \times 10^3$              |

**Table 6.2:** The variation of various parameters of IMP calculations of the opacity of niobium at 30 eV and 0.028 g/cc as larger regions of population-number space are included. The partition function  $\Omega$  is given as a ratio with the largest calculation, and the ‘Convergence’ column gives the RMS fractional difference with the largest calculation. It can be seen that in this case the requirement that the partition function is converged is significant to converge both the frequency resolved and Rosseland mean opacities.

The data given in the table first of all demonstrate explicitly the rapid increase in calculation time associated with a larger calculation, with calculations increasing from under a minute on a single CPU to over 3 hours. There is little advantage to running calculations at the higher end of this scale, however, since both the frequency-resolved and Rosseland mean opacities are converged to good accuracy for the mid-size calculations in table 6.2. The table also shows the complex relationship between these two forms of the opacity; in the first case, the partition function is a little over  $2/3$  of its true value making the contribution from absorption lines too small and resulting in a large RMS fractional error. This large error is not carried through to the Rosseland mean opacity, however, where a deviation of only 3% is seen. This is due to the spectral range in our calculations, which run from 0 to 3 KeV, including large regions where there are no lines. These windows in the spectrum dominate the Rosseland mean.

We now turn to the frequency resolved opacity, which we plot for the first 4 test cases in figure 6.4. We plot the opacity in the spectral range around the  $K$  shell edge, and include the range of the experimental collected by Hoarty *et al.*. The effect of increasingly large calculations is clear; new absorption lines appear in the spectrum and existing features broaden as spectator transitions are taken into account. As discussed in section 5.1 placing limitations on the populations of valence shells causes the usual dielectronic broadening model to be inaccurate, and so in cases where calculations are not converged many spectator transitions are neglected. Finally, since we are moving away from the most probable configurations in a symmetric manner we expect the average ionisation of ions in the DCA calculation to be approximately the same in each test case; for this reason it is difficult to see any pattern in the appearance of absorption lines.

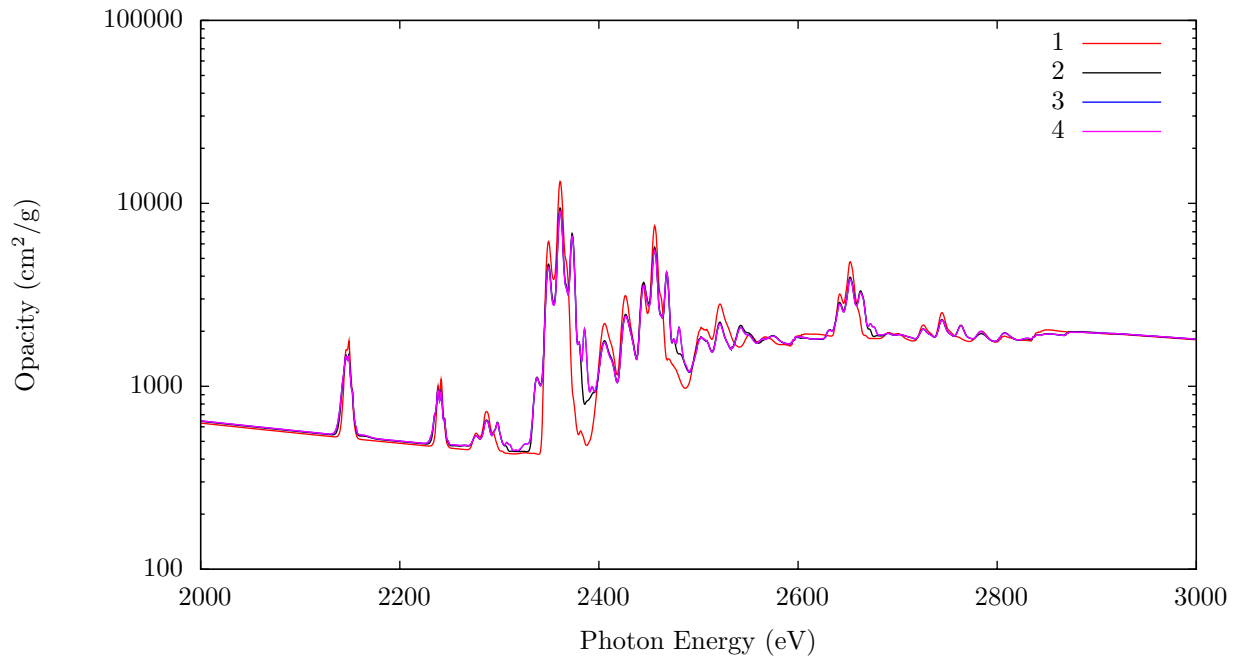


**Figure 6.4:** *The convergence of the frequency resolved opacity of niobium at  $T = 30$  eV and  $\rho = 0.028$  g/cc as the size of calculations are increased. The calculations are referenced to the conditions given in table 6.2, and data are plotted for the spectral region surrounding the L absorption edge, and correspond to the range of the data collected by Hoarty et al.*

The previous data have shown that in the case of niobium at 30 eV and 0.028 g/cc, convergence of the partition function is sufficient to give a good result for the optical properties of a plasma. Calculations for the higher temperature case give similar results, however due to the broader probability distribution the shell occupation numbers must be allowed to vary over a larger range than in the previous example. Even with this larger range, the lower average populations mean that the calculation times at high  $T$  are lower than those given in table 6.2.

The results for the frequency resolved opacity at the higher temperature are shown in figure 6.5. The broader probability distribution at higher  $T$  means that the calculations over small regions of occupation-number space show very poor convergence (1.15 for the smallest case); this can be seen in the figure, where smaller calculations miss many large lines and overestimate the strength of the existing absorption features. As in the previous case convergence is achieved rapidly, in line with the partition function.

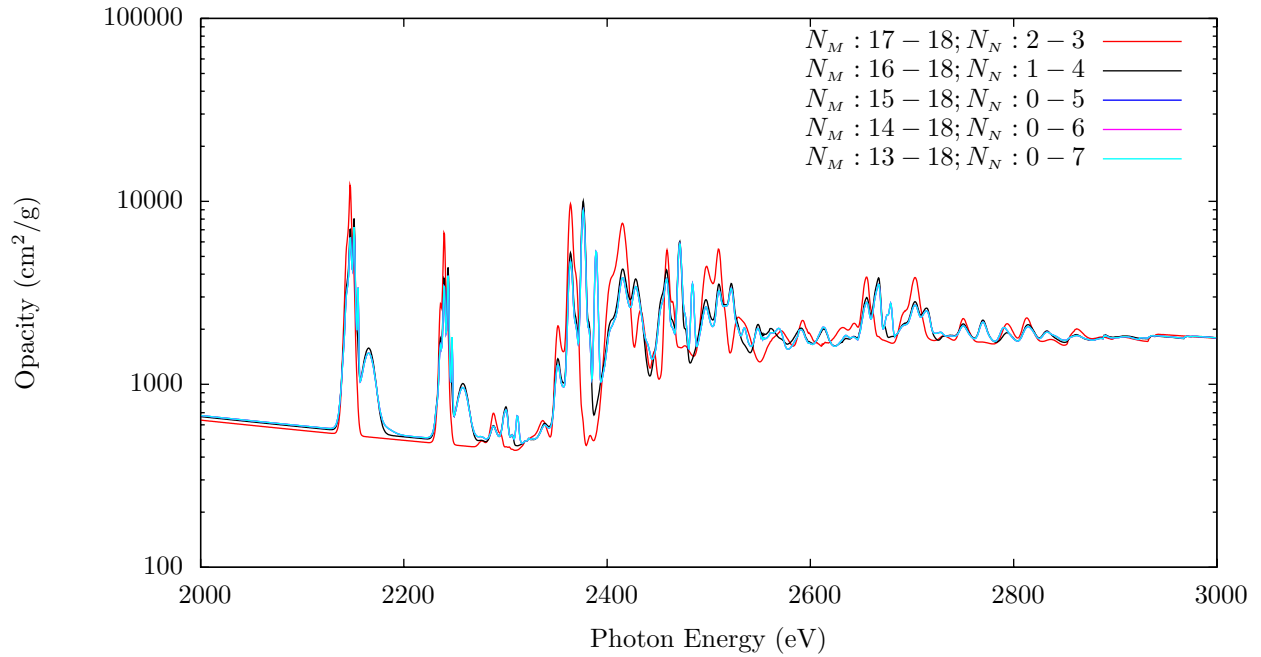


**Figure 6.5:** Convergence of the frequency resolved opacity of niobium at  $T = 41$  eV and 0.025 g/cc. Due to the higher temperature and therefore broader configuration probability distribution, the disparity between small and large calculations is much greater than in the previous example (figure 6.4). The partition function can still be used as a measure of convergence in this case.

## 6.5 Comparison with Experiment

The convergence procedure described above now allows the IMP code to efficiently model the experimental data of Hoarty *et al.* [96]. This will allow further conclusions to be made regarding the improvements made to the code, which are discussed in section 5, and on the effectiveness of fast opacity models in general.

As in the previous section, we choose two sets of data from the work of Hoarty *et al.*. In this experiment time integrated transmission spectra were collected in order to diagnose the opacity of the niobium sample. We therefore need to account for temporal and spatial gradients in the data, and convert the output from IMP to transmission. Gradients are accounted for by averaging a set of calculations at different conditions as described in section 2.4; the conditions which best fit the experiment were estimated in the original reference and we use these in our analysis. In order to convert to transmission we use equation (2.4.3) for small optical depth along with the experimentally determined areal density  $\rho L$ .

Since we now aim to test the various improvements that have been made to the IMP code, the calculation



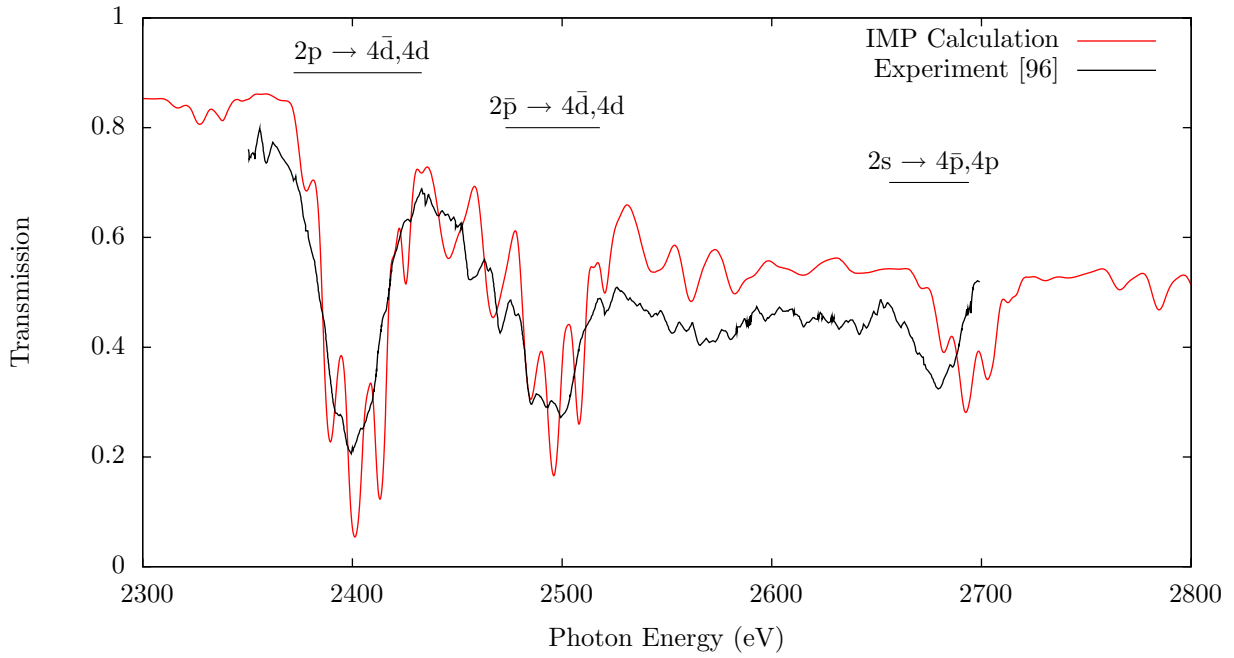
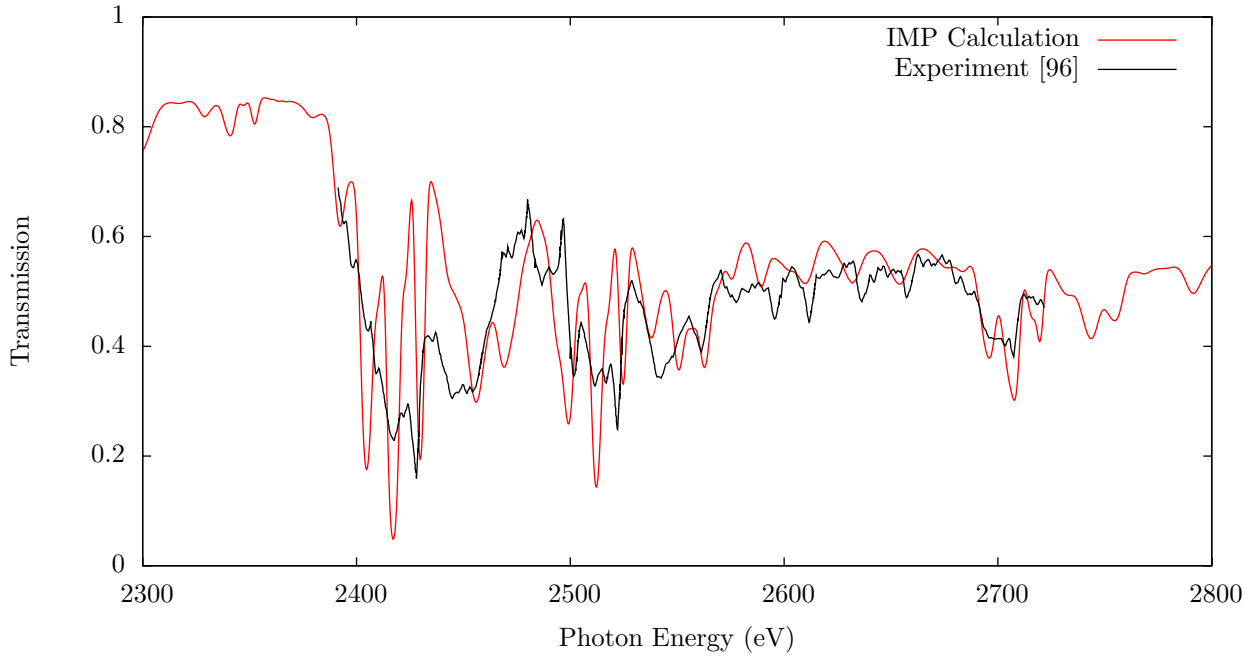
times will be significantly longer than in previous sections. We therefore present runs using parameters that give a convergence (as defined previously) of better than 5%, which in the previous low resolution runs required around 10 CPU minutes of runtime. Using a resolution high enough to give a good calculation of the Rosseland mean increases this to over an hour; however it should be noted that these calculations would not be possible without the considerations described in the previous sections.

We begin by presenting results found using the Hartree-Fock-Slater model described in section 5.2, Voigt line profiles (section 5.5) with Doppler, uncorrected dielectronic and electron impact broadening included, and the UTA model. The UTA model is tested in detail in the following chapters; in this section we are interested in other aspects of the IMP model. The data are shown for the two plasma conditions in figure 6.6(a) and (b) respectively.

In the case of the lower temperature, shown in figure 6.6(a), the gradient correction is performed by including equal components of  $T = 29$  eV,  $\rho = 0.026$  g/cc;  $T = 30$  eV,  $\rho = 0.028$  g/cc and  $T = 31$  eV,  $\rho = 0.031$  g/cc. Similarly for the higher temperature we use  $T = 39$  eV,  $\rho = 0.020$  g/cc;  $T = 40$  eV,  $\rho = 0.024$  g/cc and  $T = 41$  eV,  $\rho = 0.025$  g/cc. The opacity is averaged over these sets of plasma conditions, the transmission is calculated, and this is then convolved with a Gaussian instrument function of width corresponding to the experimental resolution  $R = 2500$ .

At the lower temperature the agreement between calculation and experiment is generally good; the large 2p→4d and 2s→4p transition arrays appear, and have the correct average strength. It should be noted that the calculated data have been shifted by 40 eV in order to align the large arrays on the lower energy side of the spectrum. This shift is sufficient to align the arrays that originate in the 2p orbital, however the higher energy 2s→4p transitions are not aligned with experiment. This is due to the known error in the LDA approach discussed in section 3.3. The error in the average transition through the plasma for the absorption window between 2500 and 2700 eV is more significant; this will change the Rosseland mean opacity with repercussions for energy transport calculations. This spectral region corresponds to the onset of the  $L$  shell edge, and as suggested previously problems with the position of the continuum in IMP would cause a shift in the position of the edge relative to absorption lines.

If this were the cause of the problems seen in figure 6.6(a), then the required shift in the position of the

(a)  $T = 30 \text{ eV}$ ,  $\rho = 0.028 \text{ g/cc}$ (b)  $T = 41 \text{ eV}$ ,  $\rho = 0.025 \text{ g/cc}$ 

**Figure 6.6:** The opacity of niobium calculated using the IMP code in the UTA approximation, for the conditions of the experiment of Hoarty et al.. We present data for two sets of plasma conditions, corrected for gradients in the sample, and converted to transmission.

continuum is consistent with that suggested by the average ionisation data presented in section 5.2. This is not consistent with a more detailed analysis however. The low density of this experiment gives an ion sphere radius of 1.1 nm which using the estimations given in Salzmänn's book [123] suggests that the effects of pressure ionisation will be small. Indeed, using the COWAN detailed atomic physics code [25] the average energy required to remove a 2p electron from the ground state of Nb IX (the average ionisation predicted by IMP) is 2555 eV; IMP calculations give this quantity as 2478 eV. Hence IMP gives ionisation transitions as too low in energy compared to more sophisticated models - the opposite to what is required to make calculations agree with experiment. The 40 eV shift that is required to align transition arrays only makes this situation worse.

In the higher temperature case, figure 6.6(b), the agreement with the average transmission is much better. The transition arrays are far too pronounced in this case however; the lineshapes shown include electron impact broadening which may be too small, however the low electron density makes this unlikely. Test calculations have confirmed that the electron impact width is negligible in both sets of data. It can also be seen that some features that appear in the calculation do not appear in the experimental data; this behaviour may be a signature of the breakdown of LTE in the sample, which given the larger temperature and lower density of this plasma would be more pronounced than in figure 6.6(a). In general, however, the opacity agrees reasonably well with experiment.

## 6.6 Discussion

In this section we aimed to formulate a method of converging opacity calculations without multiple runs, and without wasting calculation time by throwing away large numbers of transition lines. The analysis of the probability of configurations provides this scheme, and allows a systematic approach to the problem by grouping configurations with others that can be expected to have similar contributions to the opacity. The approach relies on the probability distribution in occupation number space being peaked enough to overcome changes in the number of configurations between points. The calculations that we have presented suggest that this is the case, even for calculations where the mean configuration has an almost-filled  $M$  shell. In fact the narrowing of the probability distribution as the temperature increases is able to counterbalance the

increasing number of electrons.

The conclusions may be different for a higher temperature plasma with many bound electrons; increasing the plasma  $Z$  will eventually lead to a broad enough probability distribution that the scheme given above will fail. Our test calculations for Nb ( $Z = 41$ ) have no problems and so it can be expected that the convergence approach will not fail until  $Z$  is very large. For elements of interest to civilian radiation-hydrodynamic simulations, solar modelling, and experiment, no problems will be encountered.

Development of an opacity code that automatically converges the partition function to a required level of accuracy would be straightforward. This can potentially save a significant amount of calculation time as other approaches to the convergence of the opacity can include large numbers of extra configurations.

The analysis of the Nb data at the end of this section is the culmination of the work presented in the first sections of this thesis. The data have shown that a generally good description of experiment can be achieved using the IMP code. The  $N$  shell problem presented by the data is on the limit of the capability of most opacity codes and the ability of IMP to describe such a system, which relies on the convergence procedure described, is very encouraging. It should be noted, though, that the Nb data analysed is a fortuitous case as the average population of the  $N$  shell is low. In cases where the population is close to half-full the number of configurations will be very large and significant runtime will be required even though we use a very fast model.

The experimental data have demonstrated two potential problems with the IMP's approach. The first is the exchange potential in our HFS calculations, for which the LDA is used. As discussed in section 3.3, this is a known problem that can be solved through the use of a more complex atomic model. In applications where very fast calculations are required, work to find a simpler solution is required. The second problem is the poor description of transmission windows in the lower temperature case. We have shown that this is unlikely to be due to problems with continuum lowering; recent work by Hansen *et al.*[124] has shown that an improved description of the transmission window can be found by including a model for the broadening of the ionisation edge due to the width of the initial configuration. Such effects are not included in IMP calculations and so this may explain the discrepancy.

## 7 The Effect of UTAs on Opacity Calculations

The UTA model as described in section 3.4 is an extremely useful approximation that allows large savings in calculation time. As such it has seen continual development since it was first proposed in 1979 [125]. These improvements address several deficiencies in the model however their motivation relies on the analysis of a small number of examples making it unclear how successful or important they are in full opacity calculations. In this section we present a more detailed analysis of the theory behind unresolved transition arrays and analyse the features of different models that are most important from the point of view of full opacity calculations.

### 7.1 Background

We begin by presenting the various UTA models that have been developed. Since these various models are all based on the same general approach to the problem, the first sections below will set out the theoretical basis of the UTA model.

#### 7.1.1 Statistical Description of sets of Absorption Lines

Unresolved transition arrays are used to describe sets of absorption lines as a single continuous form; we therefore begin our analysis by summing the absorption profiles of each component line  $l$  explicitly,

$$\begin{aligned}\kappa_{UTA}(\epsilon) &= \sum_{l \in UTA} \kappa_l(\epsilon) , \\ &= \frac{8\pi^2}{3cph^2} \epsilon \left(1 - e^{-\frac{\epsilon}{k_B T}}\right) \sum_{l \in UTA} \frac{n_{i,l}}{g_{i,l}} S_l \phi_l(\epsilon) .\end{aligned}\tag{7.1.1}$$

where  $S_l$  and  $\phi_l(\epsilon)$  are the strengths and profiles of the component lines as previously described, and  $n_{i,l}$  and  $g_{i,l}$  are the number density and degeneracies of the initial level of the  $l^{\text{th}}$  line respectively. The UTA model as originally described then invokes two approximations;

1. Statistical Weight Approximation -

Here the variation in energy of the initial levels of all the lines in a UTA is assumed to be small

compared to  $k_B T$ , making the number density of initial ion levels

$$n_{i,l} = \frac{g_{i,l} e^{-\frac{E_{i,l}}{k_B T}}}{\Omega} \simeq \frac{e^{-\frac{\bar{E}_l}{k_B T}}}{\Omega} g_{i,l} ,$$

where  $\bar{E}_l$  is the centre of gravity of the lower ion levels and  $\Omega$  is the partition function. Since the Boltzmann factor is now constant for all lines in the UTA this approximation assumes that initial ion levels are populated according to their statistical weights.

## 2. Average Lineshape -

Each component line is assigned the same lineshape, shifted to be centred on the transition energy of a given component. This is then written as a convolution;

$$\phi_l(\epsilon) \simeq \phi(\epsilon - \epsilon_l) = \int_{-\infty}^{\infty} \phi(\tau) \delta(\epsilon - \epsilon_l - \tau) d\tau .$$

It should be noted that in this case the lineshape function  $\phi(\epsilon)$ , which describes all line broadening processes, is replaced by the average lineshape of all component level→level transition lines. DCA opacity codes can calculate this lineshape function using the properties of the configuration→configuration transition in question.

Using the above approximations we can rewrite equation (7.1.1) as

$$\kappa_{UTA}(\epsilon) = \frac{8\pi^2}{3c\rho h^2} \epsilon \left(1 - e^{-\frac{\epsilon}{k_B T}}\right) \frac{e^{-\frac{\bar{E}_i}{k_B T}}}{\Omega} \int_{-\infty}^{\infty} \phi(\tau) \sum_{l \in UTA} S_l \delta(\epsilon - \epsilon_l - \tau) d\tau , \quad (7.1.2)$$

$$= \frac{8\pi^2}{3c\rho h^2} \epsilon \left(1 - e^{-\frac{\epsilon}{k_B T}}\right) \frac{e^{-\frac{\bar{E}_i}{k_B T}}}{\Omega} \int_{-\infty}^{\infty} \phi(\tau) \left[ \int_0^{\infty} S \left\{ \sum_{l \in UTA} \delta(S - S_l) \delta(\epsilon - \epsilon_l - \tau) \right\} dS \right] d\tau , \quad (7.1.3)$$

where the factor inside curly brackets (without the integration variable  $\tau$ ) can be identified as the joint distribution of component lines in energy and strength  $D(\epsilon, S)$ . Then the integral term is the total strength

contained in component lines of given energy,  $S(\epsilon)$ , and the UTA absorption profile becomes

$$\begin{aligned}\kappa_{UTA}(\epsilon) &= \frac{8\pi^2}{3c\hbar^2} \frac{e^{-\frac{\bar{E}_i}{k_B T}}}{Z} \epsilon \left(1 - e^{-\frac{\epsilon}{k_B T}}\right) \int_0^\infty \phi(\tau) S(\epsilon - \tau) d\tau, \\ &\equiv \frac{8\pi^2}{3c\hbar^2} \frac{e^{-\frac{\bar{E}_i}{k_B T}}}{Z} \epsilon \left(1 - e^{-\frac{\epsilon}{k_B T}}\right) [S \otimes \phi](\epsilon),\end{aligned}\tag{7.1.4}$$

where  $S(\epsilon)$  is the total strength as a function of photon energy,

$$S(\epsilon) \equiv \int_0^\infty SD(\epsilon, S) dS, \tag{7.1.5}$$

and  $[S \otimes \phi](\epsilon)$  denotes the convolution of the strength and lineshape profiles.

The opacity profile due to a group of lines is found by determining the total strength due to all lines in the group as a function of energy  $S(\epsilon)$  and convolving with the individual transition lineshape. The true distribution of strengths is a train of  $\delta$ -functions; the UTA model consists of approximating this using a continuous joint distribution function  $D_c(\epsilon, S)$ . An example of this can be seen in figure 7.1 where the detailed strength profile of the  $[\text{Li}]:2p^3 3p 3d^2 \rightarrow 2p^2 3p 3d^3$  transition in iron, convolved with a Gaussian lineshape is shown for varying line widths. We also show the approximate continuous distribution of term lines, found by summing the total strength in small energy bins. It can be seen that as the line width gets wider, making the array less resolved, the actual lineshape approaches the continuous distribution of strengths.

The problem of finding the distribution function  $D_c$  will be considered in the following sections; at this stage the method used to form the absorption profile  $\kappa_{UTA}$  are discussed. These are the UTA and RTA models as introduced previously. In the UTA model [125, 126, 80], component lines are expected to be sufficiently closely packed that the distribution function itself provides a good description of the train of  $\delta$ -functions. This approximation is aided by the fact that it is the convolution  $[S \otimes \phi](\epsilon)$  that must be well described; the resulting smoothing of the detailed distribution function allows a good description provided the spacing between component lines is small compared to their width. This is the regime shown by the widest lineshape case in figure 7.1; the accuracy of such an approach depends on the ‘porosity’ of the line,

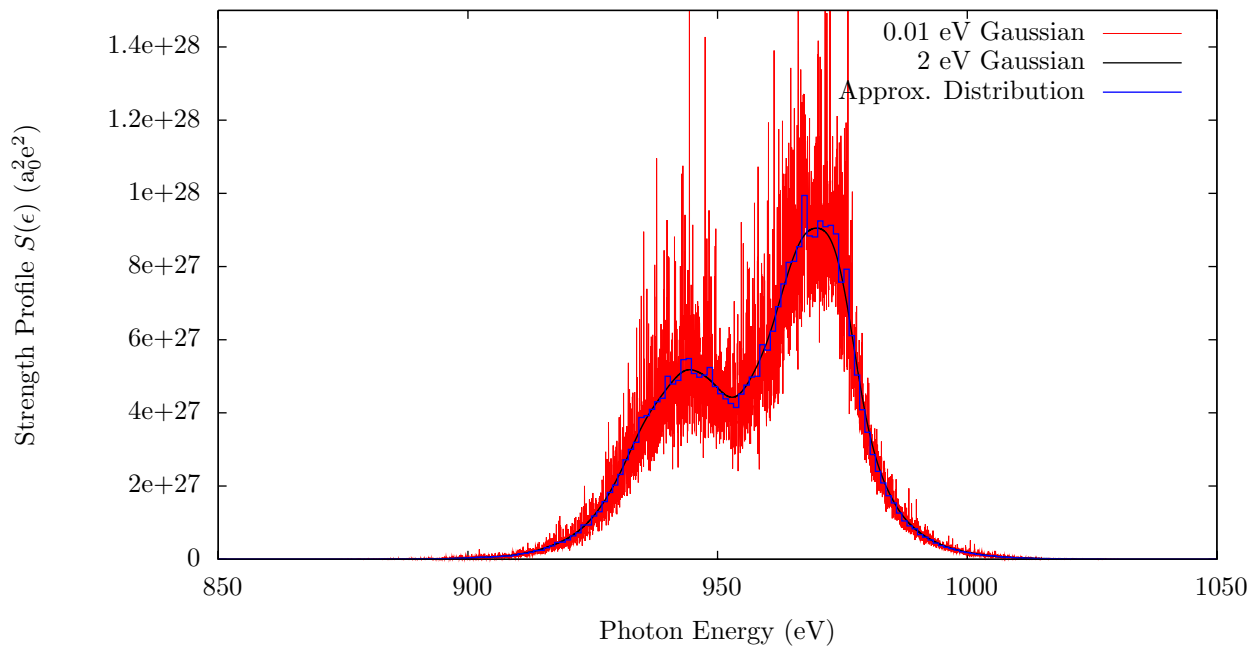


**Figure 7.1:** *The detailed strength profile of the  $[Li]:2p^33p3d^2 \rightarrow 2p^23p3d^3$  transition in iron with Gaussian lineshapes of varying width, compared with the approximate statistical description of strengths. It can be seen that the two descriptions agree with the line width is large enough to smooth out individual term lines.*

and in later sections we will attempt to quantify this and include it in our analysis.

The second approach to the formation of the UTA absorption profile allows the model to be applied to significantly more porous lines by taking random samples from the known distribution and adding them to the absorption profile explicitly. Such an approach is known as the random transition array (RTA) model [84, 83, 85], as described in section 5.3. In effect the detailed distribution of term lines is generated using a Monte-Carlo analysis, which allows the full absorption profile to be determined in detail by assigning each line an individual probability and lineshape and using (7.1.1). Since lines are added individually the RTA can describe transition arrays which are very porous provided a good description of the distribution function can be found and the desired result of calculations does not depend too much on the exact positions and strengths of detailed lines. This first requirement will be tested in the following sections; the second can be tested in the usual way by averaging several calculations using different random number generators or seeds.

The UTA and RTA models as discussed above have both assumed that the joint distribution function of component line energies and strengths is known. The explicit calculation of  $D_c(\epsilon, S)$  is not trivial however the



general approach to the problem is well defined. In the following subsection we will describe this approach and analyse the approximations that must be made from the point of view of the plasma opacity.

### 7.1.2 Finding the Distribution of Component Lines in a UTA

The determination of statistical distributions from a set of samples is a core problem in experimental science, and we adopt the same approach to the problem here. The method is based on the assumption that the moments of a set of samples are estimators of the moments of the distribution they are taken from; knowledge of the distribution moments then allow the distribution to be found unambiguously. Our problem then reduces to that of finding the moments of the lines in an array.

In equation (7.1.4) we showed that the form of the UTA opacity profile is determined by the form of the line strength as a function of energy and so we calculate the energy moments of this quantity,

$$\alpha_S^{(n)} = \frac{1}{S_{TOT}} \int_{-\infty}^{\infty} (\epsilon - \bar{\epsilon})^n S(\epsilon) d\epsilon = \frac{1}{S_{TOT}} \iint_{-\infty}^{\infty} S(\epsilon - \bar{\epsilon})^n D(\epsilon, S) d\epsilon dS, \quad (7.1.6)$$

in both the detailed and continuous representations and require them to be equal;

$$\sum_{l \in UTA} S_l (\epsilon_l - \bar{\epsilon})^n \equiv \iint_{-\infty}^{\infty} (\epsilon - \bar{\epsilon})^n S D_c(\epsilon, S) d\epsilon dS. \quad (7.1.7)$$

Equation (7.1.7) then expresses the requirement that the continuous approximation correctly reproduces the total strength ( $n = 0$ ), position ( $n = 1$ ), width ( $n = 2$ ) and higher moments of the transition array. The best approximation will be found by choosing  $D_c$  such that equation (7.1.7) is true for as many  $n$  as possible; in the limit where it is true for all  $n$  then  $D_c$  gives an exact description.

In reality it is not possible to calculate the infinite number of sample raw moments, nor is it computationally efficient. The aim of the UTA model is to determine only the most important distribution moments exactly and to approximate the remaining moments by assuming a functional form for the continuous distribution function  $D_c$ . We are then faced with the task of calculating the most important moments, and of choosing the best functional form that allows their inclusion. The 0<sup>th</sup> order moment, the total strength, can be found from DCA calculations. The 1<sup>st</sup> order moment gives the position of the UTA in energy and can be

calculated approximately as the difference between the mean energies of the upper and lower configurations. This approach effectively neglects the strength weighting in equation (7.1.6), an approximation that can be corrected using more formulae calculated from first principles. The highest order moment that can currently be calculated in closed form is the 2<sup>nd</sup>, which gives the width of the transition array [125, 126]. Some higher order moments can be calculated in special cases however no general expressions exist; in practice they must be fixed by some approximate continuous function. The best function to use will then be the one whose high order moments best match the correct values.

Before the choices of continuous function are discussed, we briefly consider the effect of approximated moments on the absorption profile. In order to obtain an accurate description of the opacity it is necessary to describe the moments of  $\kappa(\epsilon)$  correctly, not just the moments of  $S(\epsilon)$ , and the relation between the two (7.1.4) introduces other energy dependant factors. We begin by analysing the effect of the convolution with  $\phi(\epsilon)$  by considering

$$\alpha_{S \otimes \phi}^{(n)} = \frac{1}{S_{TOT}} \int_0^\infty (\epsilon - \bar{\epsilon})^n [S \otimes \phi](\epsilon) d\epsilon .$$

where we expect that the effect of the convolution is to cause a mixing of the moments of the strength distribution and the line profile. Writing out the convolution, Taylor expanding and integrating term by term gives the result

$$\alpha_{S \otimes \phi}^{(n)} = \sum_{k=0}^n \binom{n}{k} \alpha_S^{(n-k)} \alpha_\phi^{(k)} ,$$

which describes the expected mixing. In the above the prefactor is a binomial coefficient, and the moment of the lineshape  $\phi$  is taken about zero. This expression describes mixing of distribution moments via the convolution with the energy dependant lineshape; however the  $n^{\text{th}}$  moment of the convolution only contains moments of  $S$  and  $\phi$  of  $n^{\text{th}}$  order and lower. Then if a given UTA model calculates all moments up to a given order correctly then the moments of the convolution will be correct to the same order. Our analysis is not complete however, as we have still neglected the other prefactors in the opacity expression. One of these is an exponential which can be expected to cause a mixing between all moments. In this case the relevant

moments are

$$\begin{aligned}
\alpha_{\kappa}^{(n)} &\propto \int_0^{\infty} (\epsilon - \bar{\epsilon})^n \epsilon \left(1 - e^{-\frac{\epsilon}{k_B T}}\right) (S \otimes \phi)(\epsilon) d\epsilon, \\
&= \bar{\epsilon} \left(1 - e^{-\frac{\bar{\epsilon}}{k_B T}}\right) \alpha_{S \otimes \phi}^{(n)} + \left(1 - e^{-\frac{\bar{\epsilon}}{k_B T}} \left(1 - \frac{\bar{\epsilon}}{k_B T}\right)\right) \alpha_{S \otimes \phi}^{(n+1)} \\
&\quad - e^{-\frac{\bar{\epsilon}}{k_B T}} \sum_{m=2}^{\infty} \left(\frac{1}{k_B T}\right)^m \frac{(-1)^m}{m!} (\bar{\epsilon} - m k_B T) \alpha_{S \otimes \phi}^{(n+m)}, \quad (7.1.8)
\end{aligned}$$

The above expression makes clear the effect of the infinite order of the exponential factor; the  $n^{\text{th}}$  moment of the opacity profile now depends on all moments of the strength and line profiles, therefore errors in the high order behaviour of an approximate functional form can lead to changes in the lower order moments of the opacity. The mixing is strongest in arrays of low energy, and between a given moment and its next higher; therefore the line position is effected most strongly by errors in its width, and line widths are effected by asymmetry, and so on. An example is shown in figure 7.2 where we show the opacity profile arising from the  $3d^5 4s^2 4p \rightarrow 3d^4 4s^2 4p^2$  transition in iron. This array contains 40,664 component lines. In the figure we show the results of a detailed calculation along with the opacity modelled using a Gaussian strength distribution. The two Gaussian distributions differ only in their widths, the narrower having the correct value and the wider having a variance equal to 4 times the correct value (a value which we show later to be consistent with the errors in fast width calculations). It can be seen that although the strength distributions are forced to have the same mean, the absorption feature with the incorrect width is shifted significantly as a result of the mixing between 1<sup>st</sup> and 2<sup>nd</sup> order moments. This mixing has not been included in any previous work, and so will be included implicitly in this thesis by ensuring all energy dependant factors are included in our investigations. It should also be noted that this mixing is symmetric between the moments of the strength and line profiles; therefore inaccuracies in the description of line broadening in a calculation will also mix into the observed transition array shape. More significantly a measurement of transition array width does not directly give the line profile width.

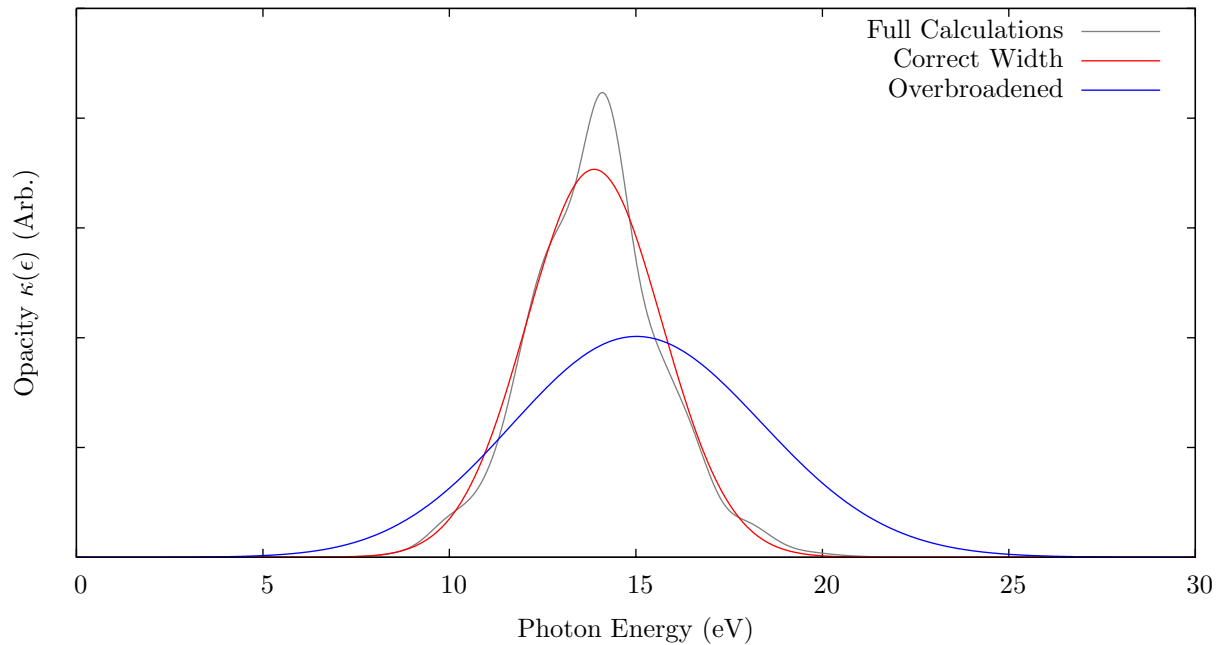


**Figure 7.2:** *The effect of an error in the moments of a transition array on the opacity profile. Two Gaussian models for the strength distribution of the  $3d^5 4s^2 4p \rightarrow 3d^4 4s^2 4p^2$  transition array in iron are plotted, one with the correct width and one with the width multiplied by 4. It can be seen that the change in the width results in not only the expected overbroadening, but also a shift in the line position. This shift is a consequence of the energy dependant factors in the definition of the opacity.*

### 7.1.3 Functional Forms for the Term Line Distribution

The higher order moments of the strength distribution  $S(\epsilon)$  are fixed by the choice of functional form, and these unspecified moments are mixed into lower order moments through the stimulated emission correction and other energy dependant factors. It is therefore important to use a functional form that describes the actual shape of the distribution as closely as possible, and this problem has been the focus of the majority of the more recent work on UTA models. The different functions that have been suggested are motivated by mathematical convenience as much as by physical reasoning, and so it is of interest to test how important the differences in the models are with respect to the plasma opacity. We begin by presenting the existing models in order of sophistication.

It has already been mentioned that the current state of the art allows the calculation of the total strength, mean energy, and width of the strength profile  $S(\epsilon)$  from first principles for any configuration. UTA models began, therefore, with the use of a Gaussian description of the relevant distribution which is both intuitive

and convenient since the convolution with the lineshape  $\phi(\epsilon)$  can be performed very easily for broadening models of relevance to opacity calculations. The question of correlations between the coordinates  $\epsilon$  and  $S$  then allowed a modified shape to be derived which in effect has a modified 4<sup>th</sup> order moment, or kurtosis. More recently the same lower order moments have been included using other functional forms in an attempt to better describe the even higher order moments of the strength profile.

#### 7.1.4 Uncorrelated Models

The simplest description of a UTA can be found by assuming that the energies and strengths of term lines are independent. In this case  $D(\epsilon, S) \equiv D_\epsilon(\epsilon)D_S(S)$  and the absorption profile becomes

$$\kappa_{UTA}(\epsilon) = \frac{8\pi^2}{3c\rho h^2} \frac{e^{-\frac{E_i}{k_B T}}}{Z} \epsilon \left(1 - e^{-\frac{\epsilon}{k_B T}}\right) S_{TOT} [D_\epsilon(\epsilon) \otimes \phi(\epsilon)] , \quad (7.1.9)$$

and the moments of the partial distribution  $D_\epsilon$  are calculated without the strength weighting, significantly reducing the calculation time required. In the above equation  $S_{TOT}$  is the total strength due to all lines in the array. In IMP calculations the partial energy distribution is assumed to be Gaussian and the convolution is performed analytically. Test calculations have suggested that the neglect of correlations between line energy and strength is not valid and so all more advanced models include these in some way. In later sections a large number of arrays are tested for the presence of these correlations.

#### 7.1.5 Models Including Correlation Between $S$ and $\epsilon$

The simplest method of including correlations is to approximate the form of the strength profile  $S(\epsilon)$  rather than the distribution function  $D(\epsilon, S)$ . In this case the moments that are included in any approximate form must be weighted by the line strength as in equation (7.1.6); correlations are then included explicitly. As mentioned these strength weighted moments can be calculated up to order 2 and so it is intuitive to use a Gaussian model.

The model described above should certainly give an improved description over the uncorrelated models, however the selection of a Gaussian lineshape is still made on the basis of mathematical convenience. A

more physical lineshape has been proposed that makes use of detailed atomic calculations to analyse the exact form of the correlation between line strengths and energies. The line energies are assumed to be Gaussian distributed, as are the line amplitudes  $a = \sqrt{S}$ . This second assumption is taken from work on nuclear transition widths and random matrices [127]. Correlations are introduced by allowing the width of the amplitude distribution to vary with energy;

$$D(\epsilon, a) = \frac{1}{\sqrt{2\pi}\sigma_\epsilon} e^{-\frac{(\epsilon-\bar{\epsilon})^2}{2\sigma_\epsilon^2}} \frac{1}{\sqrt{2\pi}\sigma_a(\epsilon)} e^{-\frac{a^2}{2\sigma_a^2(\epsilon)}} , \quad (7.1.10)$$

then

$$S(\epsilon) = \int_{-\infty}^{\infty} a^2 D(\epsilon, a) da = \frac{1}{\sqrt{2\pi}\sigma_\epsilon} e^{-\frac{(\epsilon-\bar{\epsilon})^2}{2\sigma_\epsilon^2}} \sigma_a^2(\epsilon) . \quad (7.1.11)$$

The variation of  $\sigma_a(\epsilon)$  with energy allows an increased probability of large amplitude lines in certain regions of the UTA (where  $\sigma_a$  is largest). This increase in strong lines leads to a modification of the strength distribution by  $\sigma_a^2(\epsilon)$ ; at this stage this is arbitrary and can describe the effects of correlations in any way. A good example has been given previously in figure 7.1, where the transition array splits into two separate peaks due to the spin-orbit interaction. In this case a double peaked  $\sigma_a(\epsilon)$  is required.

In the original investigation, detailed calculations of two transition arrays were used to find the functional form of  $\sigma_a(\epsilon)$  [84]. On that basis those authors suggested that the standard deviation decreases exponentially from the line centre, making larger lines more probable at line centre and therefore reproducing the expected line narrowing effect. Putting

$$\sigma_a(\epsilon) = e^{\alpha + \beta|\epsilon - \bar{\epsilon}|} , \quad (7.1.12)$$

the parameters of the fit can be determined from the moments of the transition array. The correlation is quantified by comparing the width of the energy distribution,  $\sigma_\epsilon$ , with the standard deviation of the strength distribution  $\sigma_S \equiv \sqrt{\alpha_S^{(2)}/S_{TOT}}$ ; for set of lines with no correlation these will be equal. Substituting (7.1.12) into equation (7.1.11) and calculating the energy variance results in one expression, which combined with the normalisation condition for (7.1.11) allows the two parameters to be defined in terms of the total strength in the line, and a parameter  $X$  that quantifies the degree of correlation. This correlation parameter is the

solution of the equation

$$[\rho - X^2 - 1] e^{\frac{X^2}{2}} \left( 1 + \operatorname{erf} \left( \frac{X}{\sqrt{2}} \right) \right) + \sqrt{\frac{2}{\pi}} X = 0 , \quad (7.1.13)$$

where  $\rho$  is the ratio of the variances ( $n = 2$ ) of  $S(\epsilon)$  with and without correlations,

$$\rho = \frac{\alpha_S^{(2)}}{\sigma_\epsilon^2} . \quad (7.1.14)$$

For uncorrelated lines this is equal to 1 and  $X = 0$ . For lines that are strongly narrowed by correlations  $\rho \rightarrow 0$  and  $X \rightarrow \infty$ ; in the opposite case  $X$  is negative. The parameters  $\alpha$  and  $\beta$  are convenient in describing the form of the correlation, however the UTA lineshape is simplest when written in terms of the correlation parameter  $X$ ,

$$S_B(\epsilon) = \frac{S_{TOT}}{\sqrt{2\pi}\sigma_\epsilon \left[ 1 + \operatorname{erf} \left( \frac{X}{\sqrt{2}} \right) \right]} e^{-\frac{1}{2\sigma_\epsilon^2} (|\epsilon - \bar{\epsilon}| - X\sigma_\epsilon)^2} . \quad (7.1.15)$$

In the above form  $S(\epsilon)$  is Gaussian in the absence of correlations and has a sharp peak for  $\rho < 1$ . When lines are broadened by correlations ( $\rho > 1$ ) then the lineshape has two peaks and the model is not appropriate.

It is clear from the above expressions that the modified line profile now requires both  $\sigma_S^{(2)}$  and  $\sigma_\epsilon^2$  as input, and the extra input parameter effectively fixes a higher order moment of the distribution. Since the lineshape is symmetric, we will investigate this by calculating the next highest even order moment, the kurtosis. In this case we have

$$\alpha_S^{(4)} = \frac{(\alpha_S^{(2)})^2}{\rho^2} [\rho(X^2 + 5) - 2] , \quad (7.1.16)$$

which reduces to the Gaussian value of  $3(\alpha_S^{(2)})^2$  for uncorrelated lines. It can be seen that the effect of a more detailed treatment of correlations is to modify the kurtosis, or the weight of the line wings, of the strength distribution. The model of correlations chosen here has allowed the kurtosis, which cannot be found from first principles, to be written in terms of two quantities which can. The details of the modification are, however, determined by the form of the correlation (7.1.12) and therefore are model dependant. The

log-linear model given by equation (7.1.12) worked well for the two example arrays in the original work, however we have already seen that in the case of spin-orbit split arrays such a single peaked correlation function will not suffice. We will therefore directly test this model by comparing the kurtosis predicted by the above expression with the value found from detailed calculations. This can be used to give a more robust analysis of opacity calculations than was originally presented.

### 7.1.6 Modifications for Higher ( $> 2^{\text{nd}}$ ) order moments

The previous model allows an approximate description of the kurtosis of transition arrays based on a model for correlations between  $S$  and  $\epsilon$ . If, on the other hand, the kurtosis can be calculated from first principles then this is not necessary; this moment can be included explicitly in  $S(\epsilon)$  through some expansion. This approach has the advantages that the convolution with other lineshapes may become easier to compute, and that no assumptions are made about the form of the correlation. These are offset by the fact that in many cases the higher order moments may not be known, since it is not currently possible to calculate them directly. One application where this approach is still usefull is calculations based on atomic databases - in this case it can be more efficient to store the moments of a transition array than the details of all component lines. For this reason it is still of interest to include these models in our investigation.

The first modified distribution function proposed was the Gram-Charlier (GC) expansion, which modifies a Gaussian lineshape with a polynomial function to give the desired higher order moments. This can be extended to arbitrary order however in this work we will focus on the effect of orders up to  $4^{\text{th}}$  in which case the GC expansion is

$$S_{GC}(\epsilon) = \frac{1}{\sqrt{2\pi\alpha_S^{(2)}}} e^{-\frac{(\epsilon-\bar{\epsilon})^2}{2\alpha_S^{(2)}}} F\left(\frac{\epsilon-\bar{\epsilon}}{\sqrt{\alpha_S^{(2)}}}\right),$$

$$F(y) = 1 + \frac{1}{3!} \frac{\alpha_S^{(3)}}{(\alpha_S^{(2)})^{3/2}} (y^3 - 3y) + \frac{1}{4!} \left( \frac{\alpha_S^{(4)}}{(\alpha_S^{(2)})^2} - 3 \right) (y^4 - 6y^2 + 3) .$$

The GC expansion will be usefull in the following analysis as it allows the two extra moments, the skew and kurtosis, to be treated independently. It has been pointed out that the GC expansion runs into problems for large values of the skew or kurtosis, in which case it may go negative in the wings of the profile [82].



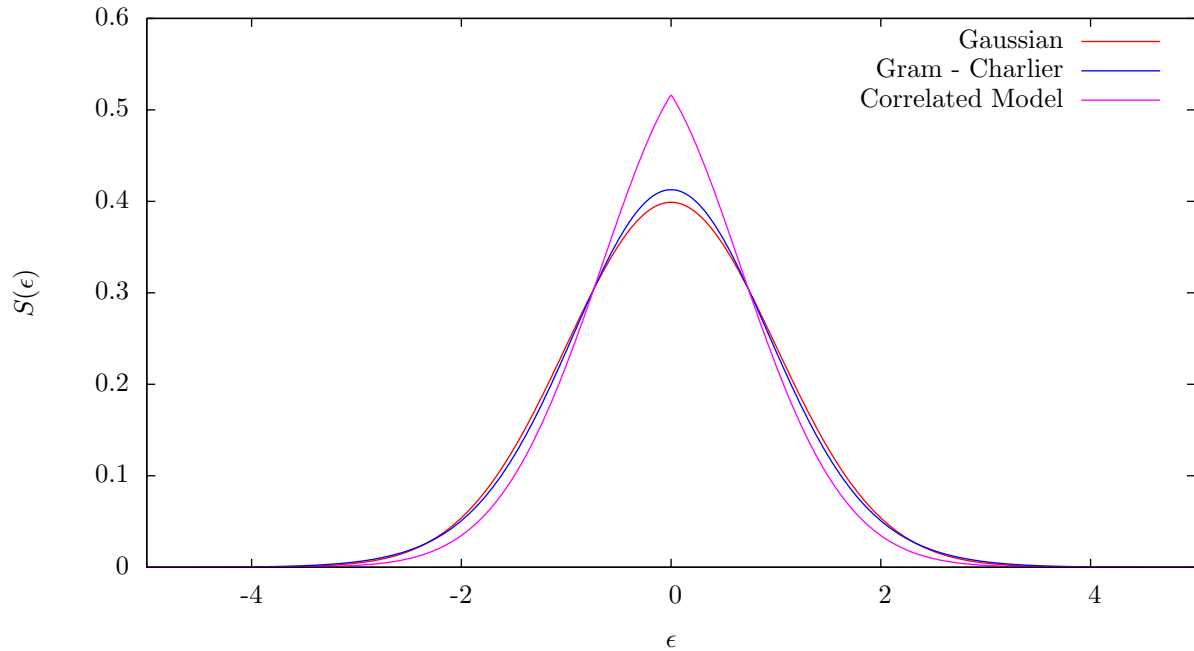


**Figure 7.3:** A comparison of the strength distributions implied by various high order UTA models. The Gaussian model for the strength distribution is shown in red, along with the 4<sup>th</sup> order Gram-Charlier expansion in blue and the Correlated model due to Bauche et al. in purple. The case shown is for a symmetric line of kurtosis  $\alpha_S^{(4)} = 3.3(\alpha_S^{(2)})^2$  which implies a correlation described by  $\rho = 0.75$ . It can be seen that there are significant differences in the models even when moments up to the 4<sup>th</sup> are identical.

In the same work Pain *et al.* suggest two alternative models, the normal inverse Gaussian (NIG) and the generalised Gaussian (GG), and suggest that they give an improved fit to a series of frequency resolved opacity profiles. These alternatives contain parameters that can be varied to give the required values of one of the higher moments (the skew for the NIG, and the kurtosis for the GG) however the other moment cannot be changed. The GC expansion is more versatile, and the evidence for the other functional forms is not conclusive, and for these reasons we will concentrate our work on the GC expansion.

The various UTA models described above give an appreciable change in the form of the strength distribution, even though they are defined to have a (small) set of common moments. The differences introduced by the moments that are not the same can be seen in figure 7.3 where we plot the Gaussian, Correlated and Gram-Charlier lineshapes for a symmetric distribution of kurtosis  $\alpha_S^{(4)} = 3.3(\alpha_S^{(2)})^2$  ( $\rho = 0.75$ ). It can be seen that there is a large difference between the profiles at line centre, the correlated model giving a significantly narrower line. If the analysis that leads to this shape proves to be applicable to a general transition array

then this simple comparison implies that other, simpler approaches will not be appropriate.

### 7.1.7 First Principles Distribution Functions

The distribution of term lines in energy and amplitude is closely related to the properties of the Hamiltonian matrix, and has seen extensive research from several directions. Mathematical approaches based on random matrix theory have been applied extensively to the related problem of nuclear reaction widths [127], and the models described previously have motivated other analytic approaches. These works have resulted in some hypotheses and simplified results but no general results.

Although the results we will present in the following sections are for the most general intermediate coupling case, the problems that analytic work faces can be understood from simplified pure coupling models. In this section we will present a brief analysis of the problem using a simple cartoon of the energy level structure, and later with some well known results for the  $LS$  coupled system.

The effect of term splitting can be seen by considering the cartoon in figure 7.4. We consider a pair of configurations, or subsets of a configuration, to be split according to the the total angular momentum of each level. The splitting between the separate states is given by the  $\Delta_i^{(j)} \equiv E_{J_{i+1}^{(j)}} - E_{J_i^{(j)}}$  parameters. The values of  $J_i$  are drawn ordered with increasing angular momenta however by changing the relative size and sign of the  $\Delta_i$  quantities the energies need not be ordered. The analysis of the distribution of term lines then requires the analysis of this figure.

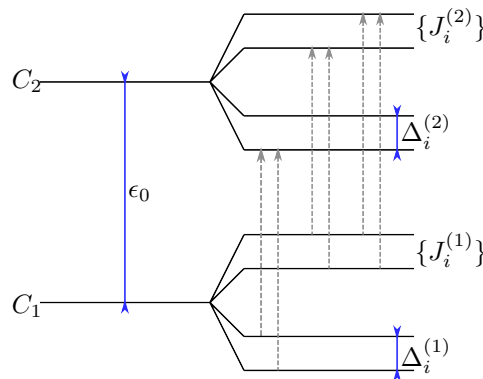


**Figure 7.4:** Cartoon of the model used to describe the distribution of term lines from first principles. The upper and lower configurations are assumed to split according to the total angular momenta of each term  $J$ ; the energy splitting between in the  $i^{\text{th}}$  and  $(i+1)^{\text{th}}$  state is given by  $\Delta_i$ .

To begin with we consider the energies of transitions only, and assume that the lowest values of  $J$  are the same in the upper and lower configuration. There are three sets of transitions according to the  $\Delta J = -1, 0, 1$  selection rule, which in this case have energies given by

$$\{\epsilon_k\}_{12} = \begin{cases} \left\{ \epsilon_0 + \sum_{l=0}^{k-1} (\Delta_l^{(2)} - \Delta_l^{(1)}) \right\} & \text{when } \Delta J = 0 \\ \left\{ \epsilon_0 + \sum_{l=0}^{k-1} (\Delta_l^{(2)} - \Delta_l^{(1)}) + \Delta_k^{(2)} \right\} & \text{when } \Delta J = 1 \\ \left\{ \epsilon_0 + \sum_{l=0}^{k-1} (\Delta_l^{(2)} - \Delta_l^{(1)}) - \Delta_{k-1}^{(2)} \right\} & \text{when } \Delta J = -1 \end{cases} , \quad (7.1.17)$$

where the value of  $k$  generates all allowed level to level configurations. This result can be understood by considering some special cases. In the case where all the level splittings are equal ( $\{\Delta_l^{(j)}\} = \Delta$ ) the transitions arising from each selection rule are degenerate and so there are three narrow structures, separated by  $\Delta$ , corresponding to each value of  $\Delta J$ . If, on the other hand, the level splittings are constant within the upper and lower arrays but not the same, the 3 separate structures acquire a width related to the difference in spin orbit splitting of the upper and lower configurations. This behaviour is the origin of the array splitting seen in figure 7.1. Clearly details of the level splitting are required to describe the detailed shape of transition arrays.

In the case of near- $LS$  coupling, the above results can be combined with some well-known results from atomic physics to further analyse the problem. We begin with the Landé Interval Rule [25];

$$E_{LSJ} - E_{LS,J-1} = J\zeta_{LS} , \quad (7.1.18)$$

which allows simplification of the previous result by relating the various  $\Delta_i$  to the value of  $J$ . In equation (7.1.18)  $\zeta_{LS}$  is an effective spin orbit splitting for the  $LS$  terms of the configuration. Substituting this into our general result and passing to a continuous representation allows the energy gap between transitions arising from a given  $LS \rightarrow L'S'$  subarray to be found. This is the inverse of the line distribution, and so our

model gives (in terms of the transition energy  $\epsilon$ , spin orbit parameters  $\zeta$ , and angular momenta)

$$\begin{aligned}
 D_\epsilon(\epsilon) &\equiv \frac{dN}{d\epsilon} = C + \sqrt{B^2 - 4C(A - \epsilon)} ; \\
 A &= \epsilon_0 - \zeta_{L'S'} \left[ 2J_0^{LS} - J_0^{L'S'} - \frac{1}{2} \right] + \zeta_{LS} J_0^{LS} + \zeta_{L'S'} \left[ J_0^{LS} - \frac{1}{2} \right] \Delta J + \frac{\zeta_{L'S'}}{2} (\Delta J)^2 , \\
 B &= (\zeta_{L'S'} - \zeta_{LS}) \left[ J_0^{LS} - \frac{1}{2} \right] + \zeta_{L'S'} \Delta J , \\
 C &= \frac{1}{2} [\zeta_{L'S'} - \zeta_{LS}] .
 \end{aligned} \tag{7.1.19}$$

In the above equations the  $J_0$  are the lowest values of total angular momenta in the two  $LS$  terms, and the transition energy runs between  $\epsilon_{min} = A + B + C$  and  $\epsilon_{max} = A + BN + CN^2$ . It can be seen that the  $A$  coefficient acts to shift the energies of lines arising with different values of  $\Delta J$ , and that the magnitude of the shift is dependant on the magnitude of the spin orbit parameter in the upper terms. This is in agreement with more detailed analysis of the problem, and is visible in spectra when this spin orbit splitting is large. It should be noted, however, that this analysis predicts a  $\sqrt{\epsilon}$  dependence for the energy distribution; this does not agree with the Gaussian assumption made in most UTA models. In order to more fully analyse the problem, the relative strengths of each line should also be included.

In  $LS$ -coupling simple results for the relative strengths of  $LSJ \rightarrow L'S'J'$  also exist. The expression for the matrix elements of the electric dipole operator in  $LS$ -coupling leads to the following expression

$$S_{LSJ \rightarrow L'S'J'} = \delta_{SS'} (2J+1)(2J'+1) \left\{ \begin{matrix} L' & S & J \\ J' & 1 & L' \end{matrix} \right\}^2 |\langle LS || \mathbf{er} || L'S' \rangle|^2 , \tag{7.1.20}$$

which gives the strength of a  $LSJ \rightarrow L'S'J'$  transition in terms of the reduced matrix element between the two  $LS$  terms and a  $6j$  symbol. This can then be combined with the previous results to model the strength distribution between the two subsets of levels. The  $6j$  symbol in equation (7.1.20) is largest when  $\Delta J = \Delta L$ , and so for a given  $LS \rightarrow L'S'$  transition the subarray with  $\Delta J = L' - L$  is largest; within this array the  $6j$  symbol increases with increasing  $J$ . Since the Landé rule predicts that these stronger transitions are more spaced out in energy, the net result (when individual lineshapes are included) is a pointed transition array.

Clearly there is a correlation between line energy and strength in this model; it arises since equations

(7.1.18) and (7.1.20) both refer to the position of the initial state in the lower configuration. The physical origin of this correlation is valid; close to LS coupling, states tend to be ordered according to their total angular momentum and the selection rule on  $J$  ensures that transitions occur between states at similar positions in the upper and lower configurations. It may appear, then, that this analysis can provide clues to the effects of correlations in terms of spin-orbit parameters.

There is a problem with this approach, however. The analysis given above cannot describe the complete distribution function required by UTA models since the Landé interval rule only applies to levels arising from a common  $LS$  term; as a result the distributions we have found are in terms of  $\epsilon_0$ , the splitting between the centres of gravity of the  $LS$  and  $L'S'$  sub-configurations. The same is true of the strength distribution due to its dependence on the reduced matrix element. The  $\epsilon_0$  quantities are dependant on the details of the configuration and electron wavefunctions in intermediate coupling and so must be found from detailed, configuration - resolved atomic models. Similarly, the above analysis can be performed in  $jj$ -coupling to give results for the lines arising from a given  $(jj) \rightarrow (jj)'$  transition; when attempting to find  $\epsilon_0$  in this case the same problems will arise. This is an unavoidable problem in cases where intermediate coupling is required, and so we must conclude that fast models require a more empirical approach.

## 7.2 Questions Regarding Unresolved Transition Arrays

The models that we have discussed all provide an approximation to the distribution  $D(\epsilon, S)$ , but differ in their assumptions regarding high order moments and correlations between  $\epsilon$  and  $S$ . These differences lead to noticeable changes in the UTA lineshape (see figure 7.3) however the models are rarely directly compared. Alongside this more sophisticated models such as Bauche *et al.*'s correlated model, Gram-Charlier expansion, *etc.* have been justified by only a small number of test calculations. In the remainder of this section we want to rectify this situation, with the aim of making clear which aspects of models are important, and which are not. Such a clarification should prove very useful in the development of opacity codes since these new models can be tailored to give the desired output accuracy.

The first assumption we aim to address is that of the presence of correlations between component line strengths and energies. Such correlations lead to a difference between the width of the joint distribution

$D(\epsilon, S)$  and of the strength profile  $S(\epsilon)$ ; we will exploit this to quantify the extent to which correlations occur. We will then move on to test the form for these correlations proposed by Bauche *et al.*. We have seen that the assumption of a functional form for  $\sigma_a(\epsilon)$  fixes the kurtosis of the UTA lineshape, and so a comparison of the model kurtosis with the true value tests the accuracy of the chosen function. Finally, we have also described models that explicitly include correlations by using strength-weighted moments and high-order modifications to the lineshape. We will also systematically test these.

A typical large opacity calculation may involve  $10^7 - 10^8$  transition arrays, the structure of which are determined by the details of the initial ion configuration, transition and coupling scheme in a very complex way. It is therefore important to test UTA models' ability to describe a large number of examples that represent as broad a range of conditions as possible. Such an approach lends itself very well to a statistical survey of a large number of transition arrays and it is this approach that we will adopt. The chosen set of transition arrays in our survey must then reflect the large range of different arrays that can occur; the most important properties to address can be summarised as

- Coupling Conditions -

In the previous section we showed that even under pure coupling conditions it is difficult to predict the properties of a general transition array. Although the faster opacity models we focus on this report usually do not resolve term structure, in order to make our results as general as possible our analysis will use detailed calculations performed in intermediate coupling.

- Array Porosity -

Lines of varying resolution will occur in the same opacity calculation and so the accuracy with which UTA models can deal with varying porosity is important

- Array Strength -

The strength of a given transition array compared to the local opacity due to other lines and absorption processes plays an important role in determining how the array contributes to the total opacity. This also determines which part of the lineshape is most important and can be used to test the accuracy of different regions of the lineshape

In the following sections we will develop an approach to the testing of UTA model that takes into account the above issues in a systematic way.

### 7.3 Testing UTA Models using Detailed Calculations

We aim to perform a statistical survey of transition arrays of relevance to opacity calculations, and to analyse them to determine the important features of opacity models. We must therefore begin by selecting a set of transitions to test.

Configurations are chosen to reflect the important configurations in the modelling of a typical plasma experiment. We choose iron for its importance to solar modelling, which has lead to several experimental studies; in particular we consider the experimental data of Nazir *et al.* [128], one of the first short pulse laser opacity experiments. This experiment collected emission data in the spectral range  $880 \rightarrow 1100$  eV, and although the plasma was not in LTE the high energy part of this range was well described in the original work by a plasma with  $T = 500$  eV and  $\rho = 8$  g/cc. We therefore form a set of configurations that are important to the modelling of this plasma.

Using the NIST atomic spectra database [129] a set of important configurations were built, resulting in around 50 UTAs of type  $1s^2 2s^2 2p^n 3s \rightarrow 1s^2 2s^2 2p^{n+1}$  and  $1s^2 2s^2 2p^n 3d \rightarrow 1s^2 2s^2 2p^{n+1}$  plus spectator configurations. A full simulation of these configurations requires a description of broadening transitions and so the calculation set was increased to include all possible electric dipole transitions out of the relevant ion configurations. This significantly increases the number of calculations to around 260 transition arrays. It is important to investigate the effects of array size on these statistical models and so some extra very large transition arrays were included, giving a full calculation set of 304 transition arrays.

These transitions are then passed to a detailed atomic physics code for analysis. In this study we use a pair of codes, GRASP2K [130] and the RNC/RCG codes due to Cowan [25] (hereafter referred to as COWAN), which perform all the coupling calculations and return the strengths and energies of each component line of a transition array. These lines are then sorted and grouped to form a set of non-relativistic UTA models. The resulting UTA energies and strengths are shown in figure 7.5. Two codes were used to ease problems with convergence, and in order to test that the two codes gave comparable results a set of tests were run

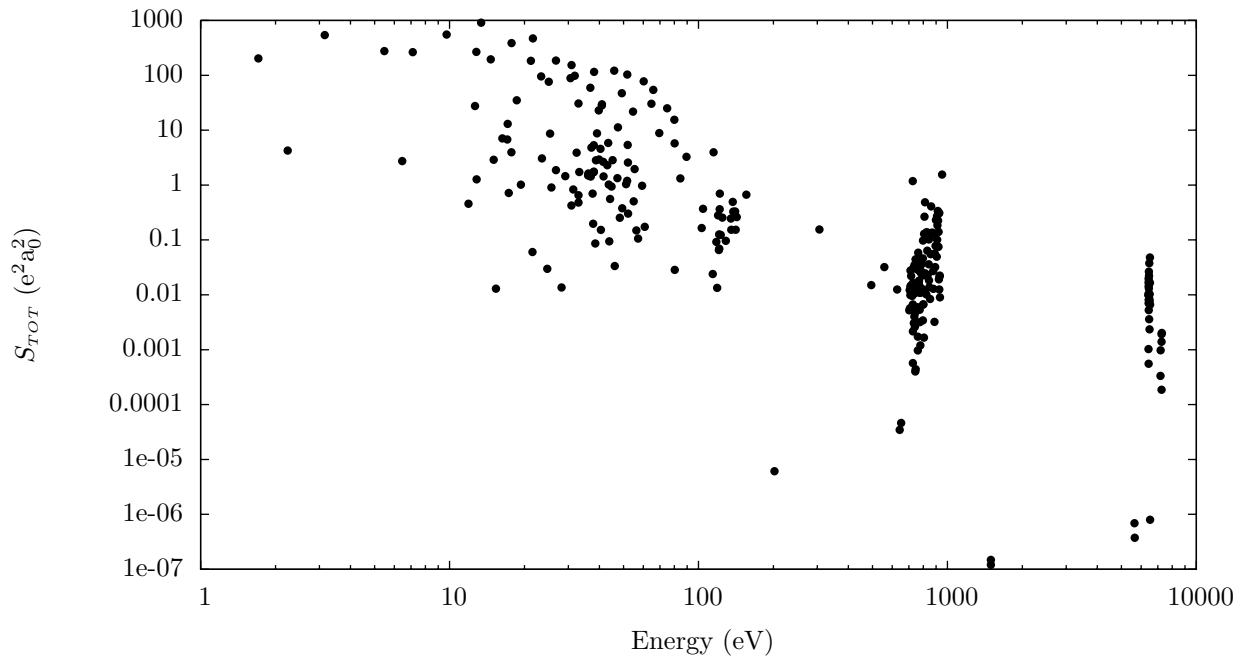


**Figure 7.5:** The details of the 304 unresolved transition arrays used in this study. We plot the total strength ( $e^2 a_0^2$ ) against the mean transition energy (eV).

where both codes were used to calculate the same transition array. An example of this is shown in figure 7.6 in which the strength profile of the  $[\text{Be}]2p^3 \rightarrow [\text{Be}]2p^23d$  transition in iron XX is plotted. There is a good agreement between the position and shape of the arrays as well as the features within them. Also given in the figure are the first few distribution moments, which agree reasonably in all cases. The close agreement between these aspects of the two calculated profiles confirms that the use of two codes will not appreciably effect our results.

Since we also aim to test the form of the correlation between component line energy and strength, it is important to confirm that any differences we see with previous work are not due to differences in the atomic code used. To this end the original analysis has been repeated using the COWAN code; the structure of the  $[\text{Kr}]4d^4 \rightarrow [\text{Kr}]4d^35p$  array in Pd XII has been used to investigate the variation of  $\sigma_a$  with  $\epsilon$  across the transition array. The data are plotted in figure 7.7, and in this case support the original conclusion (equation (7.1.12)) very well. A least-squares fitting of a linear relationship between  $\ln(\sigma_a^2)$  and  $\epsilon$  yields the coefficients  $\alpha = -1.0 \pm 0.1$  and  $\beta = -0.51 \pm 0.02 \text{ eV}^{-1}$ . In the original work the gradient of this relationship was found to be  $\beta = -0.44 \pm 0.02 \text{ eV}^{-1}$ , in poor agreement with our analysis. This difference between two calculations



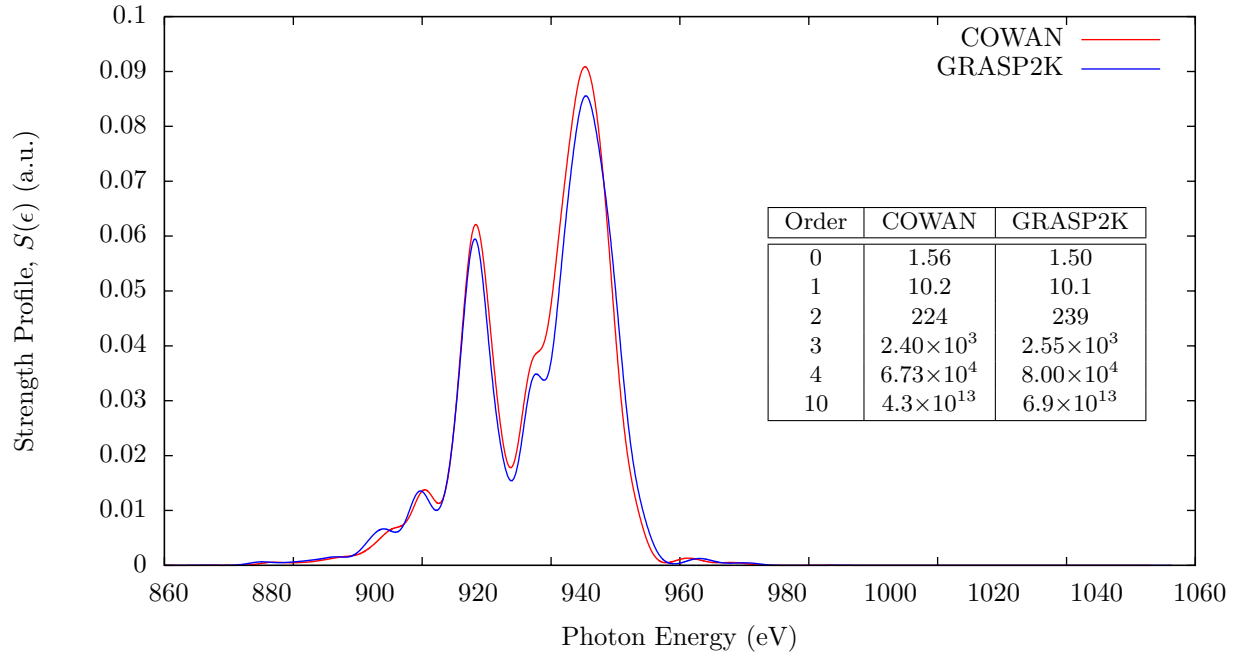


**Figure 7.6:** Comparison of the strength profiles  $S(\epsilon)$  for the  $[\text{Be}]2p^3 \rightarrow [\text{Be}]2p^23d$  transition in iron XX. The graph shows a good agreement between the two codes. The plotted profile includes an instrument width such that both cases have a porosity of  $P = 1$ . Also shown are a selection of the moments of the two distributions which also show a good agreement. The two calculations give the width of the strength profile as 120 and 118 eV respectively.

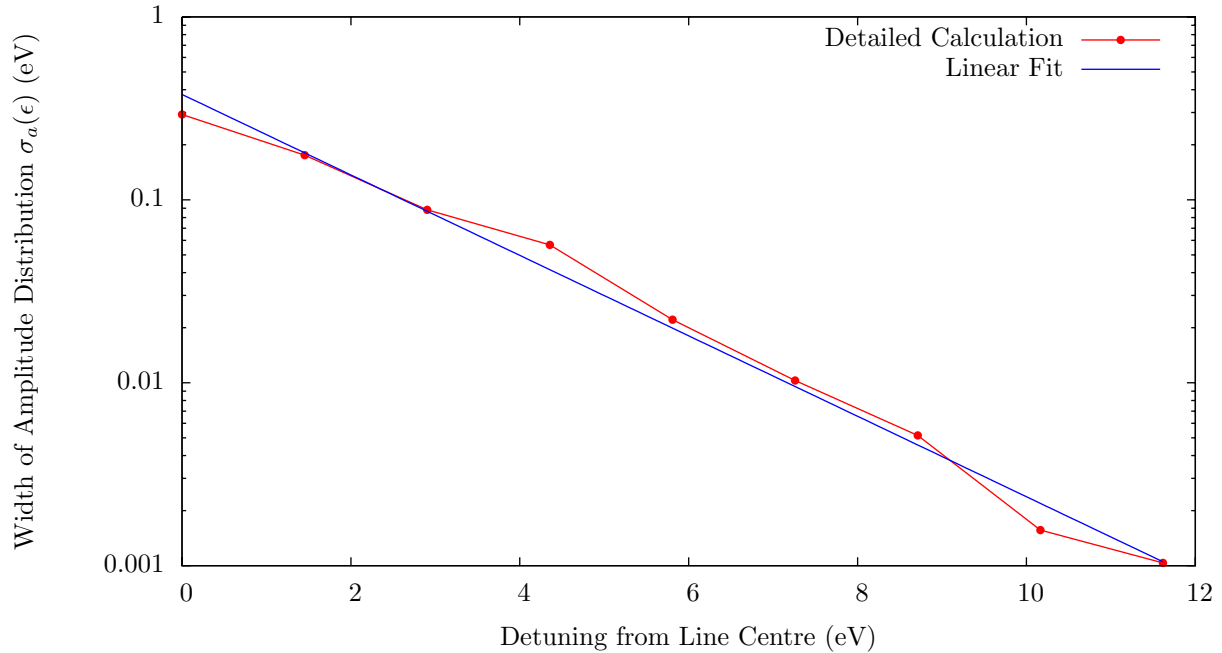


**Figure 7.7:** Calculation of the standard deviation of the distribution of variances of term lines as a function of energy in the  $[\text{Kr}]4d^4 \rightarrow [\text{Kr}]4d^35p$  transition in Pd XII. This is a repeat of the analysis performed by Bauche et al and reaches the same conclusion, that in this case the correlation between strength and energy is log-linear. Different behaviour seen in other transition arrays are not, therefore, due to differences in the atomic models used.

can be traced to differences in the strengths of individual component lines, evidence of which can be seen in differences between the moments of the strength distribution in the two analyses. The most important aspect of the analysis is the form of the correlation, and in that respect the two calculations agree and we have confirmed that any differences seen in the following analysis are due to inaccuracies in the form of the correlation (7.1.12), not the atomic models used.

We have now confirmed that the full calculations we propose to use are appropriate, and move on to build the framework to use for their analysis. We begin by quantifying the porosity of a transition array. This is determined by the extent to which adjacent component lines are smoothed into each other by line broadening effects. For broadening that results in a Gaussian lineshape of standard deviation  $\sigma_\phi$ , the opacity due to two isolated lines of the same strength will have a single peak when

$$\delta_\epsilon > 2\sqrt{2\ln 2} \sigma_\phi ,$$

where  $\delta_\epsilon$  is the distance between the two lines. We then define the array porosity  $P$  as

$$P = 2\sqrt{2\ln 2} \frac{\sigma_\phi}{\bar{\delta}_\epsilon} ,$$

such that an array with a large porosity ( $P \gg 1$ ) is smooth. In the above the line spacing has been averaged over the transition array to give  $\bar{\delta}_\epsilon$ ; in the case of a Gaussian distribution of line energies this can be performed analytically over the central portion of the lines (it is infinite if the average considers the entire array). The result for an average over the central two standard deviations is

$$\bar{\delta}_\epsilon = \frac{2\sigma_\epsilon}{N_{TL} \operatorname{erf}\left(\frac{1}{\sqrt{2}}\right)} ,$$

and therefore

$$P = \sqrt{2\ln 2} \operatorname{erf}\left(\frac{1}{\sqrt{2}}\right) \frac{\sigma_\phi}{N_{TL} \sigma_\epsilon} = 1.89 \frac{\sigma_\phi}{N_{TL} \sigma_\epsilon} , \quad (7.3.1)$$

where  $N_{TL}$  is the number of component term lines in the array. The porosity of a transition array can

therefore be defined in terms of known quantities. The derivation above, however, is inaccurate for several reasons. The most drastic approximation is the assumption that all lines in the transition array have the same strength; when an array contains a small number of strong lines it is the splitting between these that determines the overall porosity of the line profile, not the average splitting between adjacent lines. Similarly, the condition for two lines to be unresolved neglects the presence of other component lines, the wings of which will significantly effect results. These effects not only change the magnitude of  $P$  that is required to give a smooth profile, but also the dependence of this on the number of component lines  $N_{TL}$ . Averaging over only the strongest lines and the central portion of the transition array allow semiempirical definitions of  $P$  to be found however we have found that these still give inconsistent results for small arrays and those with long range structure. In particular transition arrays split by the spin orbit interaction are poorly described due to the large transmission window between subarrays. This problem is inherent in our approach and can be regarded as a statistical error. It should therefore be appreciated that in the data presented the  $P$  parameters quoted in the following data are estimates of the smoothness of the transition array only.

The accuracy of the  $P$  parameter can be seen in figure 7.8, in which the number UTAs that have less than 3 resolved peaks is plotted as a function of the porosity parameter  $P$ . We use this definition of a ‘smooth’ array in order that transitions which display strong spin-orbit splitting (and therefore may have 3 peaks) are considered smooth when each subarray has no extra peaks. The graph only includes those UTAs in our set that have more than 3 component lines, leaving 275 UTAs. It can be seen that as expected the number of unresolved arrays increases with increasing  $P$  however even for very large porosity parameter not all arrays are smooth.

If the above definition of  $P$  is valid it would be expected that all transition arrays have less than 3 peaks when  $P = 1$ . As mentioned this is not the case for any value of  $P$ , however the data in figure 7.8 demonstrate that when  $P = 5 - 10$  the majority of lines are smooth. We therefore propose to retain the Gaussian  $P$  parameter derived previously, with the knowledge that the criteria for a smooth line is shifted upwards. Similarly, the errors introduced by this approach will be considered when any conclusions or comparisons are made.

We aim to analyse the statistics of the transition arrays in our sample set, and move on to study

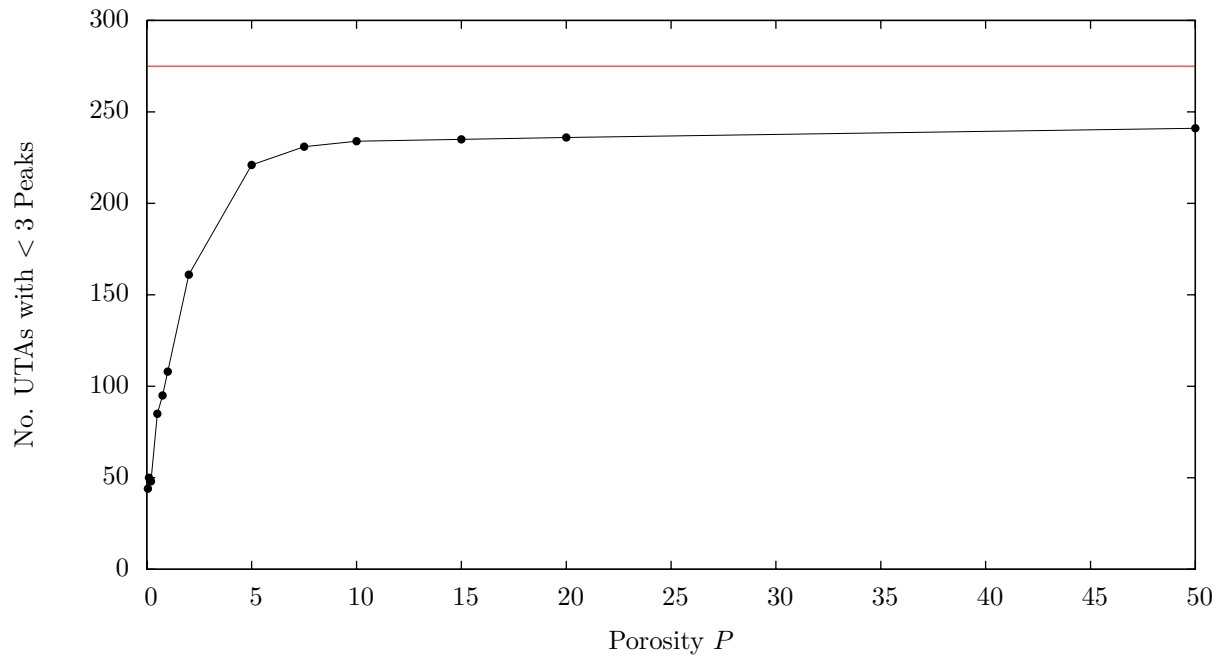


**Figure 7.8:** The number of transition arrays with less than 3 distinct maxima in their absorption profile as a function of porosity parameter  $P$ . As expected as  $P$  increases transition arrays have less maxima (and are therefore ‘smoother’ however the plot demonstrates the systematic and random error in our definition (equation (7.3.1)). The point at which most arrays are smooth is shifted to  $P = 5 - 10$  and there is no value of  $P$  that ensures all arrays are smooth.

the resulting opacity. Useful preliminary results can be found by examining the moments of the strength distribution as defined previously,

$$\alpha_S^{(n)} = \frac{1}{S_{TOT}} \int_{-\infty}^{\infty} (\epsilon - \bar{\epsilon})^n S(\epsilon) d\epsilon = \frac{1}{S_{TOT}} \iint_{-\infty}^{\infty} S(\epsilon - \bar{\epsilon})^n D(\epsilon, S) dS d\epsilon .$$

Calculation and comparison between various moments will give insight into the actual distribution of component lines, however we are also interested in how the various UTA models effect the results of full opacity calculations. To that end we will examine the average opacity. The particular average we want to test is the Rosseland mean, however calculating this quantity for an isolated line is problematic for several reasons. The first is the fact that the reciprocal of the opacity appears in the integrand, and so integrating over an infinite range will preferentially sample the regions of low opacity far from the line. The result will then be independent of the shape of the absorption line and will not diagnose differences between UTA models. We therefore limit our integration range to 7 standard deviations either side of the line centre, chosen so that the

UTA models will have dropped by a factor of around  $10^{10}$  at the edges of the integration range. A second problem is encountered due to the weighting factor in the Rosseland mean, which decreases exponentially for  $\epsilon > k_B T$ , making the integral sensitive to only the lowest photon energies in the integration range. In order to avoid these two problems we propose to instead calculate a ‘harmonic mean opacity’ defined as

$$\kappa_H = \int_{\epsilon_1}^{\epsilon_2} \frac{1}{\kappa_{TOT}(\epsilon)} d\epsilon, \quad (7.3.2)$$

where  $\kappa_{TOT}(\epsilon) = \kappa_{UTA}(\epsilon) + \kappa_0$  is the total opacity due to a given UTA line profile and a constant background  $\kappa_0$ .

Even when the integration is limited, the background opacity is essential in preventing the integrand of equation (7.3.2) from blowing up at the edges of the integration region. It also plays a physical role by modelling the relative strength of lines in the spectrum, which will vary over orders of magnitude in a full opacity calculation. Varying the size of  $\kappa_0$  allows lines to be scanned from large to small, and in effect this changes the region of the line that is sampled by the harmonic mean. This effect can be seen in figure 7.9 where the cumulative harmonic opacity is plotted across the integration range for a single UTA. The harmonic mean is shown for various values of the background opacity  $\kappa_0$ , expressed as a fraction of the peak opacity of the UTA profile. It can be seen that as  $\kappa_0$  is reduced, effectively making the absorption feature stronger in the spectrum, the line wings become more important to the harmonic mean and the line centre less so. This can have an important effect on the results of a simulation; in the example shown the harmonic mean varies by a factor of 20. To deal with this we introduce a second parameter defined as

$$\Gamma = \frac{\kappa_0}{\bar{\epsilon} (1 - e^{-\bar{\epsilon}/k_B T}) \max\{S_i\}}, \quad (7.3.3)$$

where we use the maximum strength in the detailed calculation in order to keep  $\Gamma$  independent from the porosity  $P$ . The two dimensionless parameters  $P$  and  $\Gamma$  then allow arrays to be fully quantified and by varying them in our analysis we are able to consider transition arrays of all types.

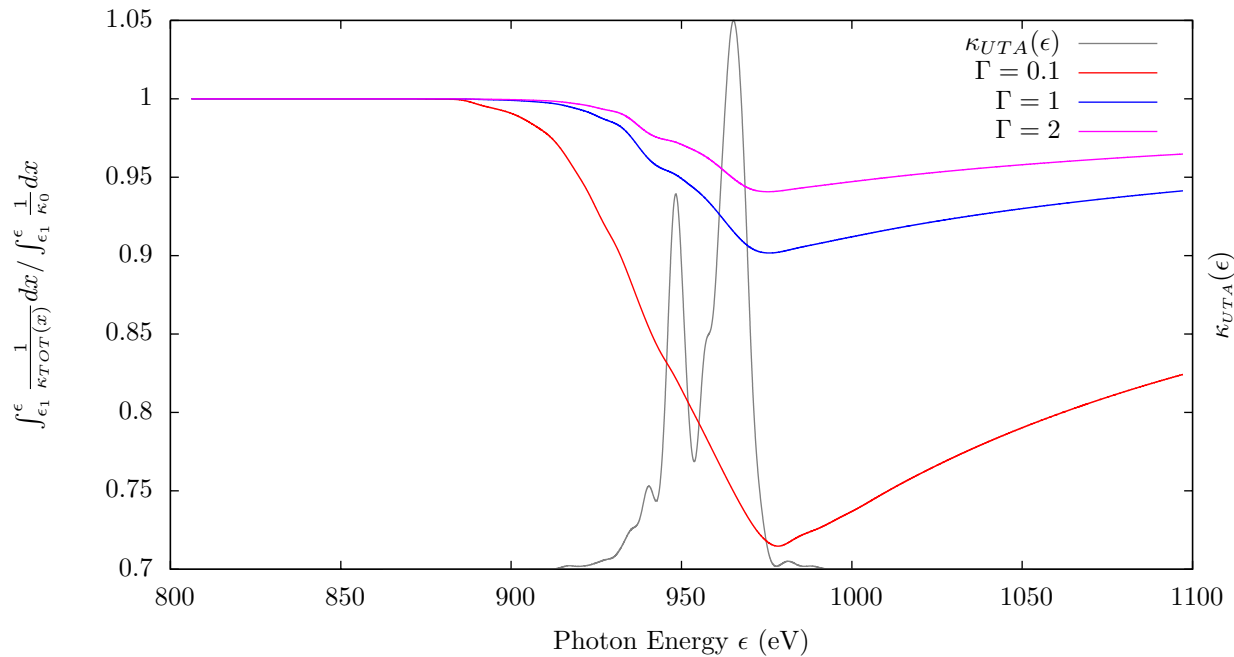


**Figure 7.9:** The cumulative harmonic mean opacity for a single UTA plus a constant background opacity of varying height, as a fraction of the background harmonic strength only. The stimulated emission correction has been neglected and the detailed line profile (shown in gray) is calculated with a porosity  $P = 1$ . The height of the background is calculated as a fraction of the peak value of the detailed line profile, and it can be seen that varying this fraction changes the portion of the line that contributes to the harmonic mean.

## 7.4 Results I - Transition Array Statistics

Before we examine the effect of high order moments on the opacity, it is informative to investigate how the shape of transition arrays in a full opacity calculation will depart from Gaussian. To do this we begin by calculating the third and fourth moments of the strength distribution for each transition array in our reference set and comparing it to the Gaussian values.

In figure 7.10 we examine the skewness of the transition arrays using the third standardised moment

$$\gamma_3 = \frac{\alpha_S^{(3)}}{(\alpha_S^{(2)})^{3/2}}, \quad (7.4.1)$$

which is equal to 0 for a symmetric distribution. The UTA model is a statistical model and so the larger arrays in the reference set are more significant; we therefore plot skewness against number of component lines and focus on the right hand side of the plot. It should be noted that in an opacity calculation arrays of

all sizes must be included and so small arrays are still relevant to this study. The red line shows the result for a symmetric array; there is significant spread around this value even for large transition arrays showing significant non-symmetric behaviour in the strength distribution. This asymmetry cannot be described by any of the models that we consider besides the Gram-Charlier expansion, and we have already seen that an error in the 3<sup>rd</sup> order moment can cause a change in the width of the observed absorption feature. The inclusion of the skew of transition arrays may, then, be important.

As with the skewness coefficient, non-Gaussian behaviour of the kurtosis is significant since it will change the profile of the line in the wings leading to changes in the transmission of a plasma far from line centre. Figure 7.11 shows a similar plot as for the skewness coefficient, where we plot the kurtosis coefficient,

$$\gamma_4 = \frac{\alpha_S^{(4)}}{(\alpha_S^{(2)})^2}, \quad (7.4.2)$$

against the number of component lines in the transition array. The kurtosis coefficient of a Gaussian distribution is 3, and this is also marked on the figure. As with the skewness there is significant spread around the value, with larger arrays systematically having a kurtosis larger than 3. This non-Gaussian behaviour can be accounted for using either the Gram-Charlier expansion or the correlated model of Bauche *et al.*; for  $\gamma_4 > 3$  they will be heavier in the wings than the unmodified models. This has the effect of reducing the absorption at line centre, similar to a change in linewidth, however this is distinct from the line narrowing caused by correlations.

The effect of correlations is to produce a change in the width of a transition array which we have described through the parameter  $\rho$ , the ratio of unweighted to weighted array variances (see equation (7.1.14)). We begin by calculating the value of  $\rho$  for all transition arrays in order to measure the importance of including correlations; the results are shown in figure 7.12. The figure confirms the effects of correlations on almost all transition arrays, and shows that the majority of transition arrays are narrowed by the presence of correlations ( $\rho < 1$ ). In the model of Bauche *et al.* these correlations modify the 4<sup>th</sup> order moment; this can be tested by taking the true narrowing of an array, calculating a predicted 4<sup>th</sup> moment using equation (7.1.16), and comparing it to the true value. The results of this comparison are shown in figure 7.13.

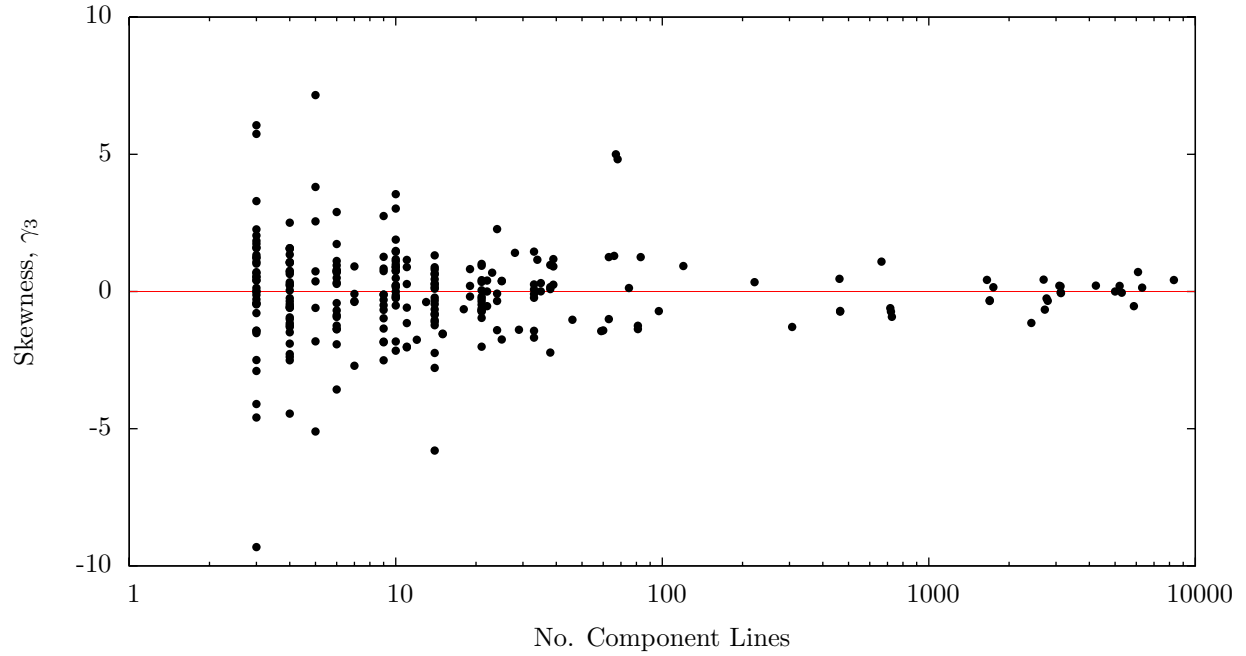


**Figure 7.10:** The skewness coefficient, defined by equation (7.4.1), for all transition arrays in this study. The very large spread in the data demonstrates the non-symmetric nature of the strength distribution for a large proportion of the transition arrays in an opacity calculation.

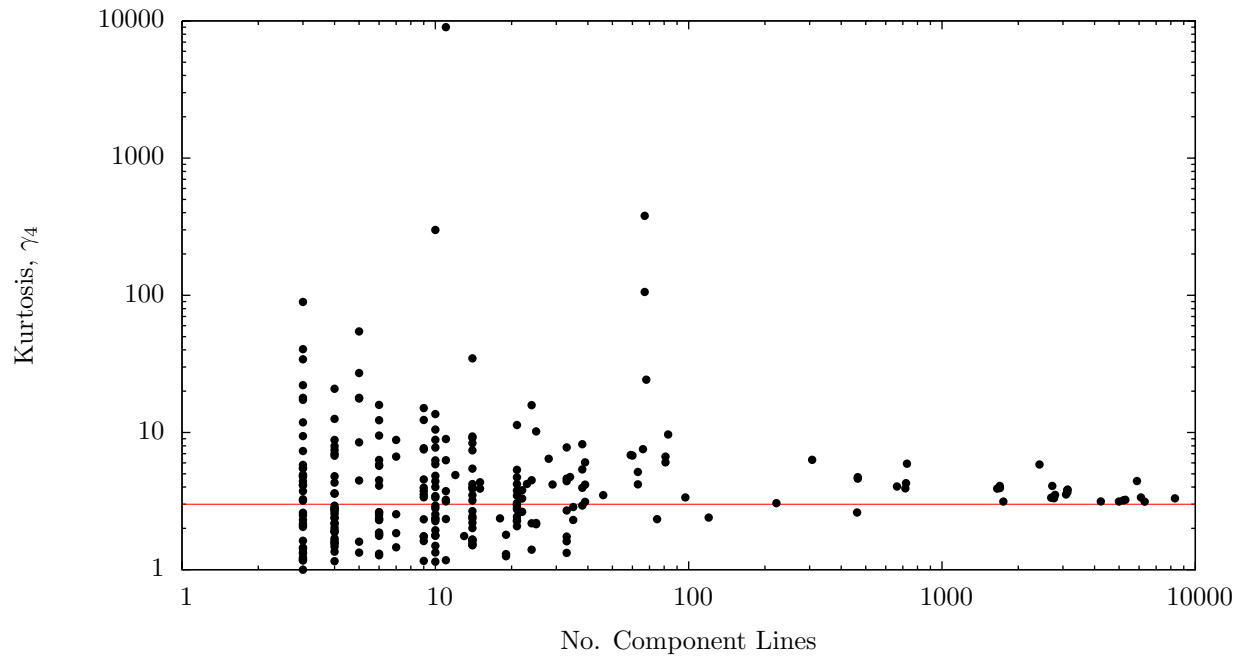


**Figure 7.11:** The kurtosis coefficient of the transition arrays in this study, defined by equation (7.4.2). Also shown is the Gaussian value of 3, and the large spread around this value shows the significant non-Gaussian behaviour of transition arrays of all sizes.



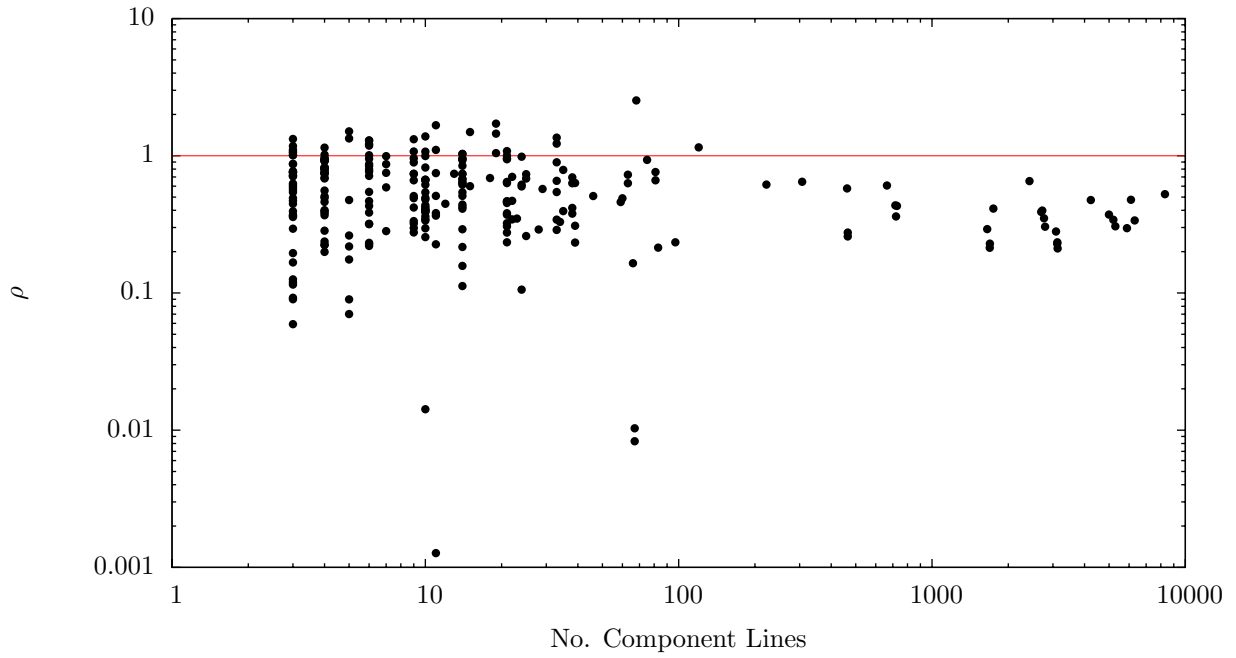


**Figure 7.12:** The value of the line narrowing parameter  $\rho$  (equation (7.1.14)) for each of the transition arrays in this study. Also shown is the  $\rho = 1$  line, below which transition arrays are narrowed by correlations. It can be seen that for the majority of the arrays, and for all of the arrays with  $\gtrsim 100$  component lines, transition arrays are significantly narrowed by correlations.

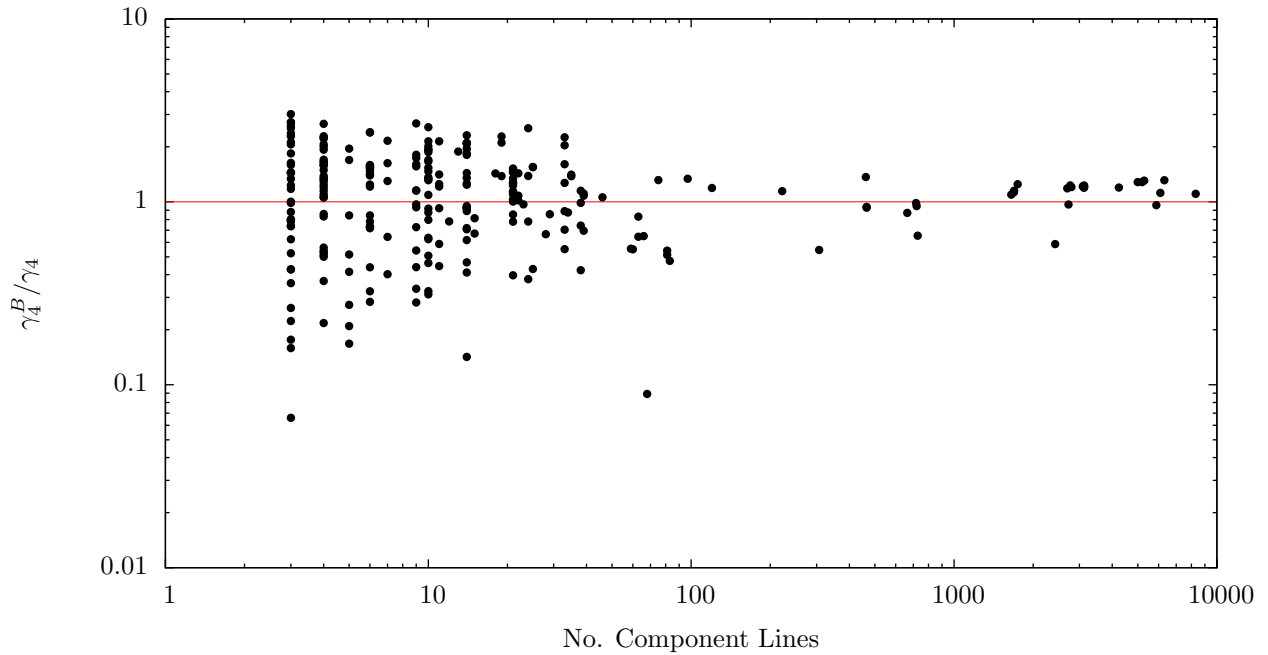


**Figure 7.13:** The ratio of the kurtosis of transition arrays calculated using the correlated model of Bauche et al. (see section 7.1.3) to the detailed value. It can be seen that even for large arrays, the model overestimates the kurtosis coefficient. This suggests that the form of the correlation assumed in this model is not successfully describing the general case.

The comparison of model and detailed kurtosis coefficients demonstrates that the model does not accurately describe the kurtosis of transition arrays in the general case. In most cases the kurtosis is overestimated producing a line with wings that are too heavy. This result suggests that the log-linear form assumed in the work of Bauche *et al.* does not reflect the true behaviour of a general transition array. It remains to be seen how this inaccuracy will change the results of opacity calculations.

## 7.5 Results II - UTA Models and the Mean Opacity

The preliminary results presented in the previous section have shown that the assumption that distribution moments above the 2<sup>nd</sup> can be modelled as Gaussian is not valid. The errors introduced by this assumption are mixed into the position and width of the absorption profile through other energy dependant factors according to equation (7.1.8). We have also shown that the effect of correlations is to significantly narrow transition arrays, reducing the standard deviation of the absorption array which in the same way can cause a change in the absorption line position. Finally we saw that the current model that allows these effects to be included is flawed in its description of the underlying physics.

We now aim to investigate the relative importance of these results with respect to the results of an opacity calculation. We use the methods described in section 7.3 to find the harmonic mean opacity in each UTA model described previously, along with the detailed (DTA) model. This allows the fractional error in each model,  $\kappa_H / \kappa_H^{DTA}$  to be found for every transition array in our sample set. Histograms of fractional error can then be formed for each model by grouping UTAs into bins according to their individual error. An example is shown in figure 7.14 where bars indicate the widths of the bins. The same data are also shown using a line plot that allows several datasets to be compared. We will use this format in the following sections. In such plots the position of the peak will indicate a systematic error in the UTA model, and the width of the peak gives the random error.

In order to reflect the different regimes which UTA models must address we choose a range of the parameters  $P$  and  $\Gamma$  to give a range of conditions from strong, resolved lines to weak, smooth structures and all cases in between. The background opacity and line broadening are calculated separately for each array so that the specified conditions are met, however some random errors can be expected due to the difficulties

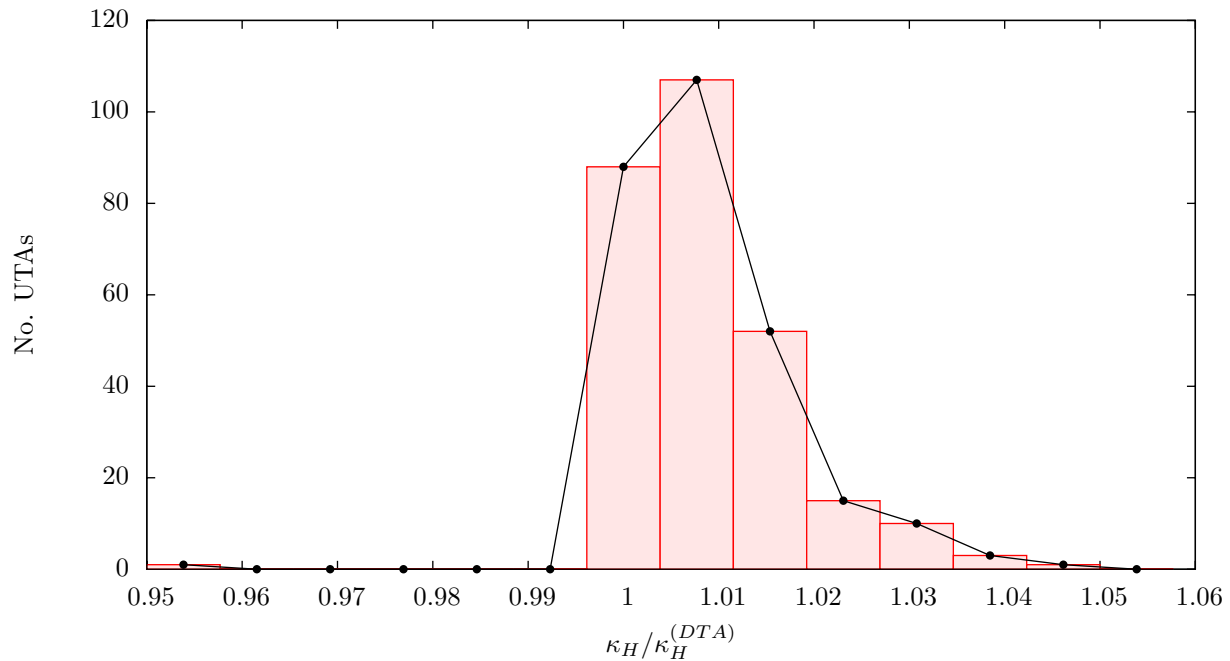


**Figure 7.14:** An example of the data collected in section 7.5. The number of transition arrays with a given fractional error is plotted, where the error is calculated as a ratio with the result of a detailed calculation. The shown data are for the uncorrelated Gaussian model where  $P = 0.5$  and  $\Gamma = 1$ .

described previously. The magnitude of the fractional error should also be treated with care since it is very sensitive to the background opacity and integration range. We will, therefore, use the collected data to compare different UTA models and analyse trends without making conclusions as to the final accuracy of UTA models compared to detailed calculations. Such an analysis can only be reliable if opacity calculations are performed using a full physics model and over a large spectral range. Performing such large scale, detailed calculations is not feasible in this work however other authors have placed constraints on the accuracy of UTA models [64].

In figure 7.15 results are plotted for fairly strong and fairly weak lines (left and right columns respectively) and for porous to smooth lines (top to bottom). The values of  $P$  shown mean that in the smoothest case,  $P = 20$ , the line shape is dominated by the plasma broadening but some structure is visible in some cases; in the opposite case  $P = 1$  all arrays will have term lines visible. The values of  $\Gamma$  vary the strength of the lines, but the dominant contribution to the harmonic mean is the line centre in both cases.

The figure demonstrates the breakdown in the UTA model for very porous lines, shown by the broadening

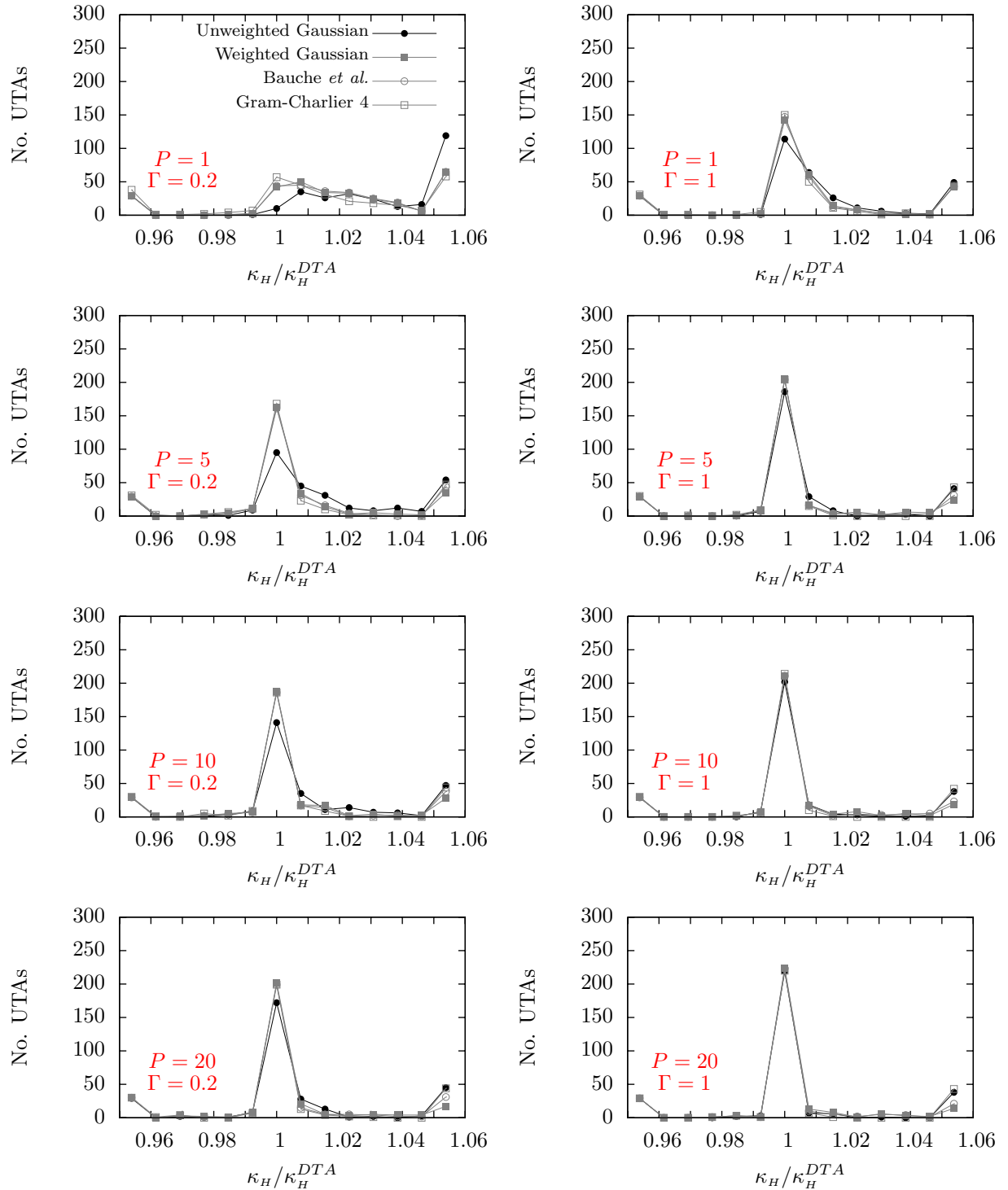


**Figure 7.15:** Histograms showing the fractional error in the harmonic mean opacity  $\kappa_H$ . Data are shown for various line parameters  $P$  and  $\Gamma$ , corresponding to a scan from very porous lines (top row) through to smooth lines (bottom), and strong (left column) to weak (right). It can be seen that the simplest uncorrelated model is unreliable at all cases except when broadening overcomes term structure, and that improved models all give much the same results.

and shift of the peak as  $P$  decreases. This result is unsurprising as this is the regime in which the UTA model is expected to fail. The nature of the breakdown is also as expected, with the UTA models overestimating the true opacity due to the neglect of transmission windows between the component lines. The effect is much less marked for weaker lines as in this case the background opacity overrides the effect of absorption lines. This result can be seen on the right hand side of figure 7.15 where the error distribution remains peaked at 1 even for the most porous arrays. The only effect of increasing term line structure on the higher  $\Gamma$  case is to increase the width of the error distribution, indicating random errors as the line strength in the DTA profile is concentrated into smaller regions. This effect is most pronounced in cases where detailed calculations are split by the spin-orbit interaction or show some other long-range structure.

The most significant conclusions that the data in figure 7.15 show concerns the relative accuracy of the 4 different UTA lineshapes in this study. The uncorrelated model (shown in black) is accurate only for the cases where the individual line width is so large that it washes out term structure altogether. This model breaks down rapidly as term structure becomes important, even when this is only affecting global UTA properties. This is consistent with the previous conclusion that the total neglect of correlations is not valid (see figure 7.12). The other models are more accurate for intermediate values of  $P$  and give much the same error distributions as each other; the correlated Gaussian and the model of Bauche *et al.* agree at almost all points, and the Gram-Charlier expansion gives little improvement. These models differ in the way that they deal with high order moments and so this result suggests that these make little difference to the opacity. These data, therefore, show that provided the UTA model is valid (ie, that  $P$  is large enough), a good description of the opacity can be obtained using a Gaussian model as long as correlations are included in the width.

The calculation of the proper Gaussian UTA width has, as mentioned, been investigated resulting in closed formulae [125]. The formulae are a reformulation of the atomic physics of the problem and so are exact yet fairly slow to implement. The above results mean that this calculation is the *only* transition-resolved atomic physics that is required in a DCA code and so the exact determination of array width is feasible for reasonably small-scale codes. For the fastest applications, however, this approach is still too slow. It is therefore interesting to investigate how faster models can be modified to improve results.

The model used in IMP approximates the array variance as the sum of the variances of the energies of the upper and lower configurations. In this way it not only neglects correlations between energy and strength, but also the selection rule on  $\Delta J$  that limits the number of transitions giving rise to so-called ‘emissive zones’ in the two configurations [131]. We saw previously that this selection rule acts to link states that are in similar positions in the upper and lower configurations; the variance as calculated by IMP neglects this effect. We can test the importance of this second approximation separately from that of correlations by comparing the unweighted standard deviation of transition energies  $\sigma_\epsilon$  calculated exactly and in the IMP model. This is done in figure 7.16 where we plot these two quantities on each axis. It should be noted that since IMP is an inherently  $jj$ -coupled model we only include detailed calculations run using GRASP2K. The data show a poor agreement with the  $y = x$  line (red); the IMP calculations have a random error of up to an order of magnitude compared to detailed calculations. This error is incurred before the errors associated with the neglect of correlations are taken into account; when developing new models it is therefore necessary to use a more accurate model even when correlations are neglected or compensated for. The methods used

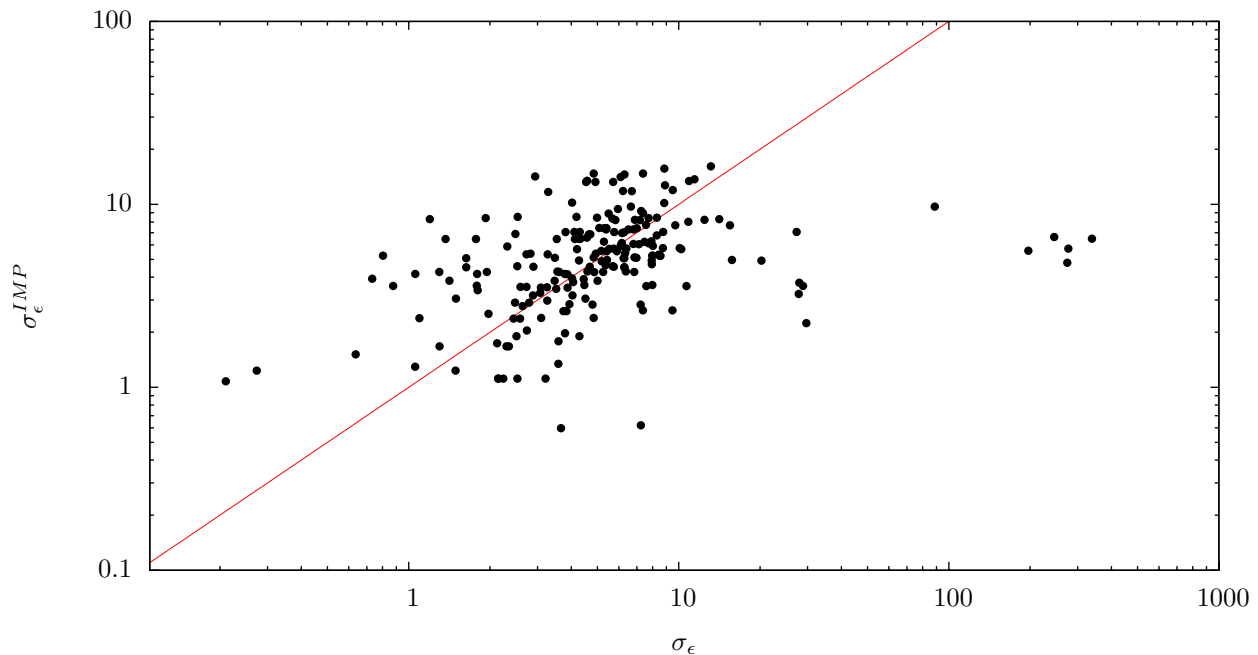


**Figure 7.16:** Comparison of the variance in transition energy calculated using IMP and the GRASP2K code. On the  $x$  axis the standard deviation from detailed calculations is plotted, and the IMP result is shown on the  $y$  axis. The red line shows the  $y = x$  line. It can be seen that the IMP model gives random errors of up to an order of magnitude.

by Bauche-Arnoult *et al.* to find the weighted standard deviation could be readily applied to this problem since they rely on general properties of the Hamiltonian only. The resulting expressions can be expected to be simpler than those for the weighted width since they only involve the matrix elements of the Hamiltonian in some coupling scheme.

We have already shown that such calculations would not be sufficient since they neglect correlations. A simple modification can be proposed by considering the average value of  $\rho$  that we found in the previous section, which gives the average effect of correlations on the widths of transition arrays. This can be used to correct unweighted widths to give an approximate description of correlations. For the UTAs in our reference set we found  $\bar{\rho} = 0.59 \pm 0.02$  when averaged over all lines in the set, and  $\bar{\rho} = 0.39 \pm 0.03$  when only lines with more than 100 components are included. In figure 7.17 we show a histogram of similar data as in figure 7.15, calculated using a Gaussian model of three different widths. Gaussian UTAs of the weighted and unweighted widths are shown along with the same model with the unweighted width multiplied by 0.59. The calculations are for strong lines of intermediate porosity ( $\Gamma = 0.2$ ,  $P = 5$ ).

The data show that the reduction of the unweighted variance does not give an appreciable improvement over the unweighted Gaussian UTA. There is a slight shift out of the  $\kappa_H > \kappa_H^{DTA}$  wing however the extra broadening of the peak of the distribution, which arises due to the statistical error associated with use of the  $\bar{\rho}$ , counterbalances this and there is a large number of transition arrays that underestimate the harmonic mean opacity. Looked at another way, the reduced (heavy black line) and weighted (blue line) models now have the same average correlation factor  $\rho$ , however there is a very significant difference in the error associated with each model due to the average treatment in the simple model we have proposed.

For larger arrays, where the UTA model is more appropriate, there is significantly less scatter in  $\rho$  about the mean value (see figure 7.12) and so slightly more success can be expected in these cases; however the work presented here cannot suggest how  $\bar{\rho}$  may vary for different elements or different transitions making such an approach very unreliable in the general case.

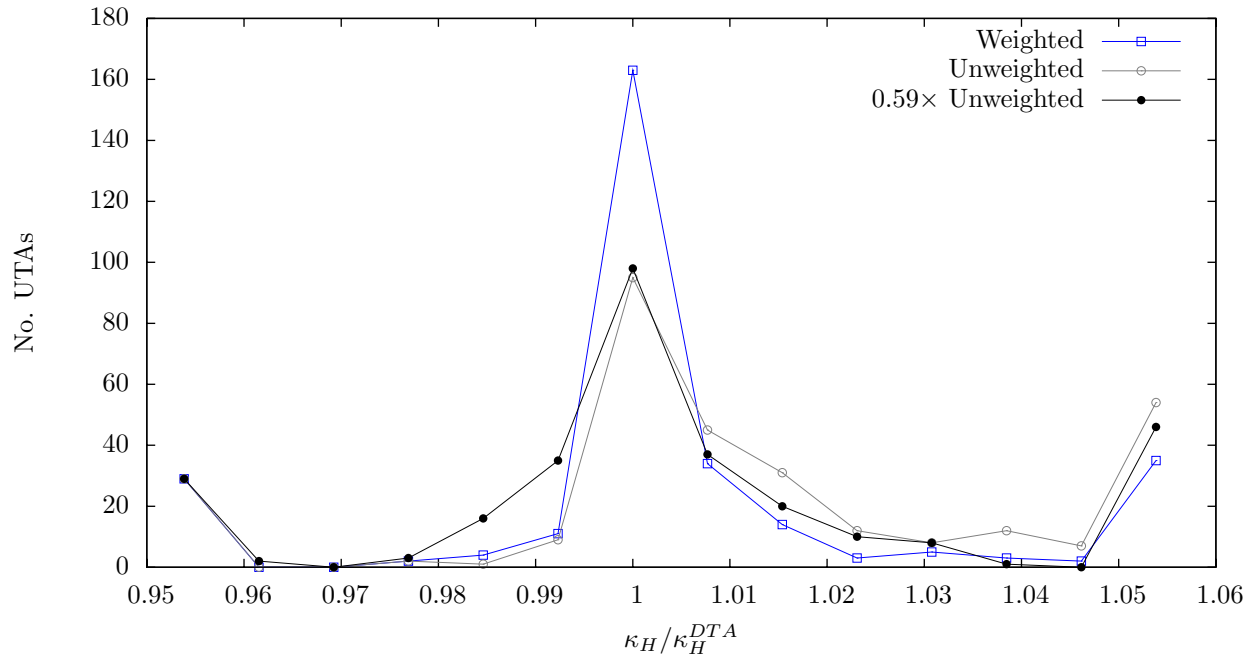


**Figure 7.17:** Testing of a reduced width UTA model in which the unweighted variance is multiplied by the mean line narrowing due to correlations,  $\bar{\rho} = 0.59$ . Data are calculated for  $P = 5$  and  $\Gamma = 0.2$ . Also shown are the ‘correct’ strength-weighted Gaussian and unmodified unweighted Gaussian models. It can be seen that there is little improvement when this simple correction of correlations is used, and that the peak in the distribution is broadened by random errors.

## 7.6 Discussion

Unresolved transition array models have seen continual development for several decades, however systematic testing has rarely been undertaken and so the results given in this section are useful in providing an objective comparison of the various choices of UTA a new code can consider. The theoretical basis is also rarely given, perhaps due to the intuitive nature of the original work. This makes the discussions given at the beginning of this section valuable.

The analysis of the mixing of transition array moments due to convolution and energy dependant prefactors are very relevant to this field since most work is focussed on improving the description of high order moments in UTA models. We have shown that these moments are not important for calculations of the harmonic mean opacity however the change in strength, shift and broadening of transition arrays due to errors in high order moments may be of relevance to other aspects of spectral modelling. In particular much is learned about a plasma system by examining the detailed shape and width of transition arrays; the results



given in this section may provide additional sources of broadening and shift, for example. The form of the mixing is strongest for transition arrays with low average energies, and for low temperature plasmas, and so it is unlikely that these effects are significant for X ray diagnostics of opacity experiments themselves. It is also much more feasible to use detailed atomic models in these cases since only a few arrays need be analysed; this does not fully remove the problem since the high order moments of the lineshape due to other broadening processes are also mixed into the observable transition array.

We have presented a simple analysis of the structure of a transition array that elucidates the factors that influence their shape; in particular the effect of spin-orbit splitting. This model only applies to subsets of transitions under pure coupling conditions, however the distribution function that has been derived could prove useful in the analysis of so-called ‘scars of symmetry’, in which the effects of pure coupling persist in configurations that are far from those conditions. The detailed data that we have generated in this section display these scars and so further work may allow the confirmation of the distribution function given above. The physical importance of such work is not clear, however.

In order to form as complete an analysis as possible, we have presented a framework under which transition arrays can be tested in a range of plasma conditions. In effect the porosity parameter  $P$  describes changes in electron density, for example, leading to changes in the width of absorption lines. Similarly changes in the strength of the lines compared to the background models the change in initial ion population as the temperature changes. This work is of interest in more complex approaches to opacity calculations since it provides a method of determining how applicable the UTA model is for a given transition array in simple terms. The errors associated with this, in particular the  $P$  parameter, make the direct implementation of this unreliable. In this work we have attempted to find more reliable methods however the best seems to be the one employed here; a simple definition of the parameter and analysis of how it behaves. The difficulties in characterising the resolution of a general transition array are the same as the difficulties encountered in trying to simply describe any property of a transition array - the complexity of the underlying atomic physics.

The main focus of this section has been to present the statistical analysis of a large number of transition arrays. The least surprising result from this is that arrays with few component lines are not amenable

to the statistical approach; it therefore seems likely that future opacity codes will use detailed models to describe these. The average behaviour of the skewness and kurtosis of large transition arrays has been shown to be fairly regular - they are in general symmetric and have a kurtosis slightly larger than the Gaussian value. In the random matrix theory which has given useful results in the study of nuclear properties these quantities are related to the symmetry properties of the Hamiltonian however little can be said that is of use in modifying existing UTA models. The work in the second part of this section has shown that these moments are not important in the description of the mean opacity anyway.

The biggest assumption in this work is the splitting up of the transition arrays in our test set. The Rosseland and harmonic mean opacities are not additive with respect to individual transition arrays and so the relevance of our results to full opacity calculations is not too clear. The introduction of a background opacity has helped to alleviate these problems since this appears in the formula for the harmonic mean in the same way that the contribution from other lines. This then means that the only problem introduced by other lines is a variation of  $\kappa_0$  with energy with the associated mixing of moments and change in shape of the transition array. Since we have also made efforts to include energy dependant prefactors, the data we have given is as robust as possible. Only a survey of full opacity calculations, comparing the Rosseland means of various different codes or experiments, would give a more reliable comparison. This was not feasible in this work.

In the light of the conclusion that a Gaussian model of the correct width gives a comparable error to other more complex models, we attempted to modify a simple Gaussian model to allow easy and fast implementation in fast models. We have shown that the random errors associated with replacing array properties by their average lead to a noticeable reduction in accuracy. This is not surprising given the comments we made earlier; transition arrays are not amenable to an average treatment of their properties. The potential accuracy of any UTA model is limited by this fact however the results we have given show that when applicable the UTA model can be a very useful approach nonetheless.

## 8 Summary & Conclusions

This work presented in this thesis has concerned the development of fast models for the calculation of the opacity of plasmas. The models that have been presented are chosen to keep calculation time to the absolute minimum, with the intention of providing useful results for the development of plasma simulations that can treat the properties of all plasma constituents - electrons, ions and photons - self consistently and accurately.

The results have been grouped into three separate investigations based on their application. These investigations are all motivated by the improvement of the IMP opacity code however many of the results are of relevance to the development of faster models from scratch. Throughout the report we use experimental data to benchmark the improved calculations; such data is a luxury that has arrived relatively recently and is invaluable in the development of models for all aspects of plasma dynamics. In almost all cases we see evidence that simple models can give a good description of the frequency resolved opacity.

Modern opacity codes place a large emphasis on the accuracy of their atomic models and on their ability to treat term structure correctly. Original IMP calculations use the semiclassical approximation for bound electrons and do not resolve term structure, and so the code has been upgraded to describe the average atom in the the Hartree-Fock-Slater model. This approach gives a much improved description of the bound charge density for a very small increase in calculation time (since we still use the average atom approximation). The improved charge density, however, translates to only a small change in the potential and therefore wavefunctions and eigenvectors. Comparison with calculations and two sets of experimental data have shown that this approach makes little difference, provided that the exchange potential is included. In the case of the experimental data of Hoarty *et al.*[106] an excellent agreement with experimentally measured inner-shell populations was seen. This is very encouraging. Comparison with a second experiment, that of Gregori *et al.* [110], showed a poorer agreement with the average ionisation of the plasma. It is suggested that since this quantity diagnoses the populations of all shells that this may be an effect of the simple ion cell model used in IMP; in particular the position of the continuum in energy may be too high. The analysis of the transmission through a niobium plasma in chapter 6 does not support this conclusion however the density

is an order of magnitude lower; that data also showed evidence that although the exchange potential in IMP gives significant improvement to the atomic model, errors associated with the local density approximation can be seen.

The HFS model implemented in IMP considers a centrally symmetric potential and therefore neglects the non central parts of the electron-electron interaction. This means that it does not consider the coupling of the orbital or spin angular momenta of electrons together and therefore does not resolve term structure. This is accounted for in the unresolved transition model (UTA), which is only appropriate when term lines are not visible in spectra. This is a major disadvantage when codes are applied to radiation transport problems where the instrument width is not present. We have therefore implemented the random transition array model (RTA) into the IMP code to give an improved description when term lines are narrow. In order to do this the calculation of the number of component lines in a transition array has been put into iterative form that suits DCA codes very well. This allows accurate initialisation of the RTA with only a small time penalty. The actual opacity calculation is still much slower, however, since the output grid is addressed many more times. During this work it was noted that the distribution function that should be used is not clear; this observation motivated the in-depth study of UTA models that forms the final chapter of this report.

Absorption lineshape and broadening is a complex issue in almost all plasma systems, and an extremely important one since line shapes can give a wealth of information regarding the state of the plasma. The detailed modelling of a single absorption line is a time consuming problem in itself and cannot feasibly be included in a fast model such as IMP. We have therefore investigated a simple model for the broadening of spectral lines by electrons in the impact approximation, using a modified version of the work of Baranger [36, 37, 38], Griem [116], and Dimitrijevic & Konjevic [117]. This approach uses the average atom approximation and therefore all widths can be calculated separately from DCA calculations; there is almost no numerical penalty. Comparison with experimental data due to Hoarty *et al.*, in which electron impact broadening is known to be important, has confirmed that the approach is valid with IMP results showing extremely good agreement with experiment. The accuracy of this agreement is as good as the description by more advanced opacity codes and broadening models.

In order to implement the electron impact broadening model described above it was necessary to include

in IMP the capability to calculate Voigt line profiles. This is a well known problem with many solutions however after a survey of the popular methods it was found that the detailed, accurate approach is far too time consuming for large scale opacity calculations. Look up tables, which are often favoured by the fastest codes, require large amounts of storage and so are not desirable either. We have therefore tested two simple algorithms for the Voigt profile over a range of parameters and chosen the Humlicek algorithm [121] for implementation in IMP calculations. It was also found that this profile would have an RMS fractional error of less than 10% provided that the Gaussian and Lorentzian widths satisfy  $0.1\sigma < \gamma < 6\sigma$ . The errors associated with resorting to a pure Gaussian or Lorentzian outside this range are large and so we choose to use Voigt profiles even outside the range of applicability.

No matter how simple an opacity calculation is made, the volume of calculations can be such that significant runtime is required. It is, therefore, useful to investigate the convergence of the results of opacity calculations with respect to the number of ion configurations included. We have developed an approach by which the configurations that contribute to a similar degree can be identified and included in calculations in a systematic manner. The approach is based on the partition function and this presents the opportunity for new codes to self-test convergence and stop when it is achieved. The success of this approach relies on the peakedness the configuration probability distribution compared to the degeneracy of states with low occupation; a series of examples motivated by experimental data have confirmed that the procedure is appropriate at various plasma conditions. This conclusion has allowed the modelling of further experimental data by Hoarty *et al.*, in which the average plasma ion has an open  $M$  and  $N$  shell. This poses a significant computational problem however the described approach allowed converged calculations to be produced in around an hour of CPU time.

The analysis of the converged data has again shown a very good agreement between IMP and experiment, however there are some problems. The first is that one transition array, corresponding to  $2s \rightarrow 4d$  transitions, is shifted with respect to the other arrays in the calculated spectra. This is due to a known problem with the LDA treatment of electron exchange. A second problem is seen for high photon energies where the overall transmission through the plasma is much larger than that in experiment. Examination of the calculations show that this occurs close to the onset of the  $L$  shell ionisation edge. A shift of this edge is consistent with

the previous conclusion that the ion cell model in IMP is not describing the effects of continuum lowering effectively, however a more detailed analysis suggests that this is not the case. It has been shown recently that the description of this experiment can be improved through the broadening of the ionisation edge to reflect the structure of the lower configuration [124]; this is not included in IMP calculations and so may explain the discrepancy.

In the final section of this thesis we return to the UTA model and attempt to assess its accuracy. We were motivated by the lack of a systematic test of the various UTA options that new codes could use, and so built a framework in which they could be tested as reliably as possible. This began with an in depth analysis of the theoretical basis for the UTA model, and a survey of UTA models. These models differ in their treatment of both the high order moments of the line strength distribution and of correlations between term line energy and strength. It is also shown that the presence of energy dependant factors in the definition of the opacity means that the high order moments of the strength distribution, which are determined by the approximation used, can influence the total strength, position and width of absorption features in the opacity spectrum. Formulae are derived to describe this mixing that show that it is most significant for low energy transitions, and the energy dependant factors are included explicitly in our analysis to ensure that mixing is treated correctly.

In order to test the effectiveness of the different UTA models a set of 304 transitions of relevance to a laser plasma opacity experiment have been analysed using detailed atomic models. We begin with some statistical analysis of these arrays and show that arrays of all sizes show significant non-Gaussian behaviour in their 3<sup>rd</sup> and 4<sup>th</sup> moments, and that the effect of correlations is to narrow transition arrays by an average factor of  $0.59 \pm 0.02$ . This analysis also allows the model for these correlations due to Bauche *et al.*[84] to be tested; this model is not capable of describing the kurtosis of transitions arrays correctly. This is evidence that the model is incorrect; it is confirmed that this is not due to differences in atomic models.

The statistical investigations described above are all evidence that the current set of UTA models cannot accurately describe the details of term structure in a general transition array. This approach does not test how these deficiencies effect the results of an opacity calculation. To that end we have also investigated their effect on the Rosseland mean, which we model through a harmonic mean opacity. Two parameters

are defined that can be varied to give smooth or spikey and strong or weak transition arrays respectively, allowing calculations to model all plasma conditions. For a set of these conditions the harmonic mean opacity is calculated for each transition array and compared to the detailed result. This process shows that all of the UTA models give comparable accuracy under all conditions provided that the correlations between line strength and energy are accounted for. The high order moments add little to the accuracy of the UTA model.

Finally, since the calculation of transition array moments including correlations is time consuming, we propose a simple correction to the uncorrelated line width based on the average line narrowing found from our investigations. Similar calculations as before have shown that this approach is an oversimplification. It is also not clear how the correction factor (0.59 in this case) varies with element or transition type.

The results described above have been motivated by the need for simple opacity calculations. We have shown that within the framework of the average atom, simple models for the most important physical processes can give good accuracy. It is not necessary to use more advanced atomic approaches such as the Hartree-Fock-Slater model when the AA description is used, provided that the exchange potential is included. Deficiencies in the LDA exchange model are visible in calculated spectra, however, as are inaccuracies introduced by the AA approach. It is shown that once these problems have been accounted for (by shifting spectra in this work), accurate results can be obtained for difficult systems such as the high density or  $M$ -shell plasmas we have considered here. Such calculations represent the current state of the art in opacity experiments and are challenging for any opacity code. Similarly, it is not necessary to provide a very detailed description of the positions of atomic term lines provided the low-order behaviour of the resulting lineshape is reproduced. These results are all of use for fast opacity calculations where the AA approach is essential.

## References

- [1] SJ Rose. Calculations of the radiative opacity of laser-produced plasmas. *Journal of Physics B: Atomic and Molecular Physics*, 25:1667–1681, 1992.
- [2] JA Gaffney and SJ Rose. Opacity calculations on plasmas with open M and N shell configurations. *High Energy Density Physics*, 5:216–218, 2009.
- [3] JA Gaffney and SJ Rose. The effect of unresolved transition arrays on plasma opacity calculations. *High Energy Density Physics* (submitted), 2011.
- [4] JN Bahcall, AM Serenelli, and M Pinsonneault. How accurately can we calculate the depth of the solar convective zone? *The Astrophysical Journal*, 614:464–471, 2004.
- [5] H Nagatomo, T Johzaki, T Nakamura, H Sakagami, A Sunahara, and K Mima. Simulation and design study of cryogenic cone shell target for Fast Ignition Realization Experiment project. *Physics of Plasmas*, 14:056303, 2007.
- [6] H Nagatomo. 2<sup>nd</sup> UK-Japan workshop on high energy density science, Edinburgh, January 2011.
- [7] J Castor. *Radiation Hydrodynamics*. Cambridge University Press, 2004.
- [8] RJ Tayler. *The Stars: their structure and evolution*. Cambridge University Press, 1994.
- [9] J Harvey. Helioseismology. *Physics Today*, pages 32 – 41, October 1995.
- [10] JP Cox. *Theory of Stellar Pulsation*. Princeton University Press, 1980.
- [11] JD Lawson. Some criteria for a power producing thermonuclear reactor. *Proceedings of the Physical Society*, B70(6):6–10, 1957.
- [12] G Hazak, AL Velikovich, M Klapisch, AJ Schmitt, JP Dahlburg, D Colombant, JH Gardner, and L Phillips. Study of radiative plasma structures in laser driven ablating plasmas. *Physics of Plasmas*, 6(10):4015–4021, 1999.
- [13] EL Moses. The national ignition facility and the national ignition campaign. *IEEE Transactions on Plasma Science*, 38(4):684–689, 2010.
- [14] RE Marshak. Effect of radiation on shock wave behaviour. *The Physics of Fluids*, 1(1):24–29, 1958.
- [15] MD Rosen. The physics of radiation driven ICF hohlraums. Lawrence Livermore Report UCRL-JC-121585, 1995.
- [16] TJ Orzechowski, M D Rosen, HN Kornblum, JL Porter, LJ Suter, AR Thiessen, and RJ Wallace. The Rosseland mean opacity of a mixture of gold and gadolinium at high temperatures. *Physical Review Letters*, 77(17):3545–3548, 1996.
- [17] D Mihalas. *Stellar Atmospheres*. Freeman, 1978.
- [18] EU Condon and PD Shortley. *The Theory of Atomic Spectra*. Cambridge, 1935.
- [19] DH Sampson. The opacity at high temperatures due to Compton scattering. *The Astrophysical Journal*, 129:734, 1959.
- [20] N Grevesse and AJ Sauval. Standard solar composition. *Space Science Reviews*, 85(1-2):161–174, 1988.
- [21] JN Bahcall and RK Ulrich. Solar models, neutrino experiments, and helioseismology. *Reviews of Modern Physics*, 60(2):297–372, 1988.
- [22] E Merzbacher. *Quantum Mechanics*. Wiley, 1998.



- 
- [23] HA Bethe and EE Salpeter. *Quantum Mechanics of One- and two- electron atoms*. Dover, 2008.
- [24] LC Biedenharn and JD Louck. *Angular Momentum in Quantum Physics*, volume 8 of *Encyclopedia of Mathematics and its Applications*. Addison-Wesley, 1981.
- [25] RD Cowan. *The theory of Atomic Structure and Spectra*. University of California Press, 1981.
- [26] IP Grant. Relativistic self-consistent fields. *Proceedings of the Royal Society of London A*, 262:555–576, 1961.
- [27] JC Slater. *Quantum Theory of Atomic Structure*, volume 1. McGraw-Hill, 1960.
- [28] JC Slater. *The Quantum Theory of Atomic Structure*, volume 2. McGraw-Hill, 1960.
- [29] G Racah. Theory of complex spectra I. *Physical Review*, 61:186–197, 1942.
- [30] G Racah. Theory of complex spectra II. *Physical Review*, 62:438–462, 1942.
- [31] G Racah. Theory of complex spectra III. *Physical Review*, 63(9):367, 1943.
- [32] JP Desclaux, DF Mayers, and F O’Brien. Relativistic atomic wave functions. *Journal of Physics B: Atomic and Molecular Physics*, 4(5):631–642, 1971.
- [33] DH Sampson, HL Zhang, and CJ Fontes. A fully relativistic approach for calculating atomic data for highly charged ions. *Physics Reports*, 477(4-6):111–214, 2009.
- [34] RM Martin. *Electronic Structure*. Cambridge, 2004.
- [35] TR Carson, DF Mayers, and DWN Stibbs. The calculation of stellar radiative opacity. *Monthly Notices of the Royal Astronomical Society*, 140:483–536, 1968.
- [36] M Baranger. Simplified quantum mechanical theory of pressure broadening. *Physical Review*, 111(2):481–493, 1958.
- [37] M Baranger. Problem of overlapping lines in the theory of pressure broadening. *Physical Review*, 111(2):494–504, 1958.
- [38] M Baranger. General impact theory of pressure broadening. *Physical Review*, 112(3):855–865, 1958.
- [39] HA Kramers. On the theory of x-ray absorption and of the continuous x-ray spectrum. *Philosophical Magazine*, 46:836–871, 1923.
- [40] AS Eddington. *The Internal Constitution of the Stars*. Cambridge, 1926.
- [41] HN Russell. On the composition of the sun’s atmosphere. *The Astrophysical Journal*, 70:11–82, 1929.
- [42] JA Gaunt. Continuous absorption. *Philosophical Transactions of the Royal Society of London. Series A, Containing Papers of a Mathematical or Physical Character*, 229:263–204, 1930.
- [43] JA Gaunt. Continuous absorption. *Proceedings of the Royal Society of London. Series A, Containing Papers of a Mathematical and Physical Character*, 126(803):654–660, 1930.
- [44] B Strömgen. The opacity of stellar matter and the hydrogen content of the stars. *Zeitschrift für Astrophysik*, 4:118–152, 1932.
- [45] PM Morse. The opacity of gas mixtures in stellar interiors. *The Astrophysical Journal*, 92:27–49, 1940.
- [46] R Epstein and L Motz. The solar internal opacity and constitution. I. *The Astrophysical Journal*, 120:156–158, 1954.
- [47] H Zirin. Radiative opacity of stellar matter. *The Astrophysical Journal*, 119:371–385, 1954.
-

- 
- [48] G Keller and RE Meyerott. A table of the radiative opacities of a number of gas mixtures. *The Astrophysical Journal*, 122:32–42, 1955.
  - [49] HF Mayer. Los Alamos Report LA-167, 1948.
  - [50] LH Aller. Proton-proton reactions in red dwarf stars. *The Astrophysical Journal*, 111:173, 1950.
  - [51] R Epstein. A two-energy source solar model. *The Astrophysical Journal*, 114:438, 1951.
  - [52] AN Cox and JN Stewart. Effects of bound-bound absorption on stellar opacities. *The Astrophysical Journal*, 67:113, 1962.
  - [53] A Arking and J Herring. Contribution of absorption lines to the opacity of matter in stellar interiors. *The Astrophysical Journal*, 67:113, 1962.
  - [54] A Arking and J Herring. The contribution of absorption lines to the opacity of matter in stellar interiors. *Publications of the Astronomical Society of the Pacific*, 75(444):226–235, 1963.
  - [55] AN Cox, JC Stewart, and DD Eilers. Effects of bound-bound absorption of stellar opacities. *The Astrophysical Journal Supplement*, 11:1–21, 1964.
  - [56] G Wallerstein, GH Herbig, and PS Conti. Observations of the lithium content of main-sequence stars in the hyades. *The Astrophysical Journal*, 141:610–617, 1965.
  - [57] RF Christy. The theory of cepheid variability. *Quarterly Journal of the Royal Astronomical Society*, 9:13, 1968.
  - [58] AW Rodgers. The masses of pulsating stars. *Monthly Notices of the Royal Astronomical Society*, 151:133–140, 1970.
  - [59] BC Cogan. Pulsation constants for models of cepheids. *The Astrophysical Journal*, 162:139, 1970.
  - [60] NH Magee, AL Merts, and WF Huebner. Improved opacity calculations. *The Astrophysical Journal*, 196:617–620, 1975.
  - [61] NR Simon. A plea for reexamining heavy element opacities in stars. *The Astrophysical Journal*, 260:L87–L90, 1982.
  - [62] GK Andreasen. Stellar consequences of enhanced metal opacity. I - an attractive solution of the Cepheid period ration discrepancies. *Astronomy and Astrophysics*, 201(1):72–79, 1988.
  - [63] CA Iglesias, FJ Rogers, and BG Wilson. Reexamination of the metal contribution to astrophysical opacity. *The Astrophysical Journal*, 322:L45–L48, 1987.
  - [64] CA Iglesias, FJ Rogers, and BG Wilson. Opacities for classical cepheid models. *The Astrophysical Journal*, 360:221–226, 1990.
  - [65] A Goldberg, BF Rozsnyai, and P Thompson. Intermediate-coupling calculation of atomic spectra from hot plasma. *Physical Review A*, 34(1):421–427, 1986.
  - [66] FJ Rogers and CA Iglesias. Radiative atomic Rosseland mean opacity tables. *The Astrophysical Journal Supplements*, 79:507–568, 1992.
  - [67] CA Iglesias and FJ Rogers. Updated OPAL opacities. *The Astrophysical Journal*, 464(2):943–953, 1996.
  - [68] JR Abdallah and REH Clark. X-ray transmission calculations for an aluminium plasma. *Journal of Applied Physics*, 69:23–26, 1991.
  - [69] MJ Seaton, Y Yan, D Mihalas, and AK Pradhan. Opacities for stellar envelopes. *Monthly Notices of the Royal Astronomical Society*, 266:805–828, 1994.
-

- 
- [70] DS Whittaker and GJ Tallents. Iron opacity predictions under solar conditions. *Monthly Notices of the Royal Astronomical Society*, 400:1808–1813, 2009.
  - [71] MJ Seaton and NR Badnell. A comparison of Rosseland-mean opacities from OP and OPAL. *Monthly Notices of the Royal Astronomical Society*, 354:457–465, 2004.
  - [72] JN Bahcall, S Basu, M Pinsonneault, and AM Serenelli. Helioseismological implications of recent solar abundance determinations. *The Astrophysical Journal*, 618:1049–1056, 2005.
  - [73] M Asplund. NEW LIGHT ON STELLAR ABUNDANCE ANALYSES: Departures from LTE and homogeneity. *Annual Reviews of Astronomy and Astrophysics*, 43:481–530, 2005.
  - [74] S Basu and HM Antia. Helioseismology and solar abundances. *Physics Reports*, 457:217–283, 2008.
  - [75] J Christensen-Dalsgaard, MP Di Mauro, G Houdek, and F Pijpers. On the opacity change required to compensate for the revised solar composition. *Astronomy and Astrophysics*, 494:457–465, 2009.
  - [76] AF Nikiforov, VG Novikov, and VB Uvarov. *Quantum-Statistical Models of Hot Dense Matter*. Birkhauser, 2000.
  - [77] BG Wilson, DA Liberman, and PT Springer. A deficiency of local density functionals for the calculation of self-consistent field atomic data in plasmas. *Journal of Quantitative Spectroscopy and Radiative Transfer*, 54(5):857–878, 1995.
  - [78] BF Rozsnyai. Relativistic Hartree-Fock-Slater calculations for arbitrary temperature and matter density. *Physical Review A*, 5(3):1137–1149, 1972.
  - [79] BF Rozsnyai. Bracketing the astrophysical opacities for the King IVa mixture. *The Astrophysical Journal*, 341:414–420, 1989.
  - [80] J Bauche, C Bauche-Arnoult, and M Klapisch. Unresolved transition arrays. *Physica Scripta*, 37:659–663, 1988.
  - [81] SA Moszkowski. On the energy distribution of terms and line arrays in atomic spectra. *Progress of Theoretical Physics*, 28(1):1–23, 1962.
  - [82] JC Pain, F Gilleron, J Bauche, and C Bauche-Arnoult. Effect of third- and fourth-order moments on the modelling of unresolved transition arrays. *High Energy Density Physics*, 5:294–301, 2009.
  - [83] P Duffy, M Klapisch, J Bauche, and C Bauche-Arnoult. Monte Carlo simulation of complex spectra for opacity calculations. *Physical Review A*, 44(9):5715–5724, 1991.
  - [84] J Bauche, C Bauche-Arnoult, J-F Wyart, P Duffy, and M Klapisch. Simulation of atomic transition arrays for opacity calculations. *Physical Review A*, 44(9):5707–5714, 1991.
  - [85] F Gilleron, J Bauche, and C Bauche-Arnoult. A statistical approach for simulating detailed-line spectra. *Journal of Physics B: Atomic and Molecular Physics*, 40:3057–3074, 2007.
  - [86] TH Maiman. Stimulated optical radiation in ruby. *Nature*, 187:493–494, 1960.
  - [87] A Hauer, RD Cowan, B Yaakobi, O Barnouin, and R Epstein. Absorption-spectroscopy diagnosis of pusher conditions in laser-driven implosions. *Physical Review A*, 34(1):411–420, 1986.
  - [88] C Chenais-Popovics, C Fievet, JP Geindre, JC Gauthier, E Luc-Koenig, J-F Wyart, H Pepin, and M Chaker.  $k_\alpha$  absorption spectroscopy: Diagnosis of the radiative preheating of laser-irradiated layered target. *Physical Review A*, 40(6):3194–3208, 1989.
  - [89] SJ Davidson, JM Foster, CC Smith, KA Warburton, and SJ Rose. Investigation of the opacity of hot, dense aluminium in the region of its k edge. *Applied Physics Letters*, 52:847–850, 1988.
-

- 
- [90] LB Da Silva, BJ MacGowan, DR Kania, BA Hammel, CA Back, E Hsieh, R Doyas, CA Iglesias, FJ Rogers, and RW Lee. Absorption measurements demonstrating the importance of  $\delta n = 0$  transitions in the opacity of iron. *Physical Review Letters*, 69(3):438–441, 1992.
  - [91] BKF Young, WH Goldstein, AL Osterheld, RE Stewart, G Charatis, and Gar E Busch. Spectroscopic analysis of a recombining laser-produced aluminium plasma. *Journal of Physics B: Atomic and Molecular Physics*, 22:L533–L538, 1989.
  - [92] TS Perry, PT Springer, DF Fields, DR Bach, FJD Serduke, CA Iglesias, FJ Rogers, JK Nash, MH Chen, BG Wilson, WH Goldstein, BF Rozsnyai, RA Ward, JD Kilkenny, R Doyas, LB Da Silva, CA Back, and R Cauble. Absorption experiments on x-ray-heated mid-Z constrained samples. *Physical Review E*, 54(5):5617–5631, 1996.
  - [93] WL Kruer. *The physics of laser plasma interactions*. Westview, 2003.
  - [94] R Kodama, K Okada, N Ikeda, M Mineo, KA Tanaka, T Mochizuki, and C Yamanaka. Soft X-ray emission from  $\omega_0$ ,  $2\omega_0$  and  $4\omega_0$  laser-produced plasma. *Journal of Applied Physics*, 59(9):3050–3052, 1986.
  - [95] AK Rossall, LMR Gartside, S Chaurasia, S Tripathi, DS Munda, NK Gupta, LJ Dhareshwar, JA Gaffney, SJ Rose, and GJ Tallents. X-ray back-lighter characterisation for iron opacity measurements using laser-produced aluminium K-alpha emission. *Journal of Physics B: Atomic and Molecular Physics*, 43:155403, 2010.
  - [96] DJ Hoarty, JWO Harris, P Graham, SJ Davidson, SF James, BJB Crowley, EL Clark, CC Smith, and L Upcraft. Measurements of niobium absorption spectra in plasmas with nearly full m-shell configurations. *High Energy Density Physics*, 3:325–334, 2007.
  - [97] PT Springer, DF Fields, BG Wilson, JK Nash, WH Goldstein, CA Iglesias, FJ Rogers, JK Swenson, MH Chen, A Bar-Shalom, and RE Stewart. Spectroscopic absorption measurements of an iron plasma. *Physical Review Letters*, 69(26):3735–3738, 1992.
  - [98] JM Foster, DJ Hoarty, CC Smith, PA Rosen, SJ Davidson, SJ Rose, TS Perry, and FJD Serduke. L-shell absorption spectrum of an open-m-shell germanium plasma: Comparison of experimental data with a detailed configuration-accounting calculation. *Physical Review Letters*, 67(23):3255–3258, 1991.
  - [99] F Thais, S Bastiani, T Blenski, C Chenais-Popovics, K Eidman, W Fölsner, J-C Gauthier, F Gilleron, and M Poirier. Absorption of local thermodynamic equilibrium aluminium at different densities. *Journal of Quantitative Spectroscopy and Radiative Transfer*, 81:473–485, 2003.
  - [100] C Chenais-Popovics, M Fajardo, F Gilleron, U Teubner, J-C Gauthier, C Bauche-Arnoult, A Bachelier, J Bauche, T Blenski, F Thais, F Perrot, A Benuzzi, S Turck-Chièze, J-P Chièze, F Dorchies, U Andiel, W Foelsner, and K Eidmann. L-band x-ray absorption of radiatively heated nickel. *Physical Review E*, 65(1):016413, 2001.
  - [101] C Chenais-Popovics, H Merdji, T Missalla, F Gilleron, J-C Gauthier, T Blenski, F Perrot, M Klapisch, C Bauche-Arnoult, J Bauche, A Bachelier, and K Eidman. Opacity studies of iron in the 15-30 eV temperature range. *The Astrophysical Journal Supplementary Series*, 127:275–281, 2000.
  - [102] H Merdji, T Miballa, T Blenski, F Perrot, JC Gauthier, K Eidmann, and C Chenais-Popovics. Absorption spectroscopy of radiatively heated samarium plasma. *Physical Review E*, 57(1):1042–1046, 1998.
  - [103] G Winhart, K Eidmann, CA Iglesias, A Bar-Shalom, E Minguez, A Rickert, and SJ Rose. XUV opacity measurements and comparison with models. *Journal of Quantitative Spectroscopy and Radiative Transfer*, 54(1):437–446, 1995.
-

- 
- [104] MH Edwards, PM Whittaker, N Booth, GJ Pert, Tallents GJ, B Rus, T Mocek, M Koslova, C McKenna, A Delsierieys, CLS Lewis, M Notley, and D Neely. Opacity measurements of a hot iron plasma using an X-ray laser. *Physical Review Letters*, 97, 2006.
  - [105] GJ Tallents, N Booth, MH Edwards, LMR Gartside, DS Whittaker, Z Zhai, B Rus, T Mocek, M Kozlová, J Polan, and P Homer. Measurements of opacity and temperature of warm dense matter heated by soft X-ray laser irradiation. *High Energy Density Physics*, 5:110–113, 2009.
  - [106] DJ Hoarty, CD Bentley, BJB Crowley, SJ Davidson, SG Gales, P Graham, JWO Harris, CA Iglesias, SF James, and CC Smith. The effect of line-broadening on the overall width of transition arrays in dense plasmas. *Journal of Quantitative Spectroscopy and Radiative Transfer*, 99:283–294, 2006.
  - [107] JE Bailey, GA Chandler, D Cohen, ME Cuneo, ME Foord, RF Heeter, D Jobe, PW Lake, JJ MacFarlane, TJ Nash, DS Nielson, R Smelser, and J Torres. Radiation science using Z-pinch X-rays. *Physics of Plasmas*, 9(5):2186 – 2194, 2002.
  - [108] JE Bailey, GA Rochau, CA Iglesias, Jr Abdalla, JJ MacFarlane, I Golovkin, P Wang, RC Mancini, PW Lake, PW Moore, M Bump, O Garcia, and S Mazevet. Iron-plasma transmission measurements at temperatures above 150 eV. *Physical Review Letters*, 99, 2007.
  - [109] A Goldberg and BF Rozsnyai. Effects of dielectronic satellite broadening on the emission spectra from hot plasmas. Lawrence Livermore Report UCRL-95472, 1986.
  - [110] G Gregori, SH Glenzer, FJ Rogers, SM Pollaine, OL Landen, C Blancard, G Faussurier, P Renaudin, S Kuhlbridt, and R Redmer. Electronic structure measurements of dense plasmas. *Physics of Plasmas*, 11(5):2754–2762, 2004.
  - [111] W Press, S Teukolsky, W Vetterling, and B Flannery. *Numerical Recipes in Fortran: The Art of Scientific Programming*. Cambridge University Press, 1996.
  - [112] MR Zirnbauer and DM Brink. Distribution of angular momenta in shell-model configurations. *Zeitschrift für Physik A*, 301:237–242, 1981.
  - [113] J Bauche and C Bauche-Arnoult. Level and line statistics in atomic spectra. *Journal of Physics B: Atomic and Molecular Physics*, 20:1659–1677, 1987.
  - [114] F Gilleron and JC Pain. Efficient methods for calculating the number of states, levels and lines in atomic configurations. *High Energy Density Physics*, 5:320–327, 2009.
  - [115] HR Griem. *Spectral Line Broadening by Plasmas*. Academic Press, 1974.
  - [116] HR Griem. Semiempirical formulas for the electron-impact width and shifts of isolated ion lines in plasmas. *Physical Review*, 165(1):258–266, 1968.
  - [117] MS Dimitrijevic and N Konjevic. Stark widths of doubly- and triply-ionised atom lines. *Journal of Quantitative Spectroscopy and Radiative Transfer*, 24(6):451–459, 1980.
  - [118] MS Dimitrijevic and N Konjevic. Simple estimates for stark broadening of ion lines in stellar plasmas. *Astronomy and Astrophysics*, 172:345, 1987.
  - [119] A Abramowitz and S Stegun. *Handbook of Mathematical Functions*. US Department of Commerce, 1970.
  - [120] E. E. Whiting. An empirical approximation to the Voigt profile. *Journal of Quantitative Spectroscopy and Radiative Transfer*, 8(6):1379 – 1384, 1968.
  - [121] J. Humlíček. Optimized computation of the Voigt and complex probability functions. *Journal of Quantitative Spectroscopy and Radiative Transfer*, 27(4):437 – 444, 1982.
-

- 
- [122] F. Schreier. The Voigt and complex error function: A comparison of computational methods. *Journal of Quantitative Spectroscopy and Radiative Transfer*, 48(5-6):743 – 762, 1992. Special Issue Conference on Molecular Spectroscopic Databases.
- [123] D Salzmänn. *Atomic Physics in Hot Plasmas*, volume 97 of *International Series of Monographs on Physics*. Oxford University Press, 1998.
- [124] SB Hansen, J Bauche, and C Bauche-Arnoult. Superconfiguration widths and their effects on atomic models. *High Energy Density Physics*, 7:27–37, 2011.
- [125] C Bauche-Arnoult, J Bauche, and M Klapisch. Variance of the distributions of energy levels and of the transition arrays in atomic spectra. *Physical Review A*, 20(6):2424–2439, 1979.
- [126] C Bauche-Arnoult, J Bauche, and M Klapisch. Variance of the distributions of energy levels and of the transition arrays in atomic spectra. II. configurations with more than two open subshells. *Physical Review A*, 25(5):2641–2646, 1982.
- [127] CE Porter. *Statistical Theories of Spectra: Fluctuations*. Academic Press, 1965.
- [128] K Nazir, SJ Rose, A Djaoui, G Tallents, MG Holden, PA Norreys, P Fews, J Zhang, and F Failles. X-ray spectroscopic studies of hot, dense iron plasma formed by subpicosecond high intensity KrF laser irradiation. *Applied Physics Letters*, 69(24):3686–3688, 1996.
- [129] Y Ralchenko, AE Kramida, J Reader, and The NIST ADS Team. NIST atomic spectra database (version 4). Online, 2008. Available: <http://physics.nist.gov/asd3>.
- [130] P Jönsson, X He, C Froese-Fischer, and IP Grant. The grasp2K relativistic atomic structure package. *Computer Physics Communications*, 177:597–622, 2007.
- [131] J Bauche, C Bauche-Arnoult, E Luc-Koenig, J-F Wyart, and M Klapisch. Emissive zones of complex atomic configurations in highly ionized atoms. *Physical Review A*, 28(2):829–835, 1983.